UNIVERSITÀ DEGLI STUDI DI CAMERINO

School of Advanced Studies

DOCTORAL COURSE IN

PHYSICS

XXXV cycle

Novel Phenomena With Berezinskii-Kosterlitz-Thouless Transition, Topological Fluctuations, and Phase Slips in Superconducting NbN Nanofilms

PhD Student

Meenakshi Sharma

Supervisor

Professor Andrea Perali

Co-supervisor

Professor Nicola Pinto

To the person who dared to dream...

Abstract

This thesis presents a systematic investigation of phase fluctuation effects in superconducting niobium nitride (NbN) nanofilms, exploring the rich physics that emerges during dimensional crossover from three-dimensional to two-dimensional and quasi-one-dimensional behavior. The experimental foundation of this study is based on the careful optimization of DC magnetron sputtering parameters, enabling the fabrication of high-quality NbN films with thicknesses ranging from 5 nm to 100 nm on various substrates including MgO, Al_2O_3 (r-cut and c-cut), and SiO_2. To ensure precise electrical measurements, the fabrication process was refined through the development of Hall bar geometries using optical lithography and reactive ion etching techniques, with particular attention to preserving film quality during processing.

Our systematic electrical transport measurements reveal two distinct manifestations of phase fluctuations in these films. In the two-dimensional regime, we observe the emergence of the Berezinskii-Kosterlitz-Thouless (BKT) transition in ultra-thin NbN films (d < 15 nm), characterized by a universal jump in the superfluid phase stiffness at T_{BKT}. The application of perpendicular magnetic fields (3-150 Gauss) leads to an interesting behavior: a field-induced crossover from Halperin-Nelson fluctuations to a BCS-like state with Aslamazov-Larkin fluctuations. This transition exhibits distinct regimes, with the BKT signature preserved up to 5 Gauss, gradually smearing between 5-50 Gauss, and completely suppressed by 100 Gauss, where conventional current-voltage behavior emerges. The crossover mechanism is attributed to field-induced free vortices screening the loga-

rithmic vortex-antivortex interactions.

As the dimensionality is further reduced, we observe the emergence of phase-slip phenomena in the quasi-1D regime. The intrinsic disorder within the granular NbN matrix leads to the formation of channels, whose dimensions critically influence the nature of phase fluctuations. Through careful analysis of temperature-dependent resistivity and current-voltage characteristics, we establish a quantitative correlation between the type of phase slips (quantum vs. thermal) and the size of these pathways relative to the superconducting coherence length. Most notably, we discover the unprecedented coexistence of BKT transition and thermally activated phase slips within the same system, highlighting the subtle interplay between nano-conducting path dimensions and coherence length.

These investigations employ comprehensive characterization techniques, including resistivity measurements, current-voltage characteristics, and magnetic field-dependent studies, all conducted using a specially designed pulsed measurement technique to minimize heating effects. Observing these coexisting phenomena, together with their tunability through temperature, thickness, and magnetic field, not only advances our understanding of phase fluctuation mechanisms in low-dimensional superconductors but also opens new possibilities for controlling quantum phase transitions in advanced superconducting devices.

Contents

List of Figures

List of Tables

Declaration

I hereby declare that this thesis is entirely my own work and has not been previously submitted, in whole or in part, for any academic degree or other qualification at this or any other university.

All sources used in this thesis have been acknowledged and are properly cited in the References section. Where research has been conducted in collaboration with others, I have clearly indicated my individual contributions and given due credit to my collaborators.

The work presented in this thesis has been published in part in the following papers, which form the foundation of the research described herein:

[1] **Meenakshi Sharma**, Manju Singh, Rajib K. Rakshit, Surinder P. Singh, Matteo Fretto, Natascia De Leo, Andrea Perali, Nicola Pinto. Complex Phase-Fluctuation Effects Correlated with Granularity in Superconducting NbN Nanofilms. Nanomaterials. 2022 Nov 22;12(23):4109.

[2] **Meenakshi Sharma**, Sergio Caprara, Andrea Perali, Surinder P. Singh, Sandeep Singh, Nicola Pinto. Berezinskii-Kosterlitz-Thouless to BCS-like superconducting transition crossover driven by weak magnetic fields in ultra-thin NbN films. arXiv preprint: 2403.11685 (2024). (Under review)

Acknowledgements

As I reflect on my journey to completing this PhD thesis, I am filled with gratitude for the many individuals who have supported, guided, and inspired me along the way.

First and foremost, I would like to express my deepest appreciation to my co-advisors, Prof. **Nicola Pinto** and Prof. **Andrea Perali**. Prof. Pinto, your patience in teaching me from the ground up has been invaluable. You have not only imparted scientific knowledge but also life lessons, treating me like family in this unfamiliar place. Your guidance in developing research skills, scientific writing, and conceptual thinking has been transformative. Prof. Perali, your unwavering encouragement of my ideas gave me the confidence to grow as a researcher. Thank you for facilitating collaborations, providing opportunities to present at conferences, and supporting me through challenging times. Your trust and optimism have been a constant source of strength.

I am especially grateful to both of you for your care during the difficult period of the COVID-19 pandemic. When I missed my family, you reassured me that I had a family here in Camerino. Your support extended far beyond academic guidance, and for that, I am truly thankful.

A special thank you to **Daniela**, Prof. Perali's wife, for your thoughtfulness in arranging vegetarian meals at conferences and for making me feel so welcome. Your kindness has meant more than words can express.

I would like to express my sincere gratitude to **Prof. S. Caprara** from the University of Roma for his invaluable contributions to this thesis. His insightful suggestions and guidance were instrumental in shaping the direction of my research. The numerous fruitful discussions we shared during conferences proved essential to the development of this work. I am immensely grateful for his support and mentorship throughout this process.

I owe a great debt of gratitude to Dr. **S.P. Singh**, who set me on this research path. Your ongoing support and crucial contributions to this project, particularly in providing important samples, have been instrumental in bringing this work to fruition. I am honored to continue working with you and am grateful for your familial care.

My sincere thanks to Dr. **Manju** and Dr. **Rajib** for supplying high-quality NbN films that were essential to my experiments and for offering valuable guidance on future research directions.

I am deeply appreciative of Dr. **N. De Leo** and Dr. **M. Fretto** from INRIM for the exceptional opportunity to work in a national laboratory. Your assistance in sample fabrication was crucial to the successful completion of my PhD work.

To my dear friends in Camerino - **Pradnya**, **Aniqa**, **Ifra**, **Bita**, and **Natasha** - thank you for your support and for the fun moments we shared. Your friendship made this small town feel like home and helped me persevere through the challenges of PhD life. Despite our diverse backgrounds, you became my family away from home, sharing laughter, tears, and everything in between.

Benedetta, my lab-mate and friend, thank you for brightening the lab with your presence, your delicious chocolate cakes, and your help with experiments. Our friendship, though formed in the final year of my PhD, has been a wonderful addition to this journey.

To **Satish**, thank you for being an excellent friend, for your help with research ideas, and for always lending an ear. Our long discussions have been both intellectually stimulating and personally enriching.

I would like to extend my gratitude to the staff members, especially **Gianna** and **Paolo**, for their daily warm greetings and assistance with day-to-day matters. Your smiles and support have made a significant difference in my time here.

A special thank you to my best friends **Sanu**, **Rashi**, and **Komal**. Although we pursued our PhDs in different countries and at different times, our shared experiences have kept us connected. Your constant support, our video calls during the isolating times of the pandemic, and our growing friendship over these five years have been invaluable. We've matured together, from uncertain students to confident individuals ready to face life's challenges.

To my family - **Mummy**, **Papa**, **Ritu**, and **Rahul** - your unwavering support has been my foundation. Thank you for your patience, for believing in me, and for enduring my occasional frustrations. Ritu, your presence motivates me to be the best version of myself, and Rahul, your encouragement and celebration of my accomplishments mean the world to me.

To **Krishii** (my husband), whose unwavering support has been crucial throughout my PhD journey. His constant encouragement, patience, and understanding have been instrumental in bringing this thesis to fruition. His belief in my abilities has been a source of strength, and his sacrifices have not gone unnoticed. I am profoundly grateful for his presence in my life and his invaluable contribution to this achievement. Without his support, this milestone would not have been possible.

Lastly, I would like to acknowledge the University of Camerino for providing the environment and resources necessary for my research. This journey has been challenging but immensely rewarding, and I am grateful for the opportunity to contribute to the field of Physics through this work.

To everyone mentioned here and to those whom I may have inadvertently omitted, thank you for being part of this incredible journey. Your contributions, big and small, have made this thesis possible and have shaped me both as a researcher and as a person.

Chapter 1

Introduction

In 1911, the Dutch physicist Heike Kamerlingh Onnes achieved a landmark discovery by observing superconductivity in pure mercury, which transitions to this state below 4.2 K [1]. The pursuit of unraveling this fascinating phenomenon encouraged the development of various phenomenological models. The Ginzburg-Landau theory [2], a milestone in the field of superconductivity, represented a remarkable step forward in our understanding of the phenomenon providing a macroscopic framework that explained its nature as a second-order phase transition. The detailed explanation of this discovery was later given by the first microscopic theory of superconductivity formulated by Bardeen, Cooper, and Schrieffer (BCS theory) in the year 1957 [3], suggesting that the electrons form a bound pair at low temperatures due to attractive interaction mediated by phonons. These pairs known as ”Cooper pairs” then condense into a collective quantum ground state where their motion is perfectly correlated, allowing the dissipation less electric current.
However, conventional BCS theory predicted a maximum critical temperature (T_C) of approximately 40 K, known as the McMillan limit. This constraint posed a significant challenge for developing high-temperature superconductors, prompting the search for novel mechanisms and materials to overcome this limitation.
A breakthrough came in 1986 when Bednorz and Müller discovered high-temperature

superconductivity in cuprates [4], earning them the 1987 Nobel Prize in Physics. This discovery revolutionized the field by demonstrating superconductivity at temperatures far beyond the McMillan limit. The phenomenon in cuprates could not be satisfactorily explained by BCS theory, particularly regarding the effect of thermal vibrations on weak electron-phonon coupling. This led to a new class of materials known as unconventional superconductors, spurring intense research into alternative conduction mechanisms.
As our understanding of superconductivity evolved, attention began to shift towards exploring this phenomenon in lower-dimensional systems, particularly in two dimensions. This transition to studying 2D superconductivity opened up new avenues for research and brought forth unique challenges and discoveries.

1.1 Historical Overview of 2D Superconductivity

Early Explorations and Graphene's Impact: The exploration of 2D superconductivity initially involved amorphous films of materials like $NbSe_2$ [5], Tin [6] and Gallium[7]. Despite their pioneering nature, these early studies were often hampered by sample quality issues, where intrinsic disorder obscured many of the intricate phenomena characteristic of 2D superconductors. The discovery of graphene in 2004 revitalized the field, acting as a catalyst for the study of 2D materials. Graphene's unique electronic and mechanical properties paved the way for exploring superconductivity in other ultrathin materials [8–13]. This led to the advent of atomically thin crystals, particularly transition metal dichalcogenides (TMDs), with NbSe2 gaining significant attention in this new 2D landscape [11, 12, 14–17].

Initial studies in 2009 revealed a clear trend: as the material thickness was reduced layer by layer, the superconducting transition temperature (T_C) decreased, aligning with theoretical predictions about enhanced fluctuations in lower dimensions [5]. However, as

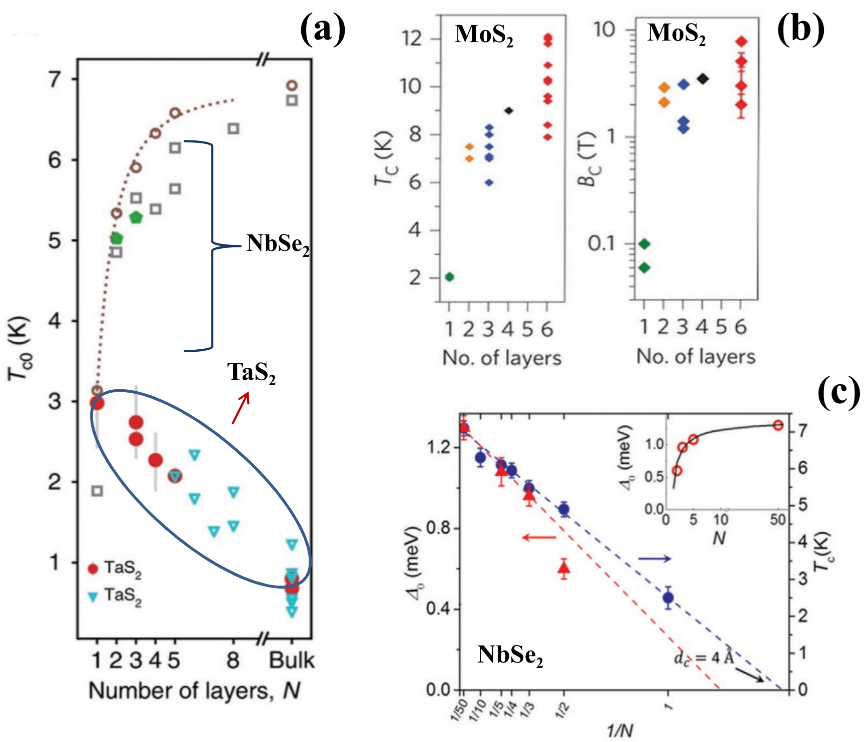

Figure 1.1: The figures illustrate how superconducting properties change with thickness in various Transition Metal Dichalcogenides: a) The graph depicts the relationship between thickness and transition temperature (T_C) for NbSe$_2$ and TaS$_2$, as detailed in the study carried out by Barrera et. al. [18]. For NbSe$_2$, a monotonic trend is observed as thickness changes. In contrast, TaS$_2$ shows an opposite trend, with Tc increasing as thickness decreases compared to the bulk system. b) Two panels are presented for MoS$_2$: the left panel demonstrates the effect of thickness on T_C, while the right panel shows how the critical magnetic field (B_C) is affected by thickness [19]. C) For NbSe$_2$, variations in both the superconducting gap and T_C are shown. The x-axis represents the inverse of thickness, allowing visualization of how these properties change as the material thickness decreases [20].

fabrication and assembling techniques improved—utilizing inert atmospheres and hexagonal boron nitride (hBN) encapsulation—researchers made groundbreaking discoveries in 2015 [15]. They found that superconductivity persisted even in a single atomic layer of $NbSe_2$ (Fig.1.1(a) and (c)), albeit with a heavily suppressed T_C of only 2 K at most. The exploration expanded to other TMDs like MoS_2[19] (Fig.1.1(b)) and WTe_2 [21, 22], each bringing its own surprises . MoS_2, for instance, showcased a remarkable transition from a band insulator to a superconductor when its carrier concentration was tuned by electrostatic gating, offering unprecedented control over the superconducting state [19, 23–25]. As research progressed, a complex interplay between various factors in these 2D systems emerged. Thickness, carrier concentration, disorder, and substrate effects all played crucial roles in determining superconducting properties. While the conventional Bardeen-Cooper-Schrieffer (BCS) theory remained applicable in many cases, the 2D landscape introduced new complexities that would soon lead to exciting discoveries beyond the conventional paradigm.

High-Temperature Superconductors and Enhanced Interfacial Phenomena: The study of 2D superconductivity underwent a significant shift with the investigation of high-temperature superconductors in the 2D limit. Initially, attempts to create ultrathin layers of cuprate superconductors were discouraging, with superconductivity seeming to degrade rapidly as materials were thinned down [26–28]. However, persistence and improved techniques eventually yielded success. In 2018, researchers fabricated unprotected monolayer $Bi_2Sr_2CaCu_2O_{8+x}$ (Bi-2212) on a cold stage in an inert atmosphere [29], which remarkably retained bulk superconductivity with a T_C of 87 K (Fig.1.3(a), (b) and (c)). This discovery challenged previous notions about the fragility of high-T_C superconductivity in 2D and opened new avenues for studying these complex materials in their most fundamental form [30].

The field of 2D high-T_C superconductivity experienced a paradigm shift before the afore-

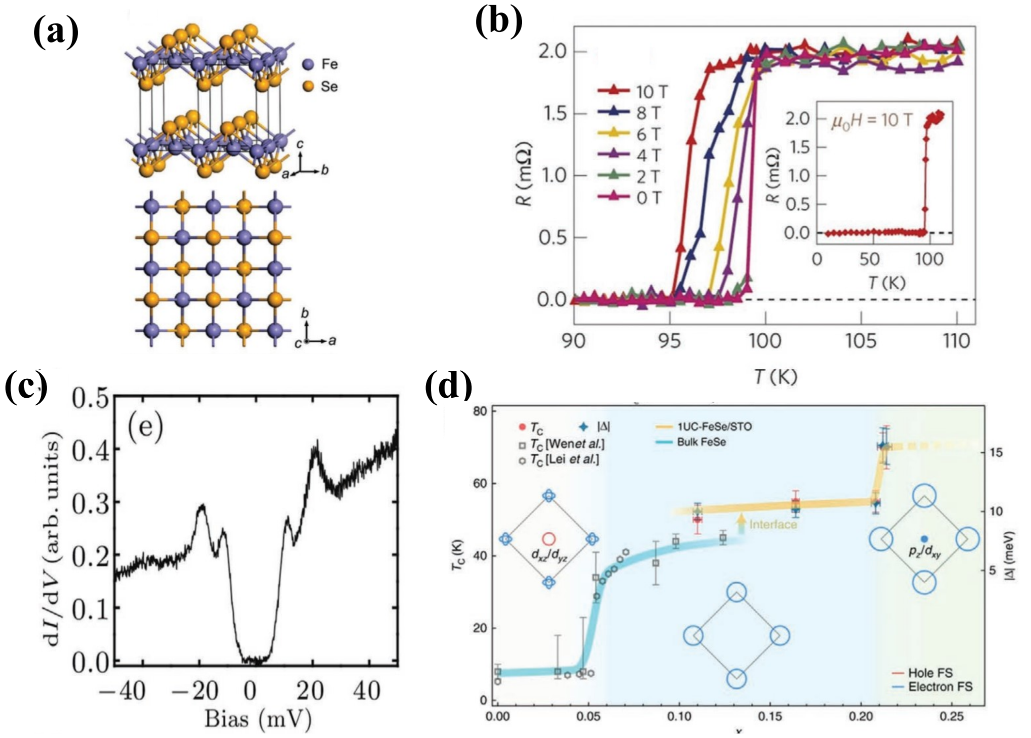

Figure 1.2: a) Illustration depicting the crystal structure of β-FeSe [31]. b) Graph showing how the resistance changes with temperature for a 1UC FeSe film [31]. The data was collected using a four-probe measurement technique. c) Scanning tunneling spectroscopy results for 1UC FeSe/STO [16], revealing the superconducting gap. Notable coherence peaks are observed at approximately ±20.1 mV and ±9 mV. d) Phase diagram of FeSe depicting the progression of superconductivity and associated changes in Fermi surface topology. The diagram shows how these properties evolve under different conditions [32].

mentioned discovery with the observation of enhanced superconductivity in iron-based systems. In 2012, researchers grew a single atomic layer of FeSe on a $SrTiO_3$ substrate (1UC FeSe/STO), observing superconductivity at temperatures ranging from 60 K to over 100 K—far exceeding the Tc of bulk FeSe (8 K) [16, 33] (Fig.1.2). This system became emblematic of enhanced superconductivity in 2D materials. The FeSe/STO interface's crucial role in boosting superconductivity was evident from the dramatic drop in T_C upon adding just one more FeSe layer [33, 34]. The observation of enhanced superconductivity at the FeSe/STO interface ignited a wave of research aimed at understanding the underlying mechanisms, including the potential roles of charge transfer, electron-phonon coupling, and strain. The relative simplicity of the FeSe/STO system compared to cuprates offered a unique opportunity to unravel the mysteries of high-T_C superconductivity, potentially paving the way for new insights into this complex phenomenon.

Moiré Superlattices: The quest to understand and control exotic quantum states in materials took an unexpected turn with the discovery of moiré superlattices [35–37]. This new chapter in condensed matter physics began in 2018 when researchers found that simply twisting two layers of graphene to a precise "magic angle" could yield remarkable properties. By creating a long-wavelength periodic modulation, these twisted structures unlocked a world of strong electron correlations typically associated with complex materials like high-temperature superconductors.

The initial breakthrough came from observing unconventional superconductivity and Mott-like insulating states in twisted bilayer graphene (TBG) (Fig.1.3 (d) and (e)) at a magic angle of about 1.1° [40]. This remarkable finding generated significant excitement within the scientific community, prompting a flurry of investigations into various moiré systems. As researchers delved deeper, they uncovered a rich landscape of electronic phases, from correlated insulators to superconducting domes, that could be tuned with unprecedented precision. As the quality of TBG samples improved, scientists unveiled an increasingly complex phase diagram. They observed additional superconducting domes, including near the charge neutrality point, and explored the intricate relationship between superconductivity and correlated insulator states. Surprisingly, recent experiments using enhanced screening techniques revealed that superconductivity could persist even when correlated insulator phases were suppressed. This unexpected finding has sparked new

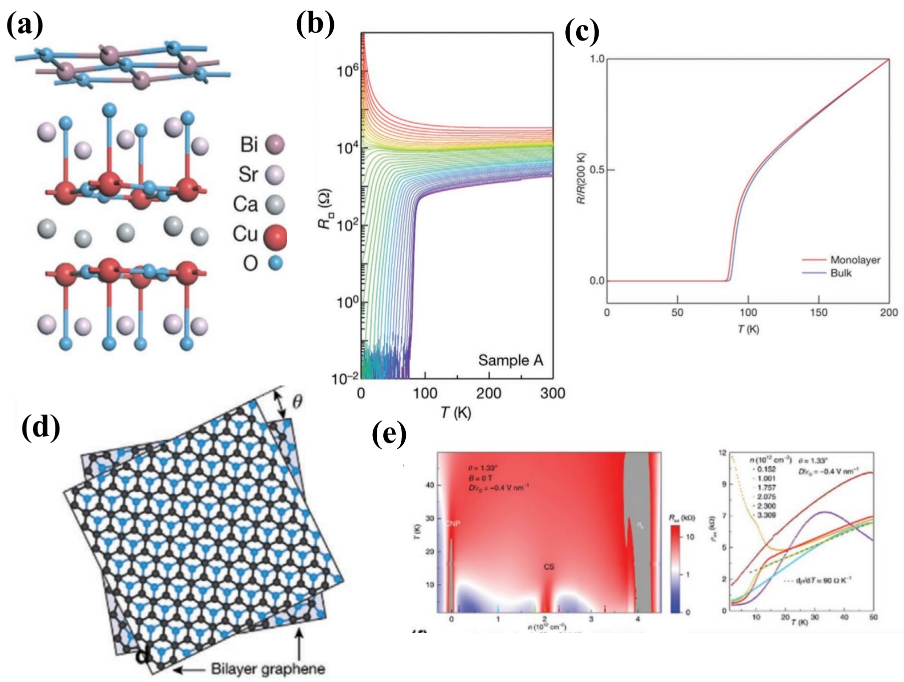

Figure 1.3: Analysis of two-dimensional Cu-based superconductors. a) Diagrammatic representation of the Bi-2212 crystalline arrangement [29]. b) Graph illustrating the temperature dependence of resistivity in a single-layer Bi-2212 sample [29]. c) Electronic characteristic analysis of monolayer Bi-2212, highlighting that the observed critical temperature (T_c) exhibits minimal variation from bulk measurements [29]. d) Structural representation of twisted double bilayer graphene (TDBG) with a specified twist angle θ [38]. e) Two-panel display: The left panel shows a color-coded plot of resistivity R_{xx} as a function of temperature T and carrier density n for a 1.33° twisted device. The right panel depicts the dependence of resistivity on temperature T and carrier density n [39].

debates about the nature of superconductivity in TBG and its underlying mechanisms.

The story quickly expanded beyond graphene [41]. Scientists began exploring twisted double-bilayer graphene, ABC-trilayer graphene on boron nitride, and even twisted transition metal dichalcogenides. Each system brought its surprises, such as spin-polarized states or strong electron-hole asymmetry. The ability to control these quantum phases through variables like twist angle, carrier density, and electric fields offered a new playground for studying fundamental physics.

However, as with any scientific frontier, challenges and mysteries abound. The extreme sensitivity to small variations in twist angle has made reproducibility a key issue. The role of disorder and twist angle inhomogeneity in these systems remains a crucial area of investigation. As researchers continue to unravel these puzzles, the hope is that insights from moiré superlattices might illuminate long-standing questions in strongly correlated electron physics and perhaps even pave the way for new quantum technologies.

The Final Frontier-Topological Superconductivity and Majorana Fermions: As our journey through the landscape of 2D superconductors nears its end, we arrive at perhaps the most exotic and promising frontier: topological superconductivity. This state of matter, characterized by a bulk superconducting gap and gapless edge states, has captured the imagination of physicists due to its potential for hosting Majorana fermions—particles that are their antiparticles [42].

Researchers have explored various avenues to achieve topological superconductivity in 2D systems. One method involves the proximity effect, where a conventional superconductor induces superconductivity in an adjacent topological material [43]. The $NbSe_2$ / Bi_2Se_3 heterostructure serves as a prime example of this approach [44]. The $NbSe_2$ / Bi_2Se_3 heterostructure emerged as a prototypical system in this category. By interfacing the 2D superconductor $NbSe_2$ with the topological insulator Bi_2Se_3, researchers created a platform where Majorana fermions could potentially emerge at the edges [44].

Another strategy involves introducing magnetic impurities into superconductors. This approach, while challenging to implement in practice, offers the potential to create designer topological states. Recent work has also demonstrated the possibility of inducing topological superconductivity through electrostatic gating, as seen in monolayer WTe_2 [45].

The pursuit of topological superconductivity is driven not just by fundamental curiosity but also by the tantalizing prospect of topological quantum computation. Majorana fermions, with their non-Abelian statistics, could serve as the building blocks for quantum bits (qubits) that are inherently protected against decoherence—a holy grail in the field of quantum information [42].

1.2 Emerging Challenges and Opportunities in 2D

As we conclude our journey through the world of 2D superconductors, we find ourselves at the frontier of condensed matter physics. From the early days of studying conventional BCS superconductivity in ultrathin films to the recent discoveries of high-Tc interfaces, moiré superlattices, and topological states, the field has been a wellspring of surprises and new physics[46, 47].

This historical overview sets the stage for our deeper exploration of the intricate phenomena observed in two-dimensional superconducting systems. As we move forward, we will delve into the specific challenges and opportunities presented by materials, focusing on the interplay between various energy scales and the emergence of fascinating quantum effects.

The success of the BCS theory in describing conventional superconductivity lies in its ability to use a single energy scale, the superconducting gap (Δ), to explain various superconducting properties. However, for a long time, another energy scale, the superfluid phase stiffness (J_S), has been overlooked. This is due to the fact that, in most conventional superconductors, the value of J_S is several orders of magnitude larger than Δ, making it seemingly irrelevant. However, under the condition when J_S becomes much smaller than Δ due to factors such as inhomogeneity, disorder, granularity, or low dimensionality, it gives rise to various intriguing phenomena. In such cases, J_S becomes a crucial energy scale that can effectively describe all the superconducting properties of the investigated system.

With significant progress in the development of nanostructures, there is a growing scientific interest in the field of materials science, particularly in the use of atomically thin layers for device fabrication. Subsequently, understanding the fundamental superconducting properties of these systems became crucial for their successful implementation. From the phenomenological point of view, the low-dimensional systems exhibit intriguing quantum phenomena explicitly when the thickness of the film becomes comparable to the coherence length (d$\approx\xi$) giving rise to the various fluctuation effects. Some of these effects include phase slips [48–52], quantum criticality [53], superconductor-insulator transitions [54], and quantum-phase transitions [55, 56].

The most fascinating phenomenon that has generated great interest in the condensed matter community for many years is the Berezinskii-Kosterlitz-Thouless transition, observed in two-dimensional superconducting systems. The significance of this transition lies in its ability to bypass the constraints of the Mermin-Wagner-Hohenberg theorem, which states that a spontaneous symmetry breaking cannot occur in dimensions two or lower[57]. Later, in the year 2016, Kosterlitz and Thouless won a prestigious Nobel prize for the theoretical discovery of topological phase transitions[58]. The core concept in BKT physics revolves around the shift in the temperature dependence of the correlation function, transitioning from a power-law dependence due to the proliferation of topological defects to an exponential dependence as the system approaches the T_{BKT}. This results in an unusual temperature-dependent resistivity near the transition temperature, with measurable effects confined to a narrow range of temperatures, rendering its experimental detection quite challenging.

To empirically detect this phenomenon, an array of studies has been conducted across various superconducting systems with ultra-thin geometries [47, 59–64], employing various techniques. The signature of this effect can be detected in the resistivity variation close to the superconducting transition temperature T_C producing a detectable feature in the other transport properties as also studied extensively by Venditti et al. [65], Mondal et al. [66], Weitzel et al. [67].

For several years, serious efforts have been made to improve the understanding of topological defects (vortex-antivortex), that are at the core of the well-established BKT theory[58, 59, 64, 66–69]. However challenges persist in interpreting the BKT effect, due to the intrinsic properties of the superconducting systems under investigation such as:

a) The Presence of quasi-particle excitations in a superconducting system results in the decrease of superfluid density. This decrease limits the temperature range to observe the BKT effect in the region $T_{BKT} < T < T_{MF}$. Consequently, the effects of mean field interactions dominate, making it challenging to precisely determine the value of T_{BKT}. b) Secondly, the charged super-currents result in significant screening effects where logarithmic interactions of the VAP pair get hindered, and results in the smearing of BKT effect[66].

c) The most important is the intrinsic inhomogeneity, which is usually present in SC ultra-thin films as NbN [70, 71], NbTiN, In/InO_X [59, 72, 73] giving rise to a broadening in the transition and results in the vanishing of BKT phenomenon.

To address fabrication challenges and deepen our understanding of the emerging phase fluctuation mechanisms resulting from the dimensional crossover, this thesis will provide a comprehensive analysis of the fluctuation effects. Initiating from the **Chapter 2** which is dedicated to detailing the fabrication process of a uniform two-dimensional superconducting system, while optimizing the relevant parameters. In this regard, considerable efforts have been devoted to fabricating high-quality, ultra-thin films of NbN, which is a well-known and researched material, belonging to the family of strongly coupled type-II superconductors and its thin films that possess high structural uniformity and a relatively high superconducting transition temperature T_C of 16 K [74, 75]. The fabrication has been carried out by exploiting the DC magnetron sputtering deposition technique. Several factors have contributed to the complexity of the process, including a careful selection of suitable substrates to reduce high lattice mismatch, precise control of deposited film thickness, accurate control of the $Ar : N_2$ ratio during deposition, and controlling the chemical defect densities. In addition to the challenges faced during film deposition, the subsequent steps involved in Hall bar fabrication have added further complexities. Each of these steps has been performed with a precise optimization and control of the parameters, adding to the overall challenges of the process.

Along with the fabrication technique, a systematic measurement of different electronic transport properties has been carried out in detail, emphasizing reducing the possible heating effects of the SC system during its characterization in order to observe a clear hallmark of a phase transition. These efforts in the fabrication have been aimed at developing a robust method and a reliable technique to ensure the precisely engineered 2D superconducting platform.

After the successful optimization and fabrication of a 2D SC system, **Chapter 3** of this thesis is devoted to the experimental exploration of Berezinskii-Kosterlitz-Thouless transition phenomena. To experimentally detect the BKT effect, we have carried out electrical transport characterization to identify the occurrence of a phase transition in close proximity to T_C. To characterize the 2D nature of these systems, we have utilized the Cooper pair fluctuation model and employed the Halperin-Nelson approach as a means of confirming the manifestation of the BKT effect [76]. Furthermore, the power law behavior observed in the current-voltage (I-V) characteristics ($V \propto I^{\alpha}$) is observed by a sharp jump in the α exponent [67, 77]. This jump in α served as a clear indication of the transition in the superfluid density, which is the hallmark of an observing BKT effect. It's worthwhile mentioning that all these experiments have been carried out in the absence of any applied magnetic field, that can otherwise induce magnetic vortices in the system or may broaden the superconducting transition partially or totally masking BKT effects.

Furthermore, the investigation at low magnetic fields ($H < H_{C1}$) on the superconducting properties of 2D systems has been largely lacking in literature both from theoretical and experimental perspectives. This gap in the knowledge leaves an incomplete understanding within the framework of BKT physics which motivated us to explore the influence of magnetic fields, primarily focusing on very low H field intensities, which are typically considered insignificant, in order to closely examine their impact on the system. The outcomes of these experiments have delivered clear evidence of a gradual vanishing effect in the BKT physics, which completely disappeared at remarkably low field intensities of around 100 Gauss [78]. The smearing of this phenomenon has been attributed to the generation of a large number of free vortices, even at extremely weak perpendicular magnetic fields. These vortices exhibit the ability to easily penetrate the two-dimensional material and closely interact with the VAP pairs present in the system, leading to a significant modification of the superconducting properties in low-dimensional systems and eventually smearing the BKT physics. The study has been detailed in the **Chapter 4** of this thesis investigating the electrical properties of NbN thin films ($<$ 15 nm) ranging from 0 to 150 Gauss.

On the other hand, the successful fabrication of 1 D systems such as superconducting nanowires has attracted significant attention for their applicability in fields ranging from superconducting nanowire detectors to kinetic inductance detectors [79], photon counters, qubits [80], and quantum communication, etc. Over the past few years, these systems have served as foundational elements for exploring advanced concepts such as high-temperature superconductivity, coherence, and macroscopic quantum tunneling.

In a typical 1D system, where the transverse dimension is significantly smaller than both the coherence length (ξ) and the magnetic penetration depth (λ), fluctuations manifest in a very different form. In these systems, the intermediate resistive states form due to the change in phase of the order parameter by 2π, resulting in a discontinuous voltage jump, forming a phase slip center. The analogous to phase slip centers are phase slip lines which take place in a two-dimensional system. Even though the time-dependent Ginzburg Landau (TDGL) equations show that the driving force in both cases is completely different, they display similar hallmarks in the current-voltage characteristics. Gaining a comprehensive understanding of these resistive states is of utmost importance as it forms the foundation for advancing fundamental scientific knowledge and the development of innovative technological applications.

These phase slip lines (PSLs) are typically detected near the critical temperature, T_C, due to the thermal activation across an energy barrier, which induces a finite value of residual resistance below T_C. This phenomenon is described theoretically by Langer, Ambegaokar, McCumber, and Halperin, widely known as the LAMH theory[81]. As the temperature decreases, thermal fluctuations freeze, providing the way for quantum phenomena to emerge, particularly known as quantum phase slips (QPS). Extensions to the LAMH theory by Giordano [82] have provided a coherent explanation for these observations. However, the specific length scale at which these quantum effects become pronounced continues to be a subject of debate. On the other hand, researchers have explored 1D and 2D systems separately, but the regime of crossover from the BKT effect to a phase slip phenomenon remains an area of uncertainty.

To understand these long overdue questions, we have experimentally investigated the phase slip effects in the **Chapter 5** of this thesis by characterization of transport measurements, in our NbN ultra-thin films. The effect has been studied, specifically in relation to the change in the width of the superconducting channel, while maintaining a constant thickness of the ultra-thin film, which shows a crossover from TAPS to QPS, as the width reduces. Additionally, an interesting trend in the number of phase slip lines at different temperature values has been observed, which effectively marks three different regions that are characterized by the dominance of QPS or TAPS. Observing this phenomenon in a superconducting system has been a challenge due to the complicated fabrication process, which can result in the emergence of defects when the thickness is substantially reduced. Therefore, the fabricated SC films have been extensively studied and the experimental results are discussed in detail focusing on the crossover regions resulting from different fluctuation mechanisms.

The significant results obtained in this work, which contribute valuable insights to the existing literature, are summarized in **Chapter 6** of this thesis. Additionally, the thesis outlines future perspectives, emphasizing the importance of understanding quantum effects for advancing future technologies. This understanding could offer a novel platform for tuning these systems.

Chapter 2

Material and Methods

2.0.1 Film deposition

Niobium nitride (NbN) nanofilms were synthesized using DC magnetron sputtering, a technique renowned for producing highly uniform, homogeneous, and adherent ultra-thin films. The deposition process was meticulously optimized to obtain films with thicknesses spanning from 5 nm to 100 nm on four distinct substrates: magnesium oxide (MgO), R-plane and C-plane sapphire (Al_2O_3), and silicon dioxide (SiO_2).

DC Magnetron Sputtering

DC magnetron sputtering, a well-established thin film deposition technique, has been extensively employed for decades due to its remarkable ability to produce high-quality thin films. In this process, energetic ions bombard a target material, causing the ejection of atoms or molecules from its surface through momentum transfer. These sputtered particles then traverse the vacuum chamber and impinge upon the substrate surface, undergoing kinetic rearrangement and coalescence to form a homogeneous and strongly adherent film.

Figure 2.1: Reactive DC magnetron Sputtering system from EXCEL instruments at the facility of CSIR-National Physical Laboratory, New Delhi, India, used for the deposition of ultra-thin NbN films

Deposition Mechanism

Depending on the power supply, the sputtering process may be classified as DC or RF sputtering. DC sputtering phenomena fail if the cathode surface is insulating. This is typically the case of an insulating target or in the presence of oxygen in the deposition chamber which makes the surface insulating and results in extremely low discharge currents and low sputtering. For insulating surfaces, the charge localizes as the ions strike the surface and with time a sheath of positive charge builds up on the target surface, preventing it from further sputtering. This sheath of positive charges can be prevented by the bombarding of positive ions and electrons simultaneously to the insulator which is generally achieved by applying a RF potential to the target. The alternating field of RF potential provides sufficient energy to the electrons to cause ionizing collisions and results in a self-sustained discharge. More electrons will reach the insulating target surface due to higher electron mobility during the positive half cycle. As the target becomes self-biased negatively due to the RF power supply, it repels the electrons from the neighborhood of the target material and forms an enriched sheath of positive ions in front of the target surface which further supports the sputtering. Typically, 13.56 MHz (Industrial, Scientific and Medical frequency band) is the most general frequency used for RF-sputtering. Such systems require an impedance-matching network between the power supply and the sputtering chamber. This network provides an optimal matching of the load to the RF generator to deliver sufficient power to the sputtering chamber.

For confining the electrons, magnetic field is coupled with the electric field which helps also in increasing the sputter yield. In the presence of magnetic field, effective path length of electrons is increased as they trace helical paths resulting in more ionizing collisions between them and the neutral gaseous species close to the target surface. The collision between the helical electrons and neutral gas species, which is mostly Argon, leads to the creation of ionic species and this results in a higher deposition rate.

Procedure for the deposition

The substrates used for the deposition of NbN ultra-thin films were initially cleaned using acetone and isopropyl alcohol (IPA) solutions to ensure a pristine surface for film growth. The NbN films were deposited using a DC magnetron sputtering system equipped with a 2-inch diameter, 99.95% pure Nb target. The substrates were positioned 8.5 cm away from the Nb target to achieve optimal deposition conditions. Prior to the sputtering process, the chamber was evacuated to a base pressure of $10^{-}7$ mbar using a turbo-molecular pump. During the evacuation process, the substrate temperature was raised to 600 °C using a proportional–integral–derivative (PID) controlled heater, following a pre-set temperature and time program.

Once the desired temperature was achieved, the 5N pure N_2 and Ar gases were injected into the chamber at a ratio of 1:6 and the pressure of the chamber was maintained at 7×10^{-3} mbar where a self-sustain plasma formed at 200 W of DC power supply. After the plasma formation, a pre-sputtering of the target was done for ≈ 2 min and then the shutter was opened to deposit NbN thin films on MgO substrates. The deposition time was optimized to obtain the desired thickness of film under the given set of experimental conditions. The film thickness was measured by using a stylus profilometer (NanoMap 500ES) and to estimate the deposition rate which comes out to be 0.3 nm/s.

2.0.2 Atomic Force Microscopy

The morphological development NbN thin films, deposited via DC magnetron sputtering, was characterized with a Veeco Instruments Multimode-V Atomic Force Microscope (AFM, fig 2.2) operating in tapping mode to explain the film's surface topography. This method is highly effective for detailed surface analysis, utilizing an AFM probe equipped with a fine tip on a flexible cantilever. Scanning this tip across the surface in a raster pattern generates a high-resolution map of the surface features. The separation between the probe and the sample is a critical parameter, denoted by $P = P(Z)$, where Z represents the distance. Furthermore, a feedback mechanism is utilized to monitor the probe-sample distance, with adjustments made to the probe's vertical position until a point is reached where the change in the signal from the feedback system is $\Delta P = 0$. By considering the magnitude of the interaction between the probe and the surface, a topographical image is reconstructed displaying the properties of thin films. Characteristics such as particle size distribution, surface roughness, and the overall surface morphology of the thin films are obtained from the AFM images.

This method is not only employed to extract various critical properties of the system but also stands out as one of the simplest techniques, requiring minimal sample preparation which makes it a versatile tool for characterizing systems of diverse sizes and structures. The only primary requisite for this technique is the availability of a surface that is flat,

Figure 2.2: Atomic Force Microscopy set up from Veeco Instruments, present in the CSIR- National physical laboratory, New Delhi, India.

free of contaminants, and smooth.

Furthermore, the AFM imaging is carried out in two different modes called as contact mode and tapping mode. In the former, the deflection in the cantilever is recorded when the distance between sample and probe changes. However as the name suggest, the contact mode experiments are usually accompanied with a direct contact between the tip and the sample, which increases the pressure in the tip and reduced the sensitivity. In the latter case, the image is reconstructed by the variation in the amplitude of the resonant probe oscillation varying with the sample-probe distance, providing a clear image of the surface. Consequently, tapping mode is often favored for the analysis of delicate, soft, or mobile samples. Given that our ultra-thin NbN films were sensitive and susceptible to damage, which contact mode measurement could potentially induce, hence we opted for the tapping mode for this investigation.

The AFM images (figure 2.3) on 1 x1 μm^2 scale were recorded at three different locations by using an etched Si-AFM probe having a resonant frequency of 300 kHz. The Nanoscope Analysis, V-1.40 was used for AFM image analysis. AFM images of NbN thin film show small granular interconnection islands having an average RMS roughness

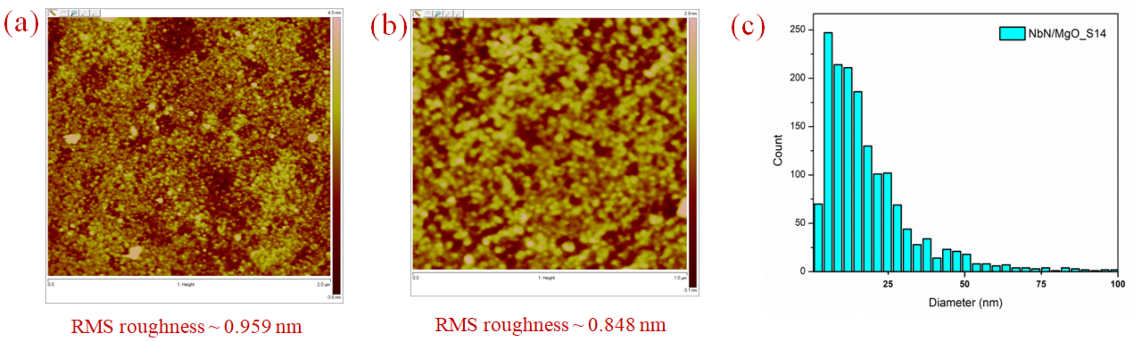

Figure 2.3: **Figure (a) and (b):** Tapping mode AFM image of 10 nm thick NbN film on MgO substrate at $2\mu m^2$ and $1\mu m^2$ area. **c** Histogram showing average size distribution of particles in $2\mu m^2$ NbN thin film on MgO substrate.

of 0.85 nm. Particle analysis shows that the average size (diameter) was 18.671 nm.

2.0.3 Designing of the Hall Bar geometry

After the deposition of NbN thin films, next step involves the fabrication of hall bar geometry to measure the electrical properties of superconducting thin films. A suitable 8-contacts Hall bar geometry was designed using LibreCAD software, which is well-suited for detailing such precise geometric layouts.

The Hall bar configuration is often preferred due to it's accuracy in probing the superconducting properties of the material under investigation. In this configuration, the current flows along the longitudinal axis of the sample. The Contacts are strategically positioned at the ends of the extended arms, while the voltage is measured between the two voltage contacts. For our investigation, we have fixed the length of 1000 µm for Hall bar, while selecting two different bar widths of 10 µm and 50 µm. To fabricate the optical mask for 50 µm width, we utilized direct laser lithography system. This involved employing a µPG101 laser writer from Heidelberg Instruments, operating at a wavelength of 375 nm (Figure 2.4). The µPG101 laser writer is an advanced micropattern generator that utilizes raster scanning to pattern the desired geometry. It incorporates a movable stage, which is closely monitored by a high-resolution linear encoder system. Additionally, a camera was used for visual investigation, aiding in position measurements on the substrate to ensure accurate alignment, particularly in cases involving multi-layer exposure with high precision.

2.0.4 Fabrication of the hall bar geometry

The hall bars were fabricated on four different substrates, for the film thickness ranging from 5 nm to 100 nm. The fabrication process involved spinning the photoresist AZ 5214E on the substrates using a spin coater at a speed of 4000 rpm. A soft bake was then performed at 110°C for 3 minutes, resulting in a nominal thickness of 1.2 µm for the photoresist layer. The pattern generation process involved utilizing a KarlSuss mask aligner (mod. MJB3) for optical lithography. This system is specifically designed for high-resolution photolithography, capable of achieving a line space resolution of 2.5 µm. It is equipped with a 350 W mercury short arc lamp, which emits light in the exposure wavelength range of 300-500 nm. The exposure step was carried out by closely aligning the mask and the sample, ensuring direct contact between them for a duration of 12 seconds. To develop the pattern, a solution consisting of a 1:1 ratio (H_2O:AZ developer) was used for the optimized time of 45 seconds.

Later, an etching step was exploited to define the final geometry of the NbN Hall bars. In particular, the etching process was carried out by using deep reactive ion etching (PlasmaPro 100 Cobra Inductively Coupled Plasma Etching System, Oxford Instrument). The fabrication parameters (etching time, ICP power, substrate temperature, etc.) were optimized while taking into account the film thicknesses and typology of the substrates. The best etching selectivity between the optical resist and the NbN thin film was obtained with a mixture of CF4 and Ar with fluxes of 90 and 10 sccm, respectively, at an operating pressure of 50 mTorr. ICP power and RIE RF power were 500 and 30 W, respectively.

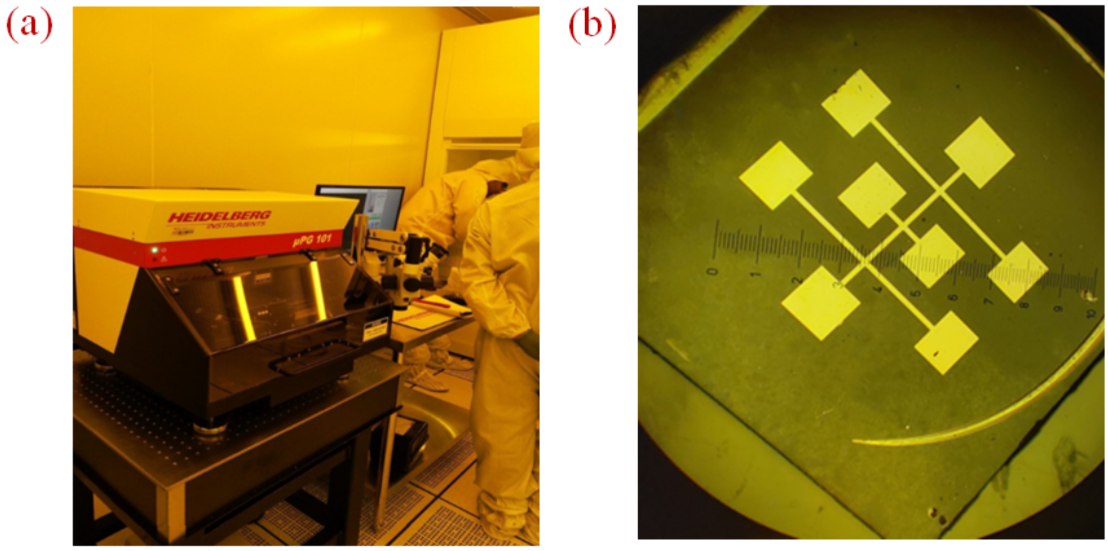

Figure 2.4: **(a)**: μPG101 laser writer from Heidelberg Instruments at the clean room facility of INRiM - National Institute of Metrological Research, Torino). **(b)**: Hall bar-configured 100 nm NbN film deposited on a MgO substrate immediately following the precise reactive ion etching process.

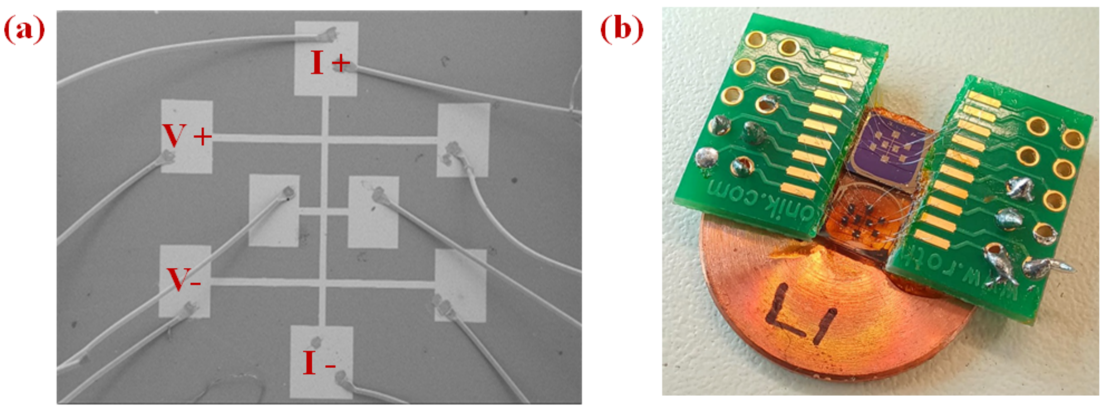

Figure 2.5: (a) Representation of an eight-contact Hall bar configuration for a 10 nm thick NbN film, illustrating the arrangement of current and voltage contacts. (b) Examples of two NbN devices on Si (center, bottom) and MgO (center, top) substrates and of two PCBs, glued to the copper disc. The aluminum wires, bonded both to the Hall bar and PCB pads are clearly visible. The adopted solution while preventing Al wires from detaching assures an optimal thermal contact of devices. The image has been taken after the electrical characterization.

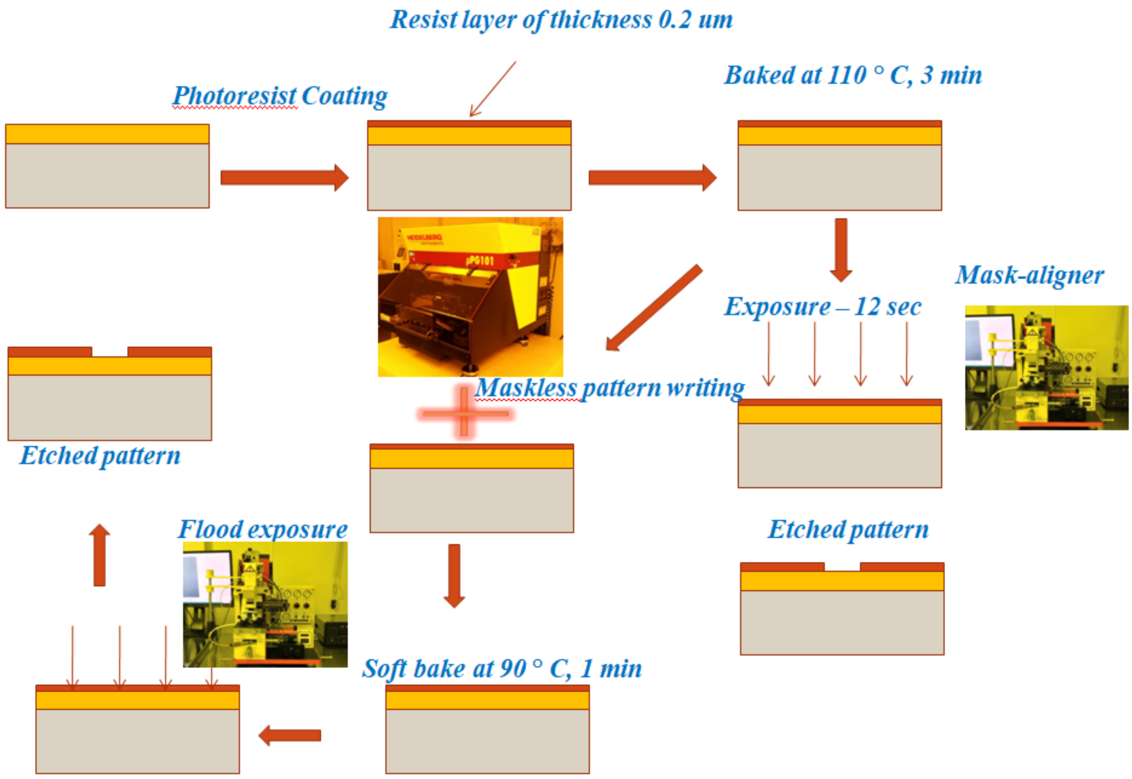

Figure 2.6: **Step-by-step schematic illustration of the fabrication process employed in the realization of the Hall bar geometry**: The lithographic techniques employed for the creation of Hall bar structures, utilizing two distinct methodologies is shown: (a) pattern generation using a mask aligner, and (b) a maskless lithographic technique employing a micro pattern generator (μPG).

All the samples were cleaned with a light-oxygen plasma before the etching, to eliminate any organic or lithographic residuals. Further, the samples were glued to a copper holder (see figure 2.5) with a high-thermal-conductivity glue (GE Varnish) in order to have better temperature control and stability in the cryostat. Aluminum wires were bridge bonded to the pads of the Hall bar and to the pads of a small printed circuit board, placed close to the sample.

2.0.5 Visual inspection of the fabricated hall bar geometry

The fabricated samples were inspected using the scanning electron microscopy technique. The morphological evaluation of ultra-thin NbN films to identify granularity and structural uniformity was carried out.

SEM in general is used to gather information about the sample's characteristics such as

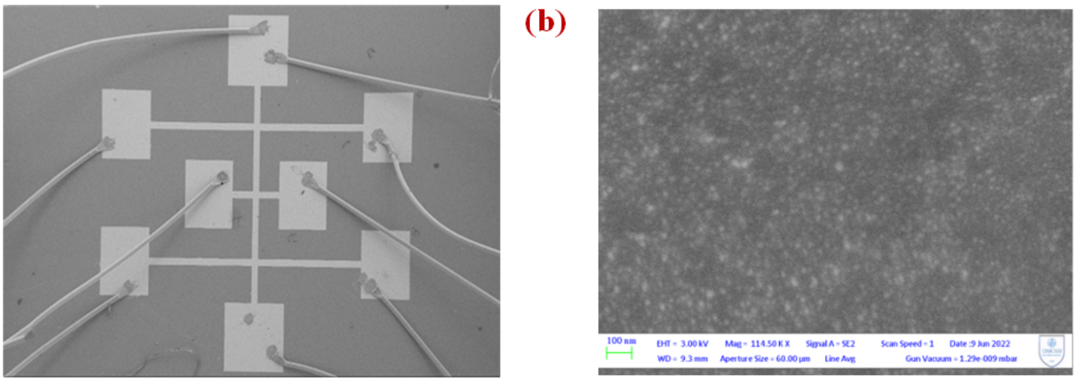

Figure 2.7: **(a)**: A SEM image of NbN hall bar geometry for a 10 nm thick film is shown. **b**: A magnified image at 114,500x for the sample is shown, displaying a granular, homogeneous distribution.

surface morphology, defects, and composition. A focused beam of high-energy electrons is directed onto the sample's surface. When the electron beam interacts with the sample, dissipation occurs, resulting in the generation of different kinds of signals. Among these, the most crucial ones are the secondary electrons, responsible for displaying the sample's topographical image, and back-scattered electrons which contribute to the contrast of the image.

In this study, the morphology and granular distribution of deposited NbN ultra-thin films were examined using a ZEISS SIGMA 300 Field Emission Scanning Electron Microscopy (FESEM) system. FESEM is an improved version of a conventional SEM system, which was achieved through the implementation of an electron optic design. This design incorporated a field emission gun enabling the acquisition of high-resolution images for various material types, offering enhanced performance.

The key component of this system is the Gemini column, which comprises a field emis-

Figure 2.8: Field Emission Scanning Electron Microscopy system from ZEISS SIGMA 300, at the facility of Department of Physics, UNICAM.

sion gun and lenses as shown in figure 2.8. The field emission gun (FEG) in this system exhibits a low energy spread of approximately 0.35 eV, which is crucial for minimizing chromatic aberrations. The probe current ranges from 3 pA to 20 nA, contributing to improved image quality. Another important factor in enhancing image quality is the implementation of electric optics in the Gemini column. These optics are responsible for demagnifying the electron source to create a smaller probe, thus improving resolution. The demagnification is achieved through the use of an objective and a condenser lens. In the Gemini column, lenses are employed, featuring a compound magnetic-electrostatic objective lens with a resolution of 1.2 nm at 15.0 kV.

When the incident electron beam interacts with the target sample, low-energy electrons, high-energy backscattered electrons, and X-rays are emitted. These signals are collected by detectors, which contribute to the formation of the image. The FESEM system incorporates three electron detectors: 1) High-efficiency in-lens electron detectors are utilized for ultra-high detection sensitivity, directly collecting secondary electrons (SE) from the sample's surface. 2) Everhart-Thornley secondary electron (ETSE) detectors are employed to detect electrons emitted at various angles relative to the primary beam. 3) High-definition backscattered electron (HDBSD) detectors are used to detect high-energy electrons (¿50 eV).

Figure 2.7 shows the SEM image of NbN film, with a thickness of 10 nm, deposited on a MgO substrate. The image is taken at a magnification level of 114,500x, displaying the granular morphology and confirming the homogeneity of the film's microstructure. This morphological consistency is extremely important for the film's superconducting performance, as it can significantly influence the electrical transport properties and the manifestation of quantum phenomena within the films.

2.0.6 Transport measurements of NbN thin superconducting films

The fabrication procedure was meticulously optimized through precise calibration and fine-tuning of each process step, resulting in the successful fabrication of NbN hall bar structures. Particular attention was devoted to the etching procedure, given the heightened susceptibility of ultra-thin films to over-etching, especially critical for samples with thicknesses approaching 5 nm. Following the optimization of deposition parameters, a set of 48 samples was systematically produced for detailed characterization.

For electrical measurements, the NbN devices and their associated printed circuit boards (PCBs) were mounted on the top of a copper disk (Figure 2.5(b)). To ensure optimal thermal coupling, the final device was anchored to a copper cold finger using Apiezon N grease, which was selected for its superior thermal conductivity at cryogenic temperatures. Transport measurements have been carried out in a He closed-cycle (liquid-free) cryostat (Advanced Research System mod. DE210) equipped with two Si diode ther-

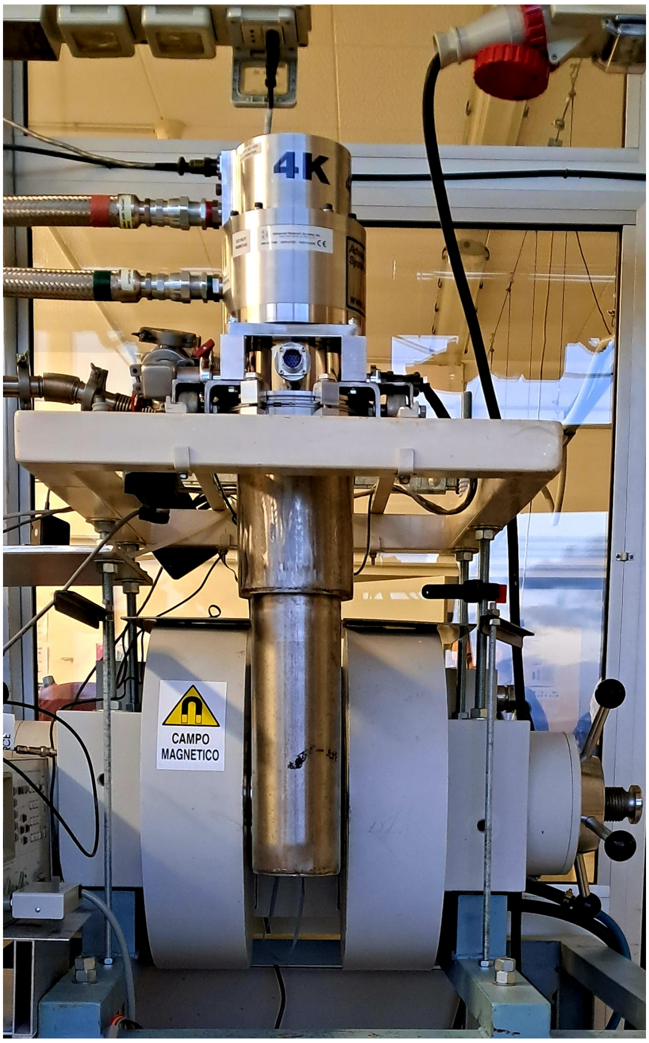

Figure 2.9: Liquid-free He closed cryostat from Advanced Research System, along with the Bruker's electromagnets, at the facility of SuperNanoLab, Department of Physics, UNICAM.

mometers (Lakeshore mod. DT-670), one of which was calibrated (maximum uncertainty of 6.3 mK). The temperature of the second stage of the cryostat has been read by the uncalibrated Si diode wired to a controller Lakeshore mod. 332, while the sample temperature has been read by one channel of a double-channel source-measure unit (SMU, Keysight mod. B2912A).

Resistivity, $\rho(T)$, and current-voltage ($I - V$), characteristics have been measured as a function of the temperature in the 4-contact geometry. For investigation of $\rho(T)$, the

SMU has been operated either in DC or in pulsed mode. The latter (so-called delta mode) is based on the suitable combination of three consecutive current pulses of alternate polarity, effectively able to minimize thermo-electric forces and offsets otherwise affecting the low voltage detected values [83].
Current (1 μA÷10 mA for $I - V$; typically $\leq 1\mu$A for ρ) has been sourced along the Hall bar length and the voltage drop detected by using two out of three lateral contacts, located on the same side (Figure 2.5 (a)).

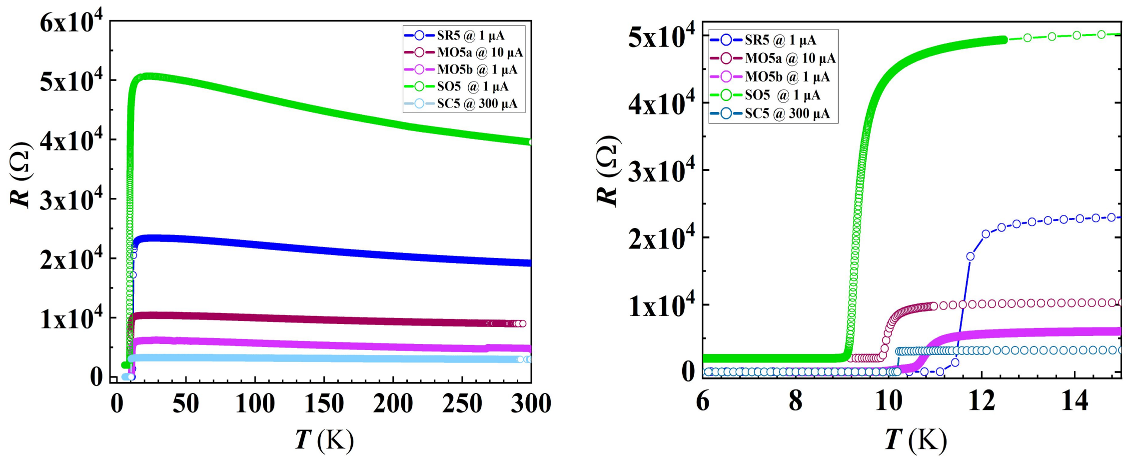

Figure 2.10: Resistivity measurements of 5 nm NbN thick films are shown as a function of temperature across multiple substrate materials (MgO (MO5), r-cut Al_2O_3 (SR5), c-cut Al_2O_3 (SC5), and SiO_2 (SO5)). Measurements have been carried out at a current intensity of 1 μA and 10 μA except for sample SC5. The left panel shows the evolution of the resistivity from the superconducting state up to room temperature. The right panel offers a detailed view of the superconducting transition region.

Electrical transport measurements were started from the lowest T ($\approx$ 4.5 K) reached by the system, without thermal stabilization of the device, by exploiting the high thermal inertia of the cryostat, resulting in effective isothermal conditions of measure.

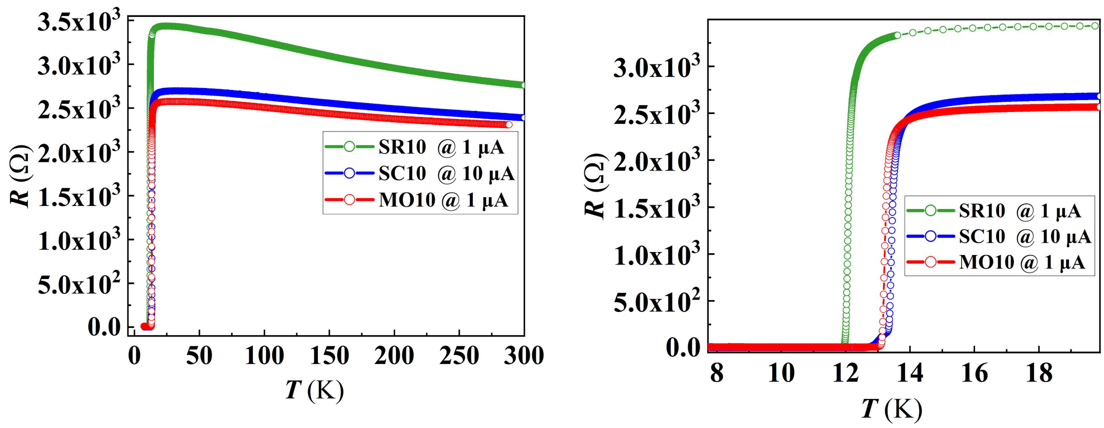

Figure 2.11: Left panel: Resistance as a function of temperature for 10 nm NbN thick films on different substrates. The right panel offers a detailed view of the transition region.

In particular, the number of data points to average has been suitably chosen to keep the variation of the sample temperature as low as possible: $\lesssim$ 1 mK, during data acquisition of the superconducting transition (fast measurement: $\approx$ 5 values/s resulting each by the average of 30 readings); $\lesssim 10 \div 20$ mK, for $I - V$ characteristics.

Using this optimized measurement protocol, we conducted systematic resistance measurements across a series of NbN films with thicknesses of 5 nm, 10 nm, and 15 nm, deposited on different substrate materials. The results of these measurements, presented in Figures 2.10, 2.11 and 2.12 provide insight into the substrate-dependent transport properties of these ultrathin films. For $I-V$ characterization, we adopted a specialized technique that exploits a specific feature of the Source-Measure Unit (SMU) used in our experiments. The measurement protocol involves sourcing current pulses of 1.1 ms duration to the device with increasing intensity in both directions (up-sweep and down-sweep), typically collecting $150 \div 200$ points for each $I - V$ curve. The current is switched off among consecutive pulses. The current is delivered to the film through a ramp of pulses

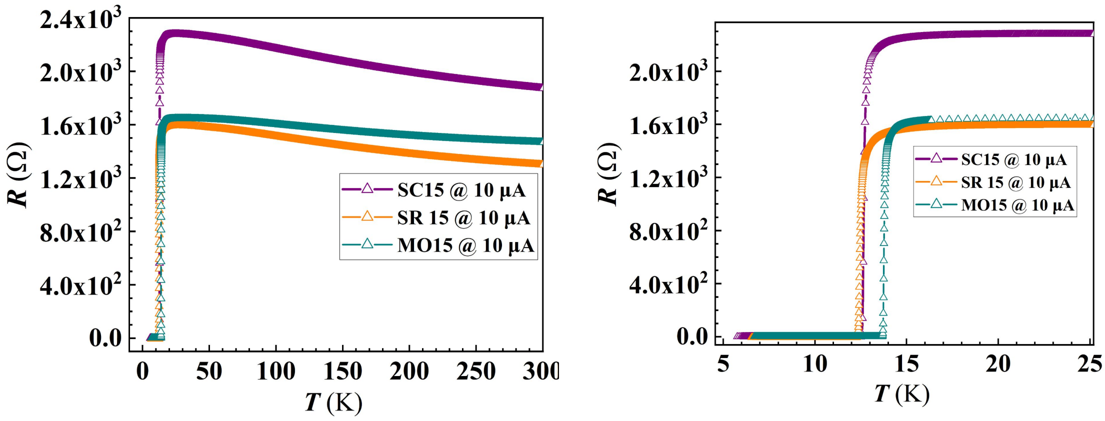

Figure 2.12: The temperature dependence of electrical resistivity is presented for a 15 nm thick NbN thin film deposited on multiple substrate materials. All measurements were conducted at a fixed current intensity of 10 μA. The main figure (left) demonstrates the complete resistivity behavior across the full temperature range, while the accompanying figure (right) provides a magnified view of the superconducting transition region, enabling a detailed examination of the resistivity evolution around the critical temperature.

with increasing intensity, spanning several orders of magnitude, where the highest intensities (>1 mA) constitute only a small fraction of the total sourced currents. The complete $I - V$ measurement sequence is executed within a few seconds (approximately 5 s). This pulsed technique approach was specifically implemented to significantly reduce possible artifacts arising from Joule heating effects in the investigated film.

2.0.7 Superconducting properties of NbN nanofilms

From the resistivity measurements and the I-V characteristics, we systematically extracted key physical parameters. The critical temperature (T_C), which marks the transition point from normal to the superconducting state, represents a fundamental property of supercon-

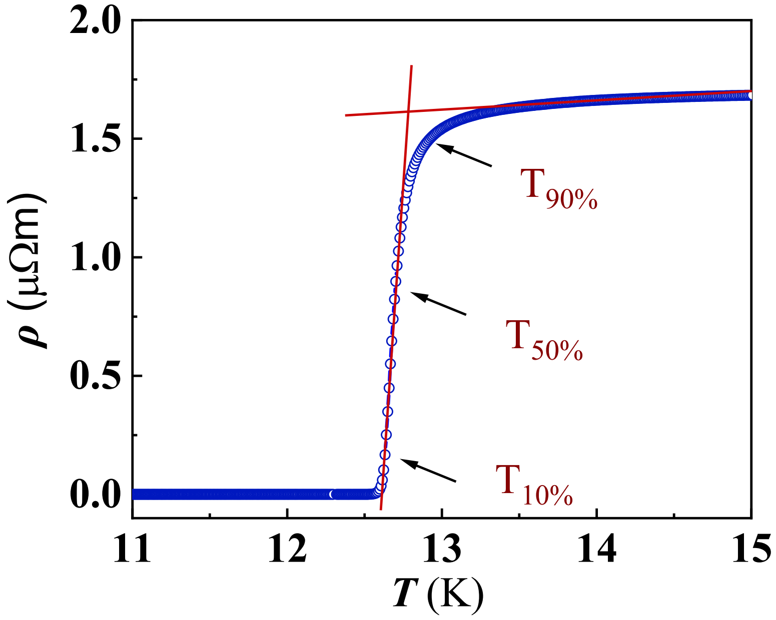

Figure 2.13: Temperature-dependent resistivity of a 15 nm thick NbN film on Al_2O_3 (C-cut) substrate. This figure illustrates the procedure used to extract the superconducting critical temperature (T_C).

ducting materials. As known, at temperatures above T_C, the material exhibits normal-state electrical resistivity, while below T_C, it transitions into the superconducting state characterized by zero electrical resistance. In our analysis, T_C was determined as the midpoint between two characteristic temperatures: $T_{10\%}$ and $T_{90\%}$, which correspond to 10% and 90% of the normal state resistivity value, taken soon after the SC transition in the plateau region above T_C, as illustrated in Figure 2.13. The superconducting transition width was subsequently defined as $\Delta T_C = T_{90\%} - T_{10\%}$, providing a measure of the sharpness of the superconducting transition.

In addition to the critical temperature, another fundamental parameter governing superconducting behavior is the critical current (I_C). This parameter represents the maximum current that a superconductor can sustain while maintaining its zero-resistance state. When the applied current exceeds I_C, the superconductor transitions to its normal state.

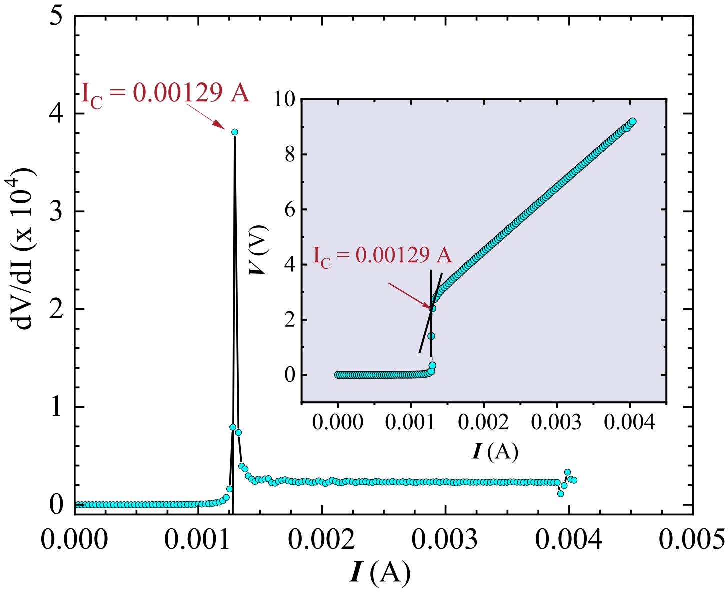

Figure 2.14: Determination of the critical current (I_C) from the I-V characteristics for a 15 nm film on Al_2O_3 (C-cut) substrate. The main panel shows the differential resistance (dV/dI) as a function of current (I). The inset shows the corresponding I-V curve.

To comprehensively characterize this parameter in our system, we conducted temperature-dependent measurements of I_V from which I_C was extracted. The determination of I_C was accomplished through two complementary approaches. The primary method identified I_C as the threshold current at which a distinct voltage jump appeared in the I-V characteristic, signifying the transition from superconducting to normal state (Fig. 2.14, Inset). This methodology follows the protocol shown by Pinto et al. [84]. For validation, we employed a secondary approach where I_C was determined from the maximum of the $dV(I)/dI$ vs I curve. A comparative analysis of the I_C values obtained from both methods demonstrated excellent agreement as shown in Figure 2.14.

Magnetic field measurement set up

The magnetic field measurements were conducted using two distinct experimental configurations to accommodate different field intensity ranges. For low-field measurements, a Bruker B-E15v electromagnet system integrated with a Bruker B-EC1 current controller and related power supply was utilized. Although this setup is capable of generating magnetic fields up to 10,000 G, the field intensity was specifically constrained to 200 Gauss for this investigation. The magnetic field strength was precisely controlled through two adjustable parameters: the input current to the electromagnet (maximum 30 A) and the variable gap between the magnetic poles. The applied magnetic field was systematically monitored using a gaussmeter (Alpha Lab, mod. GM2). The maximum field intensity experienced by the investigated films was 160 G. Since the thermometer was positioned perpendicular to the magnetic field lines, the expected relative shift in the temperature is on the order of 10 mK comparable to the thermometer's accuracy.
For field characterization at a few hundred of Gauss, the experimental setup comprised a pair of permanent magnets located symmetrically on the opposite sides of the cold finger, with the NbN hall bar structure located in the central region of the magnetic field. This configuration was designed to establish a magnetic field perpendicular to the sample plane. Field strength was achieved by placing the Gaussmeter probe close to the film surface. To minimize potential measurement artifacts, we meticulously checked the stray field generated by the permanent magnets using assembly. The thermometer was strategically positioned on the cold finger at the maximum possible distance from the magnets, in a region where the measured stray field remained below 100 G, with the thermometer package oriented perpendicular to the field lines. It is worthwhile noting that, due to the nature of the field generated by the magnetic assembly, the field presents a large variation along the magnetic radius, then affecting the value of the intensity measured. The estimated uncertainty in the field intensity is of the order of ± 100 G.

2.0.8 Conclusion

The comprehensive experimental methodology described in this chapter encompasses the precise fabrication of NbN nanofilms via DC magnetron sputtering, their careful structuring into Hall bar geometries, and thorough characterization using multiple complementary techniques, including AFM, SEM, and detailed transport measurements. The experimental setup was meticulously optimized to ensure reliable measurements across different magnetic field regimes, with particular attention paid to minimizing measurement artifacts and maintaining precise temperature control. The systematic approach to sample preparation and characterization, combined with the careful consideration of experimental uncertainties, provides a robust foundation for investigating the fundamental superconducting properties of these NbN nanofilms.

In the subsequent chapter, we will present and analyze the electrical characterization results, with a particular focus on the emergence of novel phenomena arising from the interplay between the film's intrinsic properties, their dimensional constraints, and external parameters such as temperature and magnetic field.

Chapter 3

Dimensional crossover to 2D and a clear manifestation of the BKT transition in SC NbN ultra-thin films

3.1 Introduction

The groundbreaking BCS theory has been one of the most successful theories in the field of condensed matter physics, explaining the phenomenon of superconductivity [85] by the formation of Cooper pairs through weak electron-electron interactions mediated by phonons. This leads to a macroscopic quantum state characterized by a rigid phase of the wave function. This phase coherence is crucial for understanding the remarkable properties of superconductors: zero electrical resistance and perfect diamagnetism, characterized by the energy scale, superconducting order parameter (Δ) [3]. However, in the realm of conventional superconducting systems, an essential energy scale known as the superfluid phase stiffness ($J_S >> \Delta$) is often overlooked. This parameter plays a crucial role in characterizing the SC state, where significant fluctuation effects are involved, and the BCS theory could not provide a clear explanation for the influence of such effects.

In granular systems with high disorder, such as NbN [63, 65, 67, 69], NbTiN, InO_X [72, 73], and MoGe, the complexity further increases, and the emergence of significant fluctuation effects are observed. While these phase fluctuations can disrupt the superconductivity [86], they also result in the persistence of a finite value for the superconducting gap. Therefore, in order to comprehend the impact of phase fluctuations and the role of the energy scale J_S, numerous researchers have proposed various theoretical interpretations to address and explain these phenomena. Among these interpretations, the Berezinskii-Kosterlitz-Thouless (BKT) transition [57, 87] stands out as a prominent theoretical framework.

In 2016, the Nobel Prize in Physics was awarded to David J. Thouless, Duncan Haldane, and John M. Kosterlitz for their groundbreaking theoretical work on topological phase transitions and topological phases of matter. Their work included the theoretical description of the Berezinskii-Kosterlitz-Thouless (BKT) transition, a unique type of phase transition that occurs in two-dimensional systems. Even 50 years after its discovery, the BKT transition has remained one of the most fascinating phenomena in condensed matter physics, highlighting the importance of topological effects in phase transitions. This phenomenon has been observed in various systems, including vortices in superfluid helium films, vortex configurations in 2D superconductors, and dislocations in 2D crystals, providing a phenomenological explanation for the underlying transition mechanism.

This was a significant breakthrough, as the prevailing understanding at the time, based on the Mermin-Wagner theorem, was that thermal fluctuations in 2D systems with a continuous symmetry in their order parameter would disrupt long-range order, leading to a vanishing average of the order parameter and thus a disordered phase. However, the BKT transition demonstrated that a different type of order, driven by topological defects, could exist in these systems.

It was Berezinskii [88] who first made a significant breakthrough by demonstrating the possibility of a superfluid state at low temperatures in a thin film of liquid helium, which lacked the conventional long-range order. He successfully demonstrated the power-law decay of the two-point correlation function, which captured the relationship between the order parameter correlation and the distance between points at different temperatures. This phenomenon, widely recognized as quasi-long-range order, provided compelling evidence for Berezinskii's findings. Subsequently, Kosterlitz [58] and Thouless further corroborated these observations, leading to the development of the renowned BKT theory.

Moreover, a qualitative explanation of the BKT effect in various 2D systems involves a distinct power law decay of the correlation function at high and low temperatures, indicating the occurrence of a phase transition. In the low-temperature regime, defects are typically present in the paired form, which does not break the quasi-long range order. However, as the temperature increases, these paired defects begin to dissociate, transforming into free defects which leads to the breakdown of the quasi-long range order, and the correlation function undergoes an exponential decay, resulting in a disordered phase as proposed by Berezinskii, Kosterlitz and Thouless.

Before delving into the experimental results, it is essential to explore the fundamental concepts underlying the intriguing fluctuation effects observed in superconducting systems of varying dimensions. We begin from the famous Ginzburg-Landau theory [90] in which the standard free energy equation is given by :

$$F = F_n + \alpha_0(T - T_C)|\Psi|^2 + \frac{\beta}{2}|\Psi|^4 + \frac{1}{2m^*}|(\frac{\hbar}{\iota}\nabla - e^*A)\Psi|^2 + \frac{\mu_0 H^2}{2} \tag{3.1}$$

where F_N is the free energy in the normal state, H is the applied magnetic field, A is the vector potential, μ_0 is the magnetic permeability of free space, and α_0, β are the Ginzburg-Landau parameters. m^* and e^* represent the effective mass and charge of a Cooper pair, respectively. The order parameter $\Psi(\mathbf{r})$ is a complex quantity that can be expressed as $|\Psi(\mathbf{r})|e^{\iota\theta(\mathbf{r})}$, where $|\Psi(\mathbf{r})|$ represents the amplitude and $\theta(\mathbf{r})$ represents the phase.

In the case of zero applied magnetic field, the free energy of a uniform superconductor per-

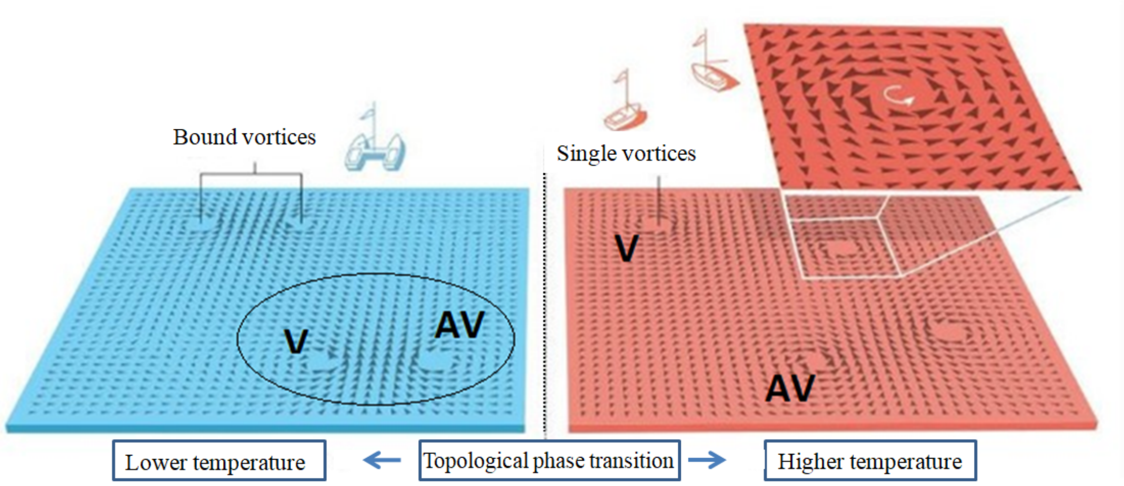

Figure 3.1: Illustration of the Berezinskii-Kosterlitz-Thouless transition in a 2D superconducting film. Left: Below the transition temperature (T_{BKT}), vortex-antivortex pairs are bound together. The arrows represent the phase of the order parameter, illustrating the circulating flow around each vortex. The black circle highlights the localized nature of the pair. Right: Above the transition temperature (T_{BKT}), the vortex-antivortex pairs unbind, leading to free vortices (V) and antivortices (AV). These unbound vortices can move independently, disrupting the long-range order of the system. The magnification shows the characteristic swirling pattern of the phase field around a vortex [89].

mits an infinite number of minima with the same magnitude $|\Psi|$, while allowing the phase θ to vary from 0 to 2π. At temperatures well below the critical temperature ($T < T_C$), the fluctuations in the amplitude of the order parameter, Ψ become energetically expensive and can be disregarded, except in cases where the phenomenon of fluctuation-induced superconductivity occurs. While the amplitude of the superconducting order parameter remains constant, fluctuations in its phase, θ, can still occur. The energy required to create these phase gradients is determined by the superfluid stiffness, J_S. In essence, J_S quantifies the resistance of the superconducting system to phase variations, making it a crucial energy scale for understanding the impact of phase fluctuations.

When a current, I, flows through a superconductor, it causes a spatial variation (or gradient) in the phase of the superconducting wavefunction, Ψ. This phase gradient is directly related to the supercurrent density, J_0 (the current per unit area), which is expressed in terms of Ψ as:

$$J_0 = \frac{e^*\hbar}{2m^*i}(\Psi^*\nabla\Psi - \Psi\nabla\Psi^*) - \frac{e^{*2}}{m^*}|\Psi|^2 A \tag{3.2}$$

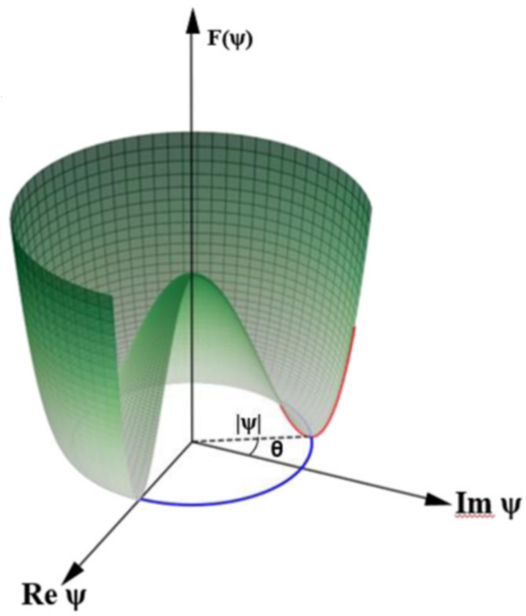

Figure 3.2: The free energy functional of a homogeneous superconductor, in the absence of external currents and magnetic fields, can be visualized as a potential landscape where the radial distance represents the magnitude of the order parameter, $|\Psi|$, and the azimuthal angle, θ, represents its phase. The minimum free energy states are located along the circle represented by the blue line. Deviations from this minimum, shown by the red and blue lines, correspond to fluctuations in the amplitude and phase of the order parameter, respectively. Amplitude fluctuations are associated with an energy cost (gapped), while phase fluctuations are not (gapless) [91].

Due to the significant energy barrier associated with changing the amplitude of the superconducting wavefunction, Ψ, it is often reasonable to assume that the amplitude remains constant while the phase, θ, varies. This approximation is especially valid when the coherence length, ξ, is much smaller than the London penetration depth, λ. In such cases, the superconducting wavefunction can be approximated as a constant amplitude wave with a spatially varying phase. This allows us to represent the wavefunction in terms of θ by replacing, $\Psi = |\Psi|e^{\iota\theta(r)}$ such that:

$$J_0 = \frac{e^*}{m^*}|\Psi|^2(\hbar\nabla\theta - e^*A) \tag{3.3}$$

In the absence of an external applied magnetic field (A=0), $J_0 = \frac{he^*}{m^*}|\Psi|^2\nabla\theta$, where $|\Psi|^2$ represents the density of the superconducting condensate, and this density is directly proportional to the number of Cooper pairs contributing to the superconducting state. By substituting the relation $|\Psi|^2 = \frac{n_S}{2}$ and using the relation $J_0 = \frac{n_S}{2}e^* v$, where v is the superfluid velocity and is written as $v = \frac{\hbar}{m^*}\nabla\theta$, the kinetic energy density is expressed as:

$$\frac{1}{4}n_S(m^* v^2) = \frac{\hbar^2 n_S}{4m^*}|\nabla\theta|^2 \tag{3.4}$$

If we only consider the contribution from phase variations, the Hamiltonian of the system can be expressed as:

$$H = \frac{1}{2}\frac{\hbar^2 n_S}{2m^*}\int d^2r|\nabla\theta|^2 \approx \frac{1}{2}\frac{\hbar^2 n_S}{4m}\int d^2r|\nabla\theta|^2. \tag{3.5}$$

From the equation 3.5, the value of superfluid stiffness is given by the pre-factor ($\frac{1}{2}\frac{\hbar^2 n_S}{2m^*}$) multiplied by the relevant length scale, a. The relevant length scale for thin films where $d < \xi$ is simply the film thickness ($a = d$). However, when $d \geq \xi$, since the superconducting order parameter varies over the distance of the order of coherence length, thus making ξ the relevant length scale ($a \sim \xi$) [91].

The superfluid stiffness (J_S) can be expressed in terms of a directly measurable quantity, the London penetration depth (λ), through the following relation: $J_S = \frac{\hbar^2}{4\mu_0\lambda^2 e^2}$.

Interestingly, in the case of thin superconducting films, the energy, described by the Hamiltonian can be directly related to a well-studied model in magnetism: the 2D XY model. This model describes a grid of magnetic spins that can point in any direction within the plane of the grid.

In the continuous version of this model, the Hamiltonian simplifies to an expression involving the spatial variation of the spin's angle, ω, and coupling strength, J, which represents the interaction energy between neighboring spins:

$$H = \frac{1}{2}J\int d^2r|\nabla\omega|^2 \tag{3.6}$$

The Berezinskii-Kosterlitz-Thouless (BKT) theory shows that such a system undergoes a special kind of phase transition at a temperature T_{BKT} proportional to J_S. Above T_{BKT}, the spins are disordered, while below it, they exhibit quasi-long-range order, meaning their correlations decay slowly with distance but do not reach a constant value like in a fully ordered system. This transition is driven by the formation and movement of unbound vortex-antivortex pairs in the spin field.

In the context of superconductivity, this translates to a transition from a state with quasi-long-range phase coherence to a state where the phase is completely random. This occurs due to the proliferation of free vortices and antivortices driving the transition from the superfluid to the normal state.

3.1.1 2D X-Y model

Building upon the 2D X-Y spin model discussion in the previous section, we can describe the Berezinskii-Kosterlitz-Thouless (BKT) framework [58, 92]. The Hamiltonian for this system, representing its energy, is formulated in terms of the spin components S_i and S_j, where:

$$H = \frac{-J}{2}\sum S_i * S_j \simeq \frac{J}{2}\int d^2r(\nabla\omega)^2 \tag{3.7}$$

S_i and S_j are the magnetization vectors, J = coupling constant and ω is the angle between the two vectors (S_i and S_j) at a given position. The low-temperature behavior of this system is controlled by the Gaussian fluctuations, whose mean value is :

$$< S(r) * S(r_0) >=< exp[\iota(\omega(r) - \omega(r_0))] >\propto \frac{|r - r_0|}{a_0}^{-K_BT/(2\pi J)} \tag{3.8}$$

which results into the power-law dependence as $< S(r)S(r_0) >\propto r^{-\eta}$. However, at high temperatures, the decay of the correlation length becomes exponential which is represented as, $< S(r)S(r_0) >\propto \epsilon(-r\xi)$.

During the phase transition in superconducting films, the appearance of vortices disrupts the quasi-long-range order of the superconducting state in two-dimensional (2D) films. These vortices can be mathematically described by the following equation:

$$\frac{\delta H}{\delta\theta(r)} = J\nabla^2\omega = 0 \tag{3.9}$$

giving solutions: ω = q arctan $\frac{y}{x}$, $v_q = \nabla\omega = \frac{q}{r}\vec{e}_\phi$, where q is the charge of the vortex which can be taken as ±1, ±2, etc.

e_ϕ is the unit vector, originating from the vortex center point, and the integral value around the vortex core is $\oint(\nabla\omega)dl = 2\pi q$.

It is necessary to note that the vortices are topological defects, meaning they cannot be smoothly deformed into the ground state configuration. A single, isolated vortex (with topological charge q = +1) persists as an excitation. However, vortex-antivortex pairs (with charges q = +1 and q = -1, respectively) can annihilate each other through continuous transformations, returning the system to the ground state.

We then proceed to calculate the energy of a single vortex using the following equation:

$$E_V = \frac{J}{2}\int\frac{2\pi}{r}dr = J\pi ln\frac{L}{a} \tag{3.10}$$

where L is the size of the system. Now, when the single vortex is generated, the change in free energy for the vortex is given by, F = E_V - TS, where entropy, S = $2K_B$ ln (L/a),

giving F = (Jπ - 2k_BT) ln(L/a). However, for the $T >> T_{BKT}$, the value of F becomes negative, which makes the generation of vortex energetically favorable.
Moreover, to estimate the Hamiltonian of a superfluid film, we replace the coupling constant $J \rightarrow \hbar n_S(T)/m^2$ and $\nabla = k_B T m^2/4\pi\hbar n_S(T)$ in the equation 3.7, where n_S is the superfluid density and m is the mass of helium atoms. As estimated by Kosterlitz and Thouless, the ratio of superfluid density and transition temperature (T_{BKT}) comes out to be:

$$\frac{n_S}{T_{BKT}} = \frac{2m^2}{\pi\hbar^2} \tag{3.11}$$

R-G analysis for the BKT transition mechanism [92]

To determine the critical parameters governing the Berezinskii-Kosterlitz-Thouless (BKT) transition, a renormalization group (RG) analysis is essential. This analysis considers the interplay between two key quantities: the superfluid stiffness (J_S), and the vortex fugacity (g) which is the measure of the energy cost of the vortex creation. The vortex fugacity, g, is exponentially related to the vortex core energy (μ), expressed as $g = 2\pi e^{-\beta\mu(T)}$, where $\beta = 1/k_B T$ (with k_B being the Boltzmann constant and T the temperature). The superfluid stiffness, a key parameter for characterizing the BKT transition, can be expressed as:

$$J_S(T) = \frac{\hbar n_s^{2D}(T)}{4m^* k_B} = \frac{\hbar^2 c^2}{16\pi e^2}\frac{d}{\lambda^2(T)} \tag{3.12}$$

where d represents the thickness of the film, m^* is the effective mass, c is the speed of light, n_s^{2D} is the superfluid density and λ is the penetration depth. Replacing, $\mu = \mu' J(T)$, and taking vortex core energy as the multiple of stiffness, the value of μ' acquired in the X-Y model can be taken as :

$$\mu' = \alpha\mu'_{xy} = \alpha\frac{\pi^2}{2} \tag{3.13}$$

The equations are written in the notation used from the sine-Gordon model:

$$\frac{dK}{dl} = -K^2 g^2 \tag{3.14}$$

$$\frac{dg}{dl} = (2 - K)g \tag{3.15}$$

where $K = \pi J_S/T$, $l = lna/\Psi_0$ with Ψ_0 and an as the original and re-scaled RG lattice spacing. For determining the value of superfluid density (n_S), we take the limiting case for K, in which $n_S = TK/\pi$ for $l \rightarrow \infty$. In the low-temperature regime ($K = \pi J_S/k_B T > 2$), the vortex fugacity is negligible, resulting in a finite superfluid stiffness, J_S. As the temperature increases, causing K to fall below 2, the vortex fugacity becomes relevant and ultimately diverges under the renormalization group (RG) flow. This divergence drives the superfluid stiffness to zero. The BKT transition temperature, T_{BKT}, is precisely determined by the fixed point of the RG equations where $K = 2$ and the fugacity vanishes ($g = 0$). This condition leads to the universal Nelson-Kosterlitz jump in the superfluid stiffness:

$$\frac{\pi J_S(T_{BKT})}{T_{BKT}} = 2 \tag{3.16}$$

Equation (3.16) encapsulates the universal relationship between T_{BKT} and the value of J_S at the transition, which is a crucial and primary diagnostic for confirming the BKT nature of the observed phase transition.

3.1.2 $V - I$ characteristics in determining the T$_{BKT}$

The solution obtained from the renormalization group equation offers valuable insights into determining the transition temperature (T_{BKT}), which occurs when the superfluid stiffness (J_S) approaches zero. Interestingly, this abrupt change in J_S can also be observed through the power law relationship exhibited by the I-V characteristics. To further understand this behavior, the energy associated with the vortex-antivortex pair (VAP) [92] can be expressed in the form:

$$\frac{E}{d} = \frac{2\pi J_S}{d} \ln \frac{r}{\xi} - \frac{I}{Wd} \frac{\phi_0 r}{c} \tag{3.17}$$

where W is the width of the SC film, Φ_0 is the flux quantum and I/wd gives the current density. When current flows through the film, a Lorentz force is generated, acting on the vortices within the film. This force is given by:

$$f = \epsilon_i jx\hat{z}\frac{\phi_0}{c} \tag{3.18}$$

drives the vortices to move in a direction perpendicular to the current. The sense of rotation of each vortex, characterized by its vorticity $\epsilon_i = \pm 1$, determines the precise direction of its perpendicular motion.

In this scenario, the critical current is determined as the threshold current at which the vortex-antivortex pair breaks. This transition occurs when the derivative of the energy with respect to the separation distance (r) of the VAP, is denoted as $\frac{\partial E(r^*)}{r} = 0$.

$$r^* = \frac{2\pi J_S cW}{I\phi_0} \tag{3.19}$$

giving energy in the form:

$$E(r^*) = 2\pi J_S ln \frac{2\pi J_S cW}{\xi_0 I\phi_0} - 2\pi J_S \tag{3.20}$$

For the condition where $r^* \leq W$, the value of the current becomes sufficiently large, which can break the vortices easily. Therefore, the minimum current required is :

$$I_C = 2\pi J_S \frac{c}{\phi_0} \tag{3.21}$$

Moreover, the density of the vortices (n_V) can be estimated by the equation :

$$\frac{dn_V}{dt} = \Gamma(T, I) - n_V^2 \tag{3.22}$$

where Γ represents the rate at which the vortices unbinding takes place and the second term in the equation gives the combining of the vortices to form a bound pair again. In that case:

$$n_V = \Gamma^{1/2} = e^{-E(r^*)/2T} \tag{3.23}$$

when a vortex traverses the width W of a sample, a phase shift of 2π occurs. In a small time interval (Δt), this phase shift leads to the escape of a fraction of vortices from the sample, therefore:

$$\frac{d\Delta\theta}{dt} = 2\pi n_V v_L L \tag{3.24}$$

where v_L is the usual drift velocity and n_v is the density of free vortices.

According to the Josephson relation, $\Delta V = (\hbar/2e)d\Delta\theta/dt$, generated electric field is given by :

$$E_x = \frac{\Delta V}{L} = \frac{\phi_0}{c} n_V v_L \tag{3.25}$$

As v_L is proportion to I, hence V can be written as n_V I. Moreover, n_V can be estimated by:

$$E(r^*) = 2\pi J_S \left[log \frac{2\pi J_S c W}{\xi_0 \phi_0 I} - 1 \right] \tag{3.26}$$

$$= 2\pi J_S \left[log \frac{I_C W}{\xi_0 I} - 1 \right] \tag{3.27}$$

it is clear from the equations that the first term is only dependent on the applied current. In that case, vortices contributing to the transport mechanism can be written as:

$$n_V \sim e^{-\pi J_S \ln(I_C/I)/T} = \left(\frac{I}{I_C} \right)^{-\pi J_S/T} \tag{3.28}$$

which shows that the nonlinearity in the I-V characteristics is determined from the exponent α given by:

$$V \propto I^{\alpha}(T), \alpha(T) = \frac{\pi J_S}{T} + 1 \tag{3.29}$$

Therefore, a key signature of the BKT transition observable in transport measurements is determined by the discontinuous jump in the critical exponent $\alpha(T)$ at the transition temperature, T_{BKT}. T_{BKT} is defined by the universal jump condition for the superfluid stiffness: $J_S(T_{BKT}) = 2T_{BKT}/\pi$. At this temperature, $\alpha(T)$ jumps from 1 (for $T > T_{BKT}$) to 3 (at $T = T_{BKT}$). Furthermore, for $T < T_{BKT}$, $\alpha(T)$ exhibits a monotonic increase. These characteristics of $\alpha(T)$ provide crucial experimental diagnostics for identifying the BKT transition.

Having established the theoretical background for the Berezinskii-Kosterlitz-Thouless (BKT) transition, we now turn to the experimental investigation of this phenomenon in our NbN thin films. The following section first outlines the essential parameters and experimental techniques used in our study, then delves into the specific analysis of the BKT transition in our samples.

3.2 Experimental results

3.2.1 Exploring the Superconducting Properties of NbN Nanofilms: A Comprehensive Study

This section presents our systematic investigation of superconducting properties in NbN thin films with thicknesses ranging from 5 nm to 100 nm. Transport measurements were performed on 44 samples with varying widths in the temperature range of 4.5 K to 300 K, under zero magnetic field conditions. Substrate selection played a crucial role in optimizing the superconducting properties of these films through the interplay of lattice matching, thermal expansion coefficients, and interface chemistry, which significantly influence both the crystallographic structure and electronic properties of the NbN films.

Figure 3.3 shows the temperature-dependent resistivity $\rho(T)$ for the films deposited on the Al_2O_3 r-cut substrate at an input current intensity of 1 μA. It is observed that at the SC transition, the films exhibit a significant jump in the resistivity value, varying approximately from 2 to 5 orders of magnitude. The order of magnitude for the resistivity jump reduces as the film thickness increases. Moreover, the normal state resistance for ultra-thin films is found to be approximately 3-4 times higher compared to a bulk NbN system. However, the normal state resistivity shows no clear correlation with film thickness and sometimes exhibits a reversed trend, particularly in films at or below the critical threshold of 15 nm with different trends observed above and below this threshold.

This trend can be observed from the extracted value of SC transition temperatures, which lowers with the decrease of the film thickness, becoming substantial when passing from $d = 25$ to $d = 15$ nm as shown in the inset of figure 3.4. Considering the effect of substrate, the highest value of T_C has been obtained on MgO (100), along with a very narrow SC transition width, ΔT_C (see figure 3.4). However, a consistent worsening of these parameters occurred for SC films deposited on SiO_2 substrate due to a significant lattice mismatch with the SiO_2, whereas MgO (100) presents the least lattice mismatch, giving the most favorable superconducting parameters without any dissipation effects.

In agreement with the behavior detected in figure 3.3, a non-monotonic dependence of the critical temperature (T_C) on film thickness has been observed across all substrate types with a clear decrease in T_C as the film thickness reduces to 25 nm. Notably, at a thickness of 15 nm, there is an abrupt increase in T_C, and then a consistent reduction is observed. This signifies the presence of an anomalous perturbation arising in the system at a thickness of 15 nm. As for ΔT_C, a minimal broadening of the transition was observed at higher thicknesses, $d > 25$ nm. Subsequently, as the thickness decreased further, ΔT_C began to

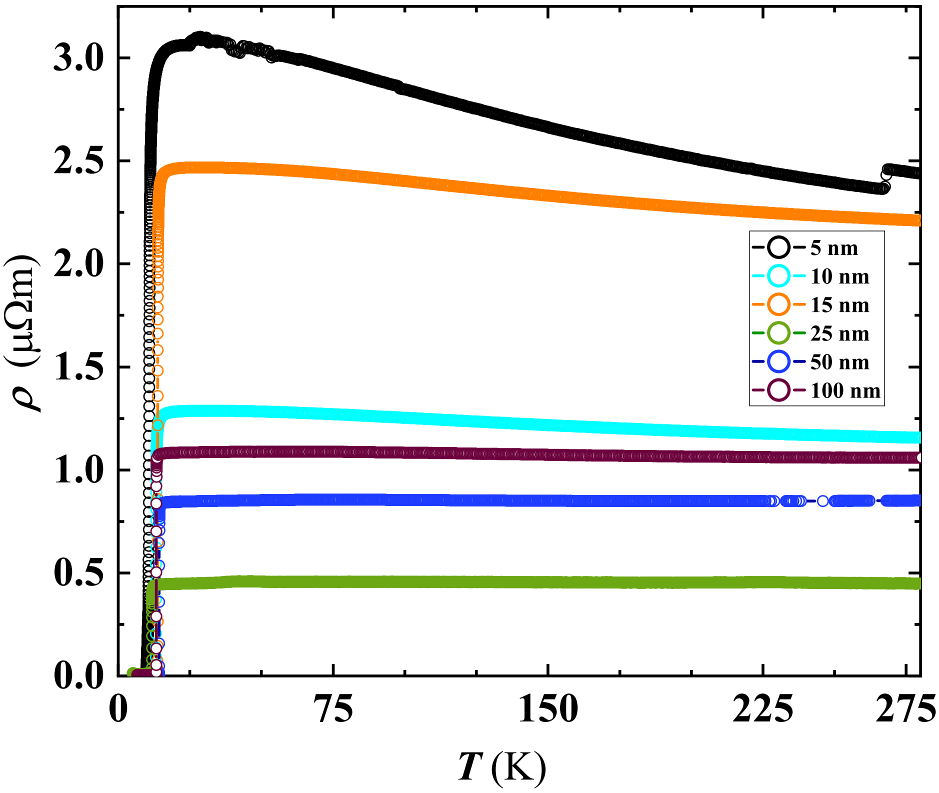

Figure 3.3: Resistivity behavior of NbN nanofilms for the set deposited on the Al_2O_3 r-cut substrate, for temperature varying from 4 K up to room temperature.

increase linearly, resulting in the highest value of 0.75 K for the thinnest sample of 5 nm deposited on the Al_2O_3 r-cut substrate.

Interestingly, for Al_2O_3, intermediate values of T_C and ΔT_C were measured, while the C-cut substrate demonstrated slightly higher T_C values for $d > 5$ nm (see Figure 3.4). Compared to NbN films deposited on Al_2O_3 r-cut, those on the c-cut type showed a wider range of T_C variation with d and a tendency toward the narrowing of ΔT_C (Table 3.1). An increase in d denotes an improvement in the film's quality, in agreement with findings reported by other groups [93, 94].

While the general trend of T_C as a function of d was reported in the literature by several groups [95, 96], T_C values also depend on the crystal structure [97], deposition technique,

Table 3.1: NbN films' properties. Starting from the left, columns are: film acronym (SC: Al_2O_3 c-cut; SR: Al_2O_3 r-cut; MO: MgO; SO: SiO_2; the number following the two letters refers to the film thickness in nm units); resistivity value at 15 K; superconducting transition temperature; superconducting transition width; superconducting critical-current density at 0 K.

Sample	ρ_{15K} **(Ω cm)**	T_C **(K)**	ΔT_C **(K)**	J_{C0} **(MA/cm²)**
MO5a *	8.0×10^{-5}	10.072	0.08	0.40 ± 0.014
MO5b **	5.8×10^{-5}	11.02	0.79	2.24 ± 0.013
MO10	1.2×10^{-4}	13.29	0.27	9.98 ± 0.15
MO15	2.4×10^{-4}	13.83	0.23	11.40 ± 0.016
SC5	8.0×10^{-5}	10.64	0.43	0.90 ± 0.010
SC10	2.4×10^{-4}	13.50	0.40	10 ± 0.028
SC15	1.7×10^{-4}	12.73	0.24	5.29 ± 0.08
SR5 **	1.1×10^{-4}	11.76	0.68	0.63 ± 0.013
SR10	1.7×10^{-4}	12.43	0.30	8.3 ± 0.18
SR15	2.3×10^{-4}	12.58	0.38	6.14 ± 0.13
SO5	9.3×10^{-7}	9.40	0.46	0.89 ± 0.024

* Both MO5a and MO5b belongs to the same deposition run, but the fabrication process of their Hall bar was carried out by using slightly different parameters. ** The Hall bar width of this film was 10 μm.

the partial pressure of nitrogen used during the film fabrication process, etc., making a direct comparison of results measured by different groups difficult [95, 96, 98, 99].

Considering the NbN films deposited on Al_2O_3 r-cut substrates, the value of T_C, while appearing scattered at $d \leq 10$ nm, follows a trend similar to that found by Soldatenkova et al. on the same substrate type (see inset Figure 3.4) [74]. The scattering of T_C in NbN films reflects inhomogeneity issues that are characteristic of this superconducting system [65].

The critical current density (J_C), a fundamental parameter in understanding the superconducting properties of a system, is defined as the maximum current density that a super-

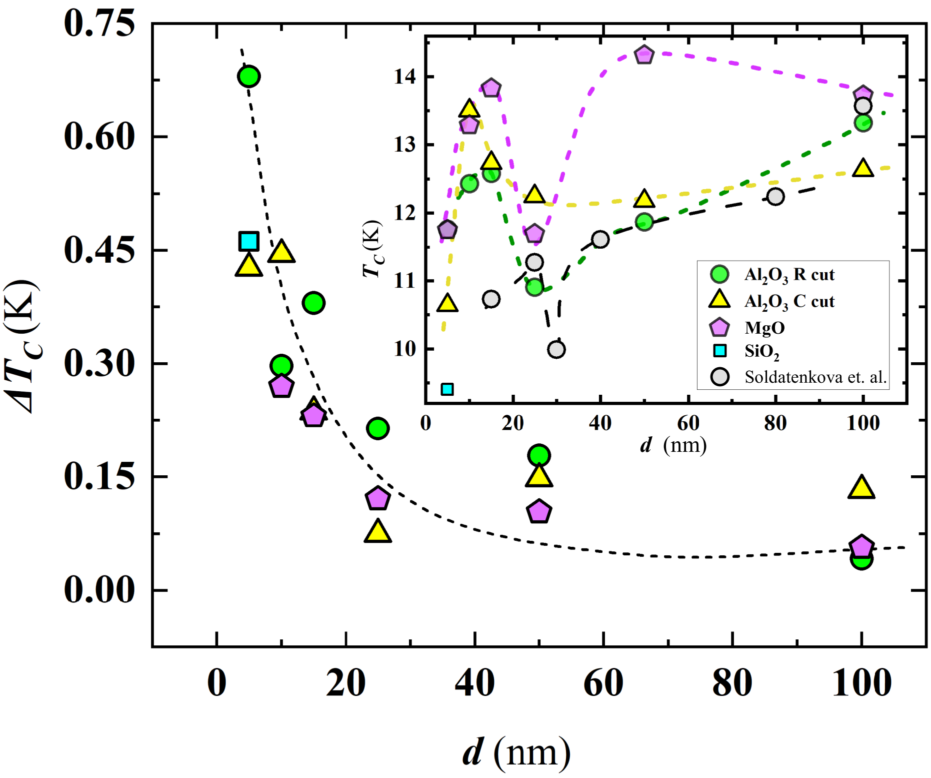

Figure 3.4: Left: Thickness dependence of the superconducting transition width of NbN films deposited on MgO (MO), SiO_2 (SO) and Al_2O_3 substrates, both c-cut (SC) and r-cut (SR) type. Right: Thickness dependence of the superconducting transition temperature of NbN films deposited on MgO (MO), SiO_2 (SO), and Al_2O_3 substrates, both c-cut (SC) and r-cut (SR) types. For comparison, T_C data of films deposited on Al_2O_3 r-cut substrates by Soldatenkova et.al [74] were plotted.

conducting material can sustain before undergoing a transition from the superconducting state to the normal state. The temperature dependence of $J_C(T)$, shown in Figure 3.5, has been derived from the measured $I - V(T)$ characteristic curves.

3.2.2 Exploring I-V Characteristics and Critical Current Density

The temperature-dependent I-V curves were measured using a pulse mode technique (explained in the materials and methods section). Short current pulses with intensities ranging from 1 μA to 1 mA, were sourced to the films at different temperatures. Measurements were conducted from about 4 K up to the T_C and recorded at intervals of 0.1-0.2 K. Figure 3.5 shows the I-V characteristics at temperatures near the transition, exhibiting clear hysteretic behavior with a well-defined crossover from the superconducting to the normal state.

This behavior was observed consistently for all film thicknesses above 10 nm. However, as the thickness decreased ($d \leq 10$ nm), several NbN films showed a sudden non-linearity in the I-V curves near T_C. This particular feature observed in ultra-thin films is investigated in more detail in Section II of this chapter. Figure 3.5 displays the temperature dependence of the superconducting critical current density, $J_C(T)$, for the set deposited on Al_2O_3 r-cut substrate at lower thicknesses of 5 to 15 nm. The J_C is extracted from the critical current values at each temperature, and the J_C values at 0 K (i.e., J_{C0}) were obtained by a least-squares fit of J_C vs T data using the standard Ginzburg-Landau equation [84]:

$$J_C(T) = J_{C0}\left[1 - \left(\frac{T}{T_C}\right)^2\right]^{\frac{3}{2}}\left[1 + \left(\frac{T}{T_C}\right)^2\right]^{\frac{1}{2}} \tag{3.30}$$

The thickness dependence of J_{C0} appears to be related to the substrate types, exhibiting a bell-shaped behavior for all the substrates. The 50 nm film shows the lowest current density of 1.29×10^9 A/m^2 on MgO substrate and values varying from 0.4 to 0.7×10^9 A/m^2 on Al_2O_3 substrates. Notably, a peak in J_{C0} at $d = 15$ nm, up to more than one order of magnitude, is observed. This anomaly at 15 nm thickness aligns well with our resistivity data, confirming a sudden change in the SC properties. The highest J_{C0} value is obtained for the film deposited on MgO substrate at 15 nm, with small differences in J_{C0} starting to appear from $d = 10$ nm. Further reducing the thickness to 5 nm, the J_{C0} drops to a value four times less than that at 10 nm. The J_{C0} values found in our films are similar to those found in thin films of NbN [100], and the bell-shaped behavior was also detected

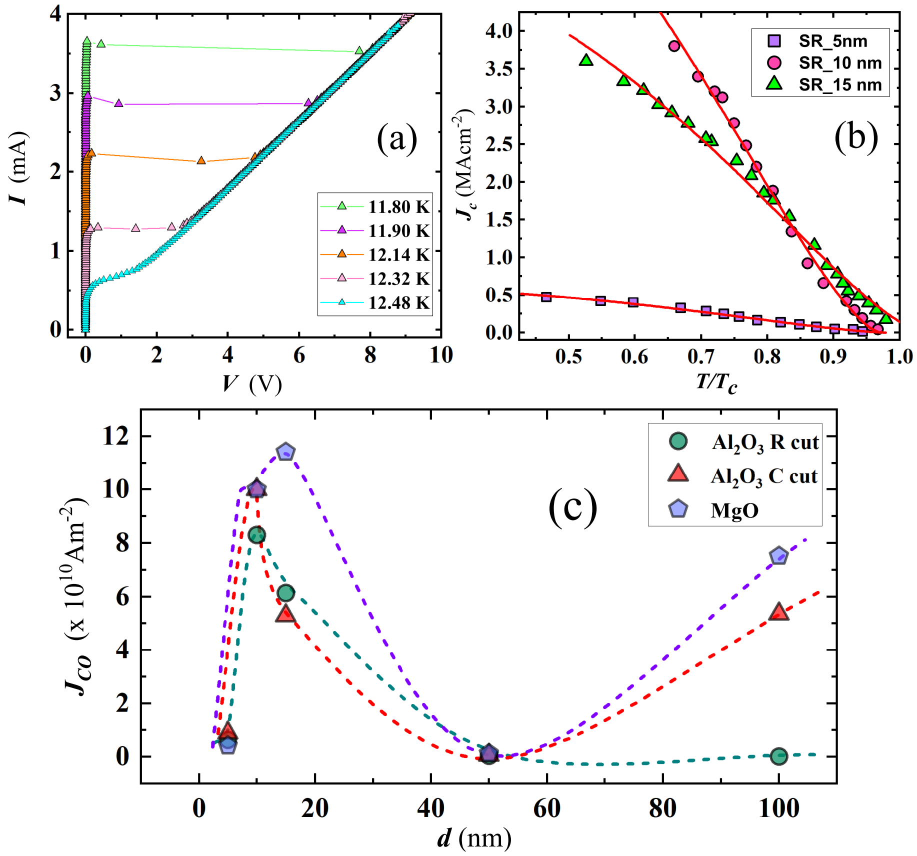

Figure 3.5: **(a)**: Current-Voltage characteristics of the superconducting film SC15, measured at fixed temperature values near the superconducting transition temperature. The hysteresis between the current sweep-up and sweep-down directions decreases as T approaches T_C. The I_C is determined from the I-V curve as detailed in the Material and Methods chapter **(b)**: Current density as a function of the temperature, normalized to T_C, for the whole set of NbN films deposited on Al_2O_3 r-cut substrate. Lines are the result of the least-squares fitting by the Ginzburg-Landau equation (see ref. [84]). **(c)**: Thickness dependence of the critical current density at zero temperature, J_{C0}, for NbN films deposited on Al_2O_3 r-cut, Al_2O_3 c-cut, MgO substrates.

in Nb [84]. The substrate's influence on the critical current density (J_C) indicates that the MgO substrate yields the highest J_C values, establishing it as the optimal substrate for fabricating NbN film-based devices.

3.2.3 Discussion

Our systematic investigation across multiple substrates has demonstrated that the choice of substrate significantly impacts the superconducting properties of NbN films. Through comprehensive characterization of critical parameters, MgO substrates consistently demonstrated superior performance, as evidenced by:

- MgO substrates yielded the highest critical temperature (T_C) values among all tested substrates.
- NbN films on MgO exhibited the narrowest superconducting transition width (ΔT_C), indicating enhanced film quality and homogeneity.
- The critical current density at zero field (J_{C0}) reached its peak value for films deposited on MgO, particularly at the 15 nm thickness.
- MgO demonstrated the least lattice mismatch with NbN, resulting in the most favorable superconducting parameters without dissipation effects.

These findings collectively establish MgO as the optimal substrate for fabricating high-performance NbN film-based devices. The superior performance can be attributed to its crystallographic compatibility with NbN, which promotes better film growth, reduces defects, and enhances overall superconducting properties.

Our systematic transport measurements reveal distinct modifications in the superconducting behavior of NbN films as their thickness decreases below 15 nm. The evidence for this transition is manifested in several experimental observations: (1) a broadening of the resistive transition near T_C, with ΔT_C increasing significantly for films below 15 nm of thickness, (2) an abrupt increase in the normal-state resistivity at thickness lower than 15 nm, showing values 3-4 times higher compared to bulk NbN systems, (3) a non-monotonic dependence of T_C on film thickness, with a notable anomaly at 15 nm, and (4) distinctive non-linear features in the I-V characteristics that deviate from the behavior seen in thicker films. Particularly striking is the observation of a peak in J_{C0} at 15 nm, followed by a sharp decline for thinner films, suggesting a fundamental change in the superconducting properties at this critical thickness. These experimental signatures, combined with the thickness-dependent evolution of transport properties, point to a possible dimensional crossover in ultra-thin NbN films. A detailed theoretical analysis of the dimensionality-driven modifications in ultra-thin NbN films will be addressed in subsequent sections.

3.2.4 Experimental Investigation of the BKT Transition

The thin NbN films below 15 nm exhibit non-linear I-V characteristics and broadened superconducting transitions, suggesting a transition to two-dimensional superconductivity. This dimensional transition manifests through the Berezinskii-Kosterlitz-Thouless mechanism, where vortex-antivortex pairs create a distinct topological phase transition as film thickness approaches the superconducting coherence length (ξ).

To observe this BKT transition, films must satisfy key criteria: thickness comparable to ξ and high surface homogeneity to minimize dissipation effects, while maintaining pearl length (Λ) greater than film width (w). Our experimental protocol addresses these requirements through carefully controlled measurements - using low currents (1 μA and 100 nA) for resistivity studies and an alternating pulse mode technique (max 1 mA) for I-V characteristics, effectively minimizing heating artifacts that could mask BKT signatures.

Analysis of our NbN films ($5 \leq d \leq 15$ nm) [71] revealed key parameters relevant to the BKT transition. The mean free path varies from 1.4 nm for 10 nm films to 7.8 nm for 100 nm films, placing our system in the dirty limit regime where the mean free path (l) is significantly smaller than the coherence length (ξ). The pearl length (Λ) measurements yielded values of approximately 100 μm, 40 μm, and 20 μm for 5 nm, 10 nm, and 15 nm films respectively. When compared with our Hall bar width ($w = 50$ μm), these values indicate that only the 5 nm film fully satisfies the dimensional criteria for BKT effects, while the 10 nm film lies at the boundary of this regime, and the 15 nm film exceeds the range where 2D fluctuations would dominate.

The BKT transition in real systems is experimentally investigated through the universal jump in superfluid stiffness (J_S) at T_{BKT}, occurring below the mean-field transition temperature (T_{MF}). This phenomenon emerges from vortex-antivortex pair (VAP) unbinding via logarithmic interactions, detectable through transport measurements. When current is applied to the superconducting film, VAP unbinding generates free vortices, manifesting as nonlinear I-V characteristics near T_{BKT}. This is marked by a distinct transition in the power exponent from $\alpha = 1$ to $\alpha = 3$, signifying the VAP unbinding process. On the other hand, two-coil mutual inductance measurements offer a direct probe for observing the BKT transition. This technique, which involves inductively coupling a drive coil and a pickup coil through the superconducting sample, enables the determination of λ^{-2}, where λ is the penetration depth. As discussed earlier, λ is directly related to the superfluid stiffness, J_S by the relation:

$$J_S = \frac{\hbar^2 n_S^2 D}{4m} = \frac{\hbar^2 c^2 d}{16\pi e^2 \lambda^2} \tag{3.31}$$

To quantify the energy scale associated with superfluid stiffness, we will express J_S in units of Kelvin. Given that the penetration depth is measured in μm, the resulting expression is:

$$J_S = 0.62 \times \frac{d[\text{Å}]}{\lambda^2[\mu m^2]}[K] \tag{3.32}$$

where d represents the thickness of the superconducting film in nanometers, and λ is the penetration depth.

Carefully measuring the temperature dependence of the inverse penetration depth, and determining the jump in the superfluid stiffness at T_{BKT} can provide direct evidence of the presence of BKT effect.

Evidence from the Transport Measurements

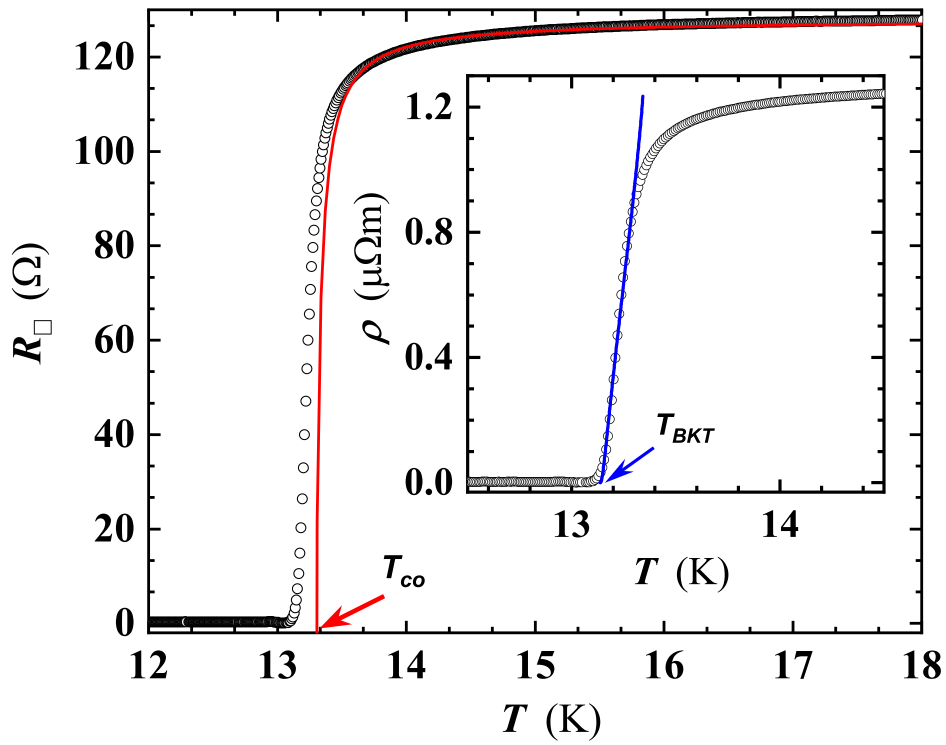

Figure 3.6: Temperature-dependent sheet resistance around the superconducting transition temperature for MO10 (see Table 3.2). The red line is the least-squares fit by using Equation (3.33). The value of T_{C0} = 13.31 K (red arrow) is the intercept of the red line with the x-axis. Inset: least-squares fitting of the $\rho(T)$ curve of MO10 by Equation (3.34). The intercept with the x-axis gives the value of T_{BKT} (13.06 K, blue arrow).

Transport measurements of ultra-thin NbN films (d < 15 nm) revealed significant deviations from bulk superconducting behavior. While bulk NbN exhibits a sharp superconducting transition, films with thicknesses below 15 nm showed distinct modifications in their transport properties. The sheet resistance, $R_\square(T)$, exhibited a gradual decrease with temperature, with the transition broadening becoming particularly pronounced in films with $d \leq 10$ nm, as demonstrated in Figure 3.6. This thickness-dependent evolution of the resistive transition suggests a fundamental modification of the superconducting properties in the ultra-thin regime.

To understand these modifications, we employed the Cooper-pair fluctuation model, which will be discussed in detail in the subsequent section. The model, developed by Aslamazov and Larkin (AL) [101] and Maki and Thompson (MT) [102, 103], was applied to analyze our $R(T)$ data by employing the equation 3.33. This approach enabled us to extract crucial parameters such as the critical temperature under zero magnetic field (T_{C0}) and the normal state sheet resistance ($R_{\square N}$). The analysis revealed that our ultra-thin films exhibit a rounded transition rather than the sharp transition characteristic of bulk samples, consistent with the emergence of thermal fluctuations near the critical temperature. In the normal state region above the transition, the sheet resistance $R_{\square}(T)$ demonstrates only a weak temperature dependence, aligning with theoretical predictions for 2D systems.

Significantly, the pair-fluctuation model used in our analysis fails when applied to 3D and 1D systems, providing additional confirmation of the two-dimensional nature of our measured superconducting system. This dimensional confirmation is further supported by the model's accurate description of our experimental data. To quantitatively characterize this behavior, we evaluated key parameters by performing least-squares fitting of the experimental $R_{\square}(T)$ curves shown in Figure 3.6. The fitting was conducted over a temperature range extending from T_{C0} to approximately 15 K, employing the relation described by [76] and [98]:

$$R_{\square}(T) = \frac{R_{\square N}}{1 + R_{\square N}\frac{\gamma}{16}\frac{e^2}{\hbar}(\frac{T_{C0}}{T - T_{C0}})} \tag{3.33}$$

where: γ is a numerical factor, $\hbar$ is the reduced Planck constant, e is the electron charge. Fitting was carried out satisfying the condition $ln(T/T_{C0}) \ll 1$.

The analysis revealed excellent agreement between fitted and experimental $R_{\square N}$ values

Table 3.2: Berezinskii–Kosterlitz–Thouless (BKT) parameters derived by the analysis of the resistivity and I-V characteristics curves of some of the thinner NbN films. Column headings, from left: sample acronym *; BKT temperature derived by $\rho(T)$ fitting with Equation (3.34); SC transition temperature at $B = 0$ (see the text); normal state sheet resistance at 20 K; γ value (see the text and Equation (3.33)); VAP polarizability.

Sample	T_{BKT} **(K)**	T_{C0} **(K) ****	$R_{\square N}$ **(Ω)**	γ	ϵ
MO5a	9.70 ± 0.03	9.90	502.30 ± 0.01	0.970 ± 0.002	10.28 ± 0.030
MO5b	10.30 ± 0.02	10.60	620 ± 1.06	1.500 ± 0.005	11.49 ± 0.022
MO10	13.060 ± 0.008	13.31	129.8 ± 0.60	1.56 ± 0.09	25.5 ± 0.11

* For meaning of sample acronym see the caption of Table 3.1.

within 2–3%. Both T_{C0} and γ showed systematic dependence on film thickness d and substrate type, particularly evident in the T_{C0} values for 5 nm NbN films. The T_{C0} values obtained from the fit were consistently, though systematically, lower than those extracted from the analysis of the superconducting transition branch of the $\rho(T)$ curves (see Table 3.2). The values of γ, ranging from ≈ 1 to ≈ 2 (Table 3.2), align well with those reported for NbN films with $d < 10$ nm [76, 98], and are comparable with literature values for various superconducting materials.

The result of the $R_{\square}(T)$ fitting of film MO10 is reproduced in Figure 3.6. Similar findings were found also for MO5a, MO5b and SC10.

To further investigate the possibility of a Berezinskii-Kosterlitz-Thouless transition in our thin films, we analyzed the resistivity data using the Halperin-Nelson relation (Equation 3.34). This theoretical framework quantitatively describes the resistance behavior characteristic of two-dimensional superconductors near the BKT transition. Below T_{BKT}, vortex-antivortex pairs remain bound, ensuring the dissipationless flow of supercurrent. However, as T approaches T_{BKT}, thermal fluctuations become sufficiently strong to dissociate these pairs, leading to the emergence of free vortices, as elucidated in the theoretical section. In this intermediate regime ($T_{BKT} < T < T_{C0}$), where T_{C0} represents the superconducting transition temperature in zero magnetic fields, a dynamic equilibrium exists between bound and unbound vortices [64, 76, 104]. The presence of these free vortices profoundly influences the film's resistive properties. Under an externally sourced current, unbound vortices experience a Lorentz force, giving rise to a finite voltage drop across the film.

Consequently, the film's resistivity is well-described by the Halperin-Nelson relation:

$$\rho(T) = aexp\left(-2\sqrt{b\frac{T_{C0} - T}{T - T_{BKT}}}\right) \tag{3.34}$$

where a and b are fitting parameters related to the SC material, and the values obtained were less than 1 for all films. T_{BKT} represents the temperature at which vortex-antivortex pairs unbind. This exponential temperature dependence is a distinctive signature of the BKT transition, fundamentally different from the power-law behavior expected in conventional superconducting transitions. By applying this analysis to our thinnest NbN films, which are most likely to exhibit 2D behavior, we were able to extract their respective T_{BKT} values. The inset of Figure 3.6 demonstrates this analysis for the MO10 sample, where the intersection with the temperature axis yields $T_{BKT} = 13.06$ K.

It is also interesting to estimate the polarizability, ϵ_{BKT}, of a VAP at the BKT-like vortex phase transition in the presence of other VAPs, by using the relation [76]:

$$\frac{T_{BKT}}{T_{C0}} = \frac{1}{1 + 0.173\epsilon_{BKT}R_{\square N}\frac{2e^2}{\pi h}} \tag{3.35}$$

equation (3.35) which was applied to NbN films deposited on different substrates, resulting in values of ϵ (Table 3.2) in close agreement with those found in ref. [76] for 6 nm thick NbN films and also successfully cross-checked with the universal relation $k_B T_{BKT} = AT_{BKT}/4\epsilon_{BKT}$ for topological 2D phase transitions; see Nelson and Koster-

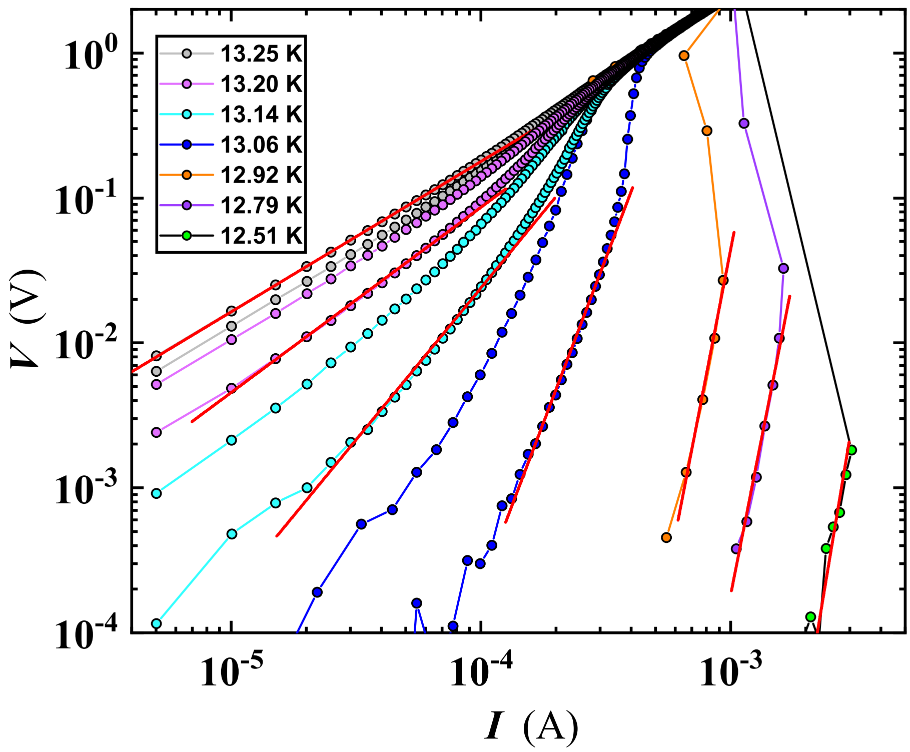

Figure 3.7: Voltage-current characteristics for the film MO10. Experimental data of the sweep-up curve were fitted by a power law function to extract the value of α (see Equations 3.36, 3.37 and Table 3.2.

litz [105, 106]. All the parameters extracted by fitting (see Table 3.2) are in excellent agreement with the values reported in the ref. [76, 98].

Further evidence supporting the BKT transition was obtained from our analysis of the I-V characteristics. As detailed in the theoretical background of this chapter, the correlation between the observed jump in the critical exponent α, extracted from the I-V characteristics using the following equations provides compelling support for this interpretation:

$$V \propto I^{\alpha}(T) \tag{3.36}$$

$$\alpha(T) = 1 + \pi \frac{J_s(T)}{T} \tag{3.37}$$

At the BKT transition, the I-V exponent exhibits a characteristic universal jump from

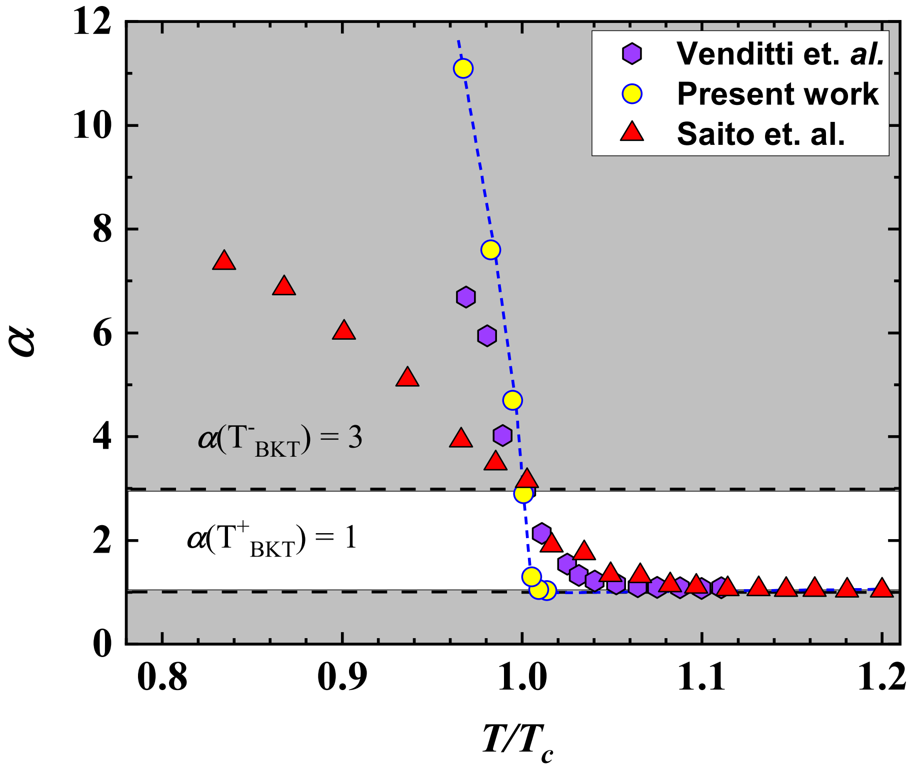

Figure 3.8: Temperature dependence of α for MO10, derived from the power-law fitting of the V-I curves plotted in Figure 3.7. A jump in the value of α from ≃1 to ≃3 (white region) was detected at T_{BKT}, corresponding to $T/T_C = 0.989$. For comparison, the α values for a 3 nm thick NbN film from the work of Venditti et al. [65] and for MoS_2 from the work of Saito et al. [107] were added to the data. The broken line is a guide for the eyes. The temperature was normalized to T_{BKT} for our and Saito et al. data. Venditti et al.'s α values were derived by the digitization of Figure (2e) in ref. [65].

$\alpha(T^{-}_{BKT}) = 3$ to $\alpha(T^{+}_{BKT}) = 1$, where the unity value signals the metallic ohmic behavior in the normal state of the I-V characteristics. This discontinuous jump in the exponent represents a fundamental signature of the BKT transition, reflecting the sudden unbinding of vortex-antivortex pairs.

Using Equation (3.36), we performed a detailed least-squares fitting of the voltage-current curves for the MO10 film, measuring at several temperature points (Figure 3.7). Our analysis revealed the predicted universal jump from ≃1 to ≃3 at T_{BKT} (Figure 3.8). The transition we observed demonstrates a particularly sharp and well-defined character (see Figure 3.8), showing excellent agreement with the results reported by Venditti et al. for NbN thin films [65]. Remarkably, this characteristic behavior is not unique to NbN systems; similar transitions have been observed by Saito et al. in MoS_2 [107] (Figure 3.8), a materially distinct system. This universality across different material systems provides compelling evidence for the fundamental nature of the BKT transition and validates the use of the universal jump in superfluid density as a robust criterion for identifying the BKT transition temperature.

3.3 Key Findings and Final Thoughts

We have delved into the theoretical frameworks and interesting experimental results that underscore the emergence of the BKT phenomenon in ultra-thin NbN films ($d < 15$ nm). A convergence of the Halperin-Nelson model, a good agreement between the observed vortex-antivortex pair polarizability values and the Nelson-Kosterlitz universal relation, and a sharp, textbook-like transition of the α exponent in the vicinity of T_{BKT}, collectively provides a clear confirmation of the BKT transition in our investigated NbN films. This jump in α is often obscured by broadening effects, resulting in a gradual variation of α, that can hinder the unambiguous identification of the BKT transition. The successful extraction of α values and the observation of a striking jump at the precise T_{BKT} is a good observation, as, such clear indications of the BKT transition are rarely observed experimentally. The clarity and precision of our findings not only validate the theoretical predictions but also provide a roadmap for researchers seeking to uncover similar clear signatures of the BKT transition in related materials.

We will further extend our experimental study to understand the BKT physics under an applied perpendicular magnetic field. This novel work will shed light on the previously unexplored interplay between the BKT transition and magnetic field effects, paving the way for the development of a comprehensive theoretical framework.

Chapter 4

Exploring BKT physics under low magnetic field

4.1 Introduction

The preceding chapter presented a comprehensive analysis of the Berezinskii-Kosterlitz-Thouless transition in two-dimensional superconducting films, encompassing both the theoretical framework and our experimental observations. The investigation uncovered characteristic signatures of this fascinating phenomenon, which were particularly evident in the resistivity behavior and current-voltage characteristics of the studied systems. The results not only confirmed the presence of BKT physics in our samples but also laid the groundwork for more nuanced investigations presented in this chapter.

While extensive research has displayed many aspects of the BKT transition [59–64] and related phenomena, the complex interplay of quantum coherence, quasi-particle interactions, and topological effects continue to present intriguing challenges. Despite substantial progress in understanding these systems, several fundamental questions persist, particularly regarding the behavior of the BKT state under various external conditions, such as magnetic fields [59, 108–110].

To date, investigations of the BKT effect in SC ultra-thin films have primarily focused on zero-field conditions. However, the interpretation of this phenomenon becomes significantly more complex in the presence of applied magnetic fields where $H \geq H_{C1}$, where H_{C1} is the lower critical magnetic field at which vortices began to penetrate the superconductor. The introduction of these additional vortices and pinning mechanisms complicates the identification of BKT hallmarks, presenting considerable challenges in detecting the BKT effect. This complexity underscores the need for more sophisticated experimental and analytical approaches to unravel the interplay between BKT physics and magnetic fields in ultra-thin films.

Our preliminary investigations at moderate perpendicular magnetic fields (1300 G to 3600 G) show suppression of the Berezinskii-Kosterlitz-Thouless effect, with no discernible signatures of its presence. This observation motivates a detailed examination of vortex-antivortex pair (VAP) behavior under significantly lower magnetic field intensities. Specifically, we aim to elucidate the nature of the transition in VAP interactions as a function of applied field strength. The central question we address in this section is whether the transition from BKT physics to a regime dominated by individual VAP interactions is gradual or abrupt as the magnetic field intensity is reduced.

Therefore, to investigate this, we conducted an extensive study centered on high-resistance NbN films. These films, which demonstrated clear BKT effects as detailed in chapter 3, serve as an ideal platform for examining the interplay between magnetic fields, free vortices, and the BKT state. Our objective is to provide a comprehensive understanding of the fate of the BKT superconducting state and its evolution under varying magnetic field conditions. By exploring this continuum from low to high fields, we aim to understand the transition between the VAP-dominated BKT state and the regime where free vortices play a dominant role, offering insights into the rich physics of 2D superconductors in magnetic fields.

Approach to probe the BKT physics under magnetic field:

Our investigation into the BKT phenomenon under varying field conditions employs a multi-faceted experimental approach:

Resistivity Measurements: We conducted detailed measurements of resistivity, $\rho(T)$ near the T_C, applying low current values ($\approx$ few μA) under perpendicular field intensities, varying systematically across two regimes: a low-field range (0-150 G) and a high-field range (1300-3600 G).

Analysis of system dimensionality: To establish the two-dimensional nature of our system near T_C in the presence of H, we have initially employed the Cooper pair fluctuation model.

Halperin-Nelson Theory Application: Based on the previous study (Ref. chapter 3), we utilized the Halperin-Nelson (HN) theory to analyze the gradual suppression of $\rho(T)$ as the transition is approached from above.

Fluctuation Regime Analysis: We then extended our investigation to explore the crossover behavior from 2D Aslamazov-Larkin (AL) fluctuations to Halperin-Nelson conductivity for temperatures above T_C, providing additional confirmation of the fluctuation phenomenon.

Current-Voltage Characteristics: As discussed in the previous chapter, a detailed analysis of the I-V characteristics, obtained using the pulsed current technique, provides an indirect method to probe the superfluid stiffness. To identify the signature discontinuous jump associated with the BKT transition under varying magnetic fields, we meticulously examined the power-law exponent α in the relation $V \propto I(T)^{\alpha}$. Employing the renormalization group equations, we fit the extracted superfluid stiffness to detect the abrupt jump in the superfluid density, a hallmark of the BKT transition.

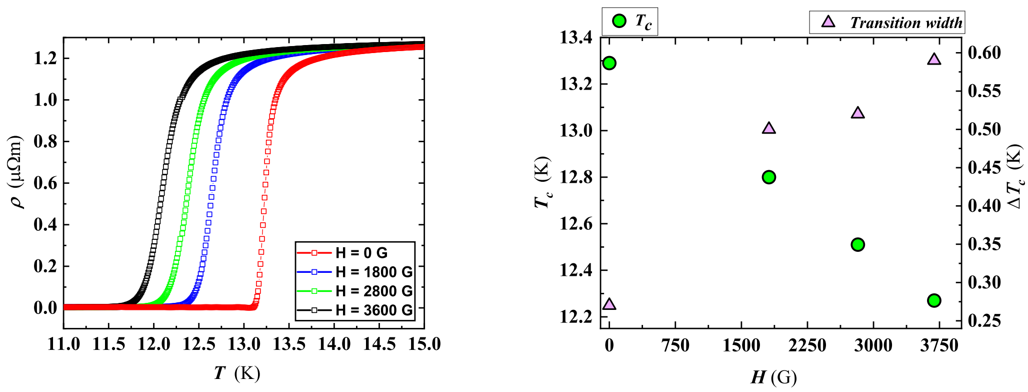

Figure 4.1: **Left**: Temperature-dependent resistivity under an applied magnetic field of varying intensity, for a 10 nm thick NbN film deposited on a MgO substrate (MO10). **Right**: Variation of the superconducting critical temperature (circles) and superconducting transition width (triangles) as a function of the magnetic field intensity for the MO10 film.

4.2 Experimental findings and analysis

Investigation of the BKT Effect under High Magnetic Fields

To investigate the behavior of the BKT transition in the presence of a perpendicular magnetic field generated by permanent magnets assembly (see the Material and Methods chapter), we performed temperature-dependent resistivity measurements, $\rho(T)$, on ultra-thin NbN films. A standard four-wire configuration was employed with a pulsed current of 1 μA to minimize Joule heating effects. Measurements were conducted under applied magnetic field intensities ranging from 1300 G to 3600 G.

Figure 4.1 illustrates the resistivity behavior measured at high magnetic field intensities, in which a substantial shift in the T_C has been observed as the field intensity increases. This shift is shown by a distinct jump in the resistivity curve, accompanied by a pronounced broadening effect evidenced by the rounding of the curve near the transition. This broadening effect arises due to the well-established pair-breaking effect [85] that occurs when a perpendicular magnetic field is applied to the superconductor.

For instance, in Ref. [111], for a 5 nm thick NbN film on a Al_2O_3 substrate, the ΔT_C

increases from 1.5 K to 3 K when the field intensity varies from 0 to 7 T, which suggests a presence of high level of inhomogeneity in the sample. Conversely, for a 50 nm thick NbN film on the same substrate, the value of ΔT_C increases from 0.15 K to 0.5 K under the same conditions. Furthermore, it has been found that the transition width shows a more significant change in thinner films, attributable to additional broadening caused by enhanced granularity and inhomogeneity, along with a progressive increase in the resistive tail [112].

To investigate the BKT effect, we employed the Cooper pair fluctuation model, as discussed in detail in Chapter 3 [63]. Through this fitting analysis, our objective is to extract the T_C, which is the mean-field critical temperature under a magnetic field, and $R_{\square N}$ from the experimental data, similar to our previous approach.

To facilitate the analysis, I will provide a brief reintroduction of the equations that will be utilized for examining the BKT effect.

$$R_{\square}(T) = \frac{R_{\square N}}{1 + R_{\square N}\frac{\gamma}{16}\frac{e^2}{\hbar}(\frac{T_{C0}}{T - T_{C0}})} \tag{4.1}$$

where γ is a numerical factor, $\hbar$ is the reduced Planck constant, e is the electron charge, and T_{C0} is the critical temperature in zero magnetic fields and is replaced by T_C when considering equation under the applied magnetic field.

$$\rho(T) = aexp\left(-2\sqrt{b\frac{T_{C0} - T}{T - T_{BKT}}}\right) \tag{4.2}$$

The experimental data, obtained under a perpendicular magnetic field intensity of 1800 G, is presented in the form of sheet resistance, $R_{\square}(T)$ with varying temperature (see Fig. 4.2). The experimental points exhibit a distinct deviation from the predicted behavior of the pair-fluctuation model. Notably, this deviation becomes evident near the transition

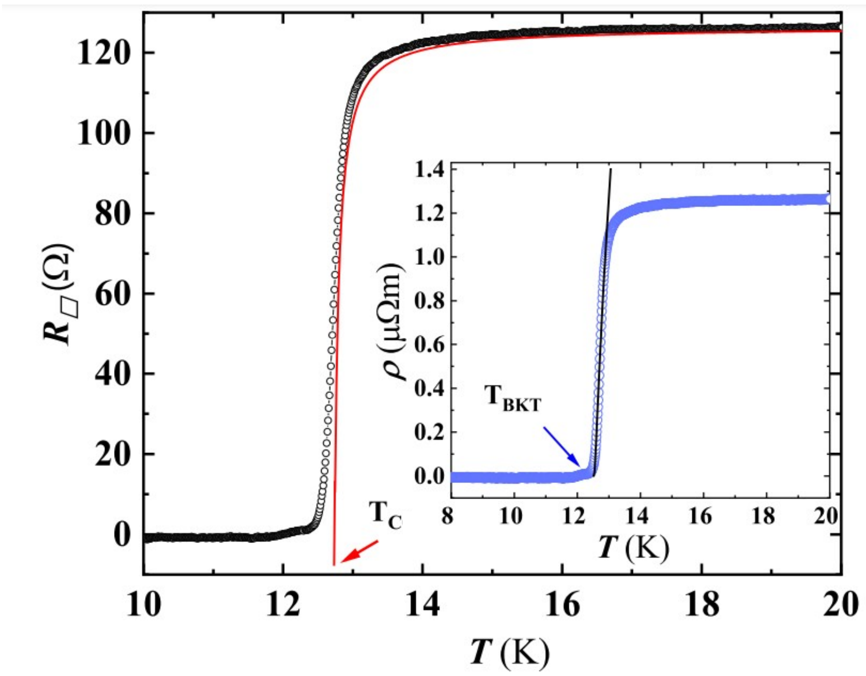

Figure 4.2: Temperature dependence of sheet resistance (main panel) and resistivity (inset) for a 10 nm thick NbN film on MgO substrate under a magnetic field of 1800 G. The red and black lines are the least squares that fit with the eq. 4.1 and 4.2 to the sheet resistance and resistivity data respectively.

point and persists up to a temperature of 14 K, indicating a discrepancy. Based on the available literature, this observation presents two plausible explanations: Firstly, it suggests that our NbN films undergo a dimensional crossover near the critical temperature due to the strong influence of the perpendicular magnetic field, resulting in the observed divergence. Secondly, the model used in our analysis may fail to account for the effects induced by the applied field intensity. These effects include the emergence of vortices due to magnetic field which are not considered in the model.

On the other hand, in the subsequent analysis, the temperature-dependent resistivity curve exhibits a pronounced tail-like effect that disrupts the sharp transition from the superconducting to the normal state, as shown in the inset of Figure 4.2. The fitting of the

Halperin-Nelson equation (Eq. 4.2) to the data yields poor convergence, resulting in a significant error of ± 2.28 K in the determination of T_C obtained from the least squares fit. It is noteworthy that this fitting procedure introduces an error of approximately 16.3%, which exceeds an acceptable range for accurate analysis. Moreover, as the magnetic field intensity is further increased, this deviation becomes more prominent, indicating no signs of the BKT effect.

4.2.1 Variation of the α Exponent under High Magnetic Fields

Building upon the analysis of the resistivity data, it is intriguing to investigate the impact of the magnetic field on the V-I characteristics. To explore this, we performed measurements of the V-I characteristics at different field intensities, ensuring a constant interval of 0.1 K between each measurement. Extreme care has been taken while performing the V-I measurements, to reduce any artifacts related to heating, which can complicate the data analysis. we utilized the power-law function ($V \propto I^{\alpha}$) to fit the low current region, as explained in detail in Chapter 3.

The resulting α exponent from the linear fit is plotted in figure 4.3, as a function of the magnetic field intensities.

The BKT transition can be observed through the temperature dependence of $\alpha(T)$ [65]. In the absence of applied field, at $T/T_C \approx 1$, α undergoes a steep decline from 3 to 1, which is the hallmark of the BKT effect (see Chapter 3). However, as the H is increased, no abrupt jump in α is observed (Ref fig. 4.3), and the curves nearly overlap. Notably, plotting $\alpha(T)$ instead of T/T_C shows a shift of the curves towards lower temperatures proportional to the field intensity, while the slope of the curves remains relatively unchanged (Fig. 4.3).

The disappearance of the BKT phenomenon at high magnetic fields, while theoretically

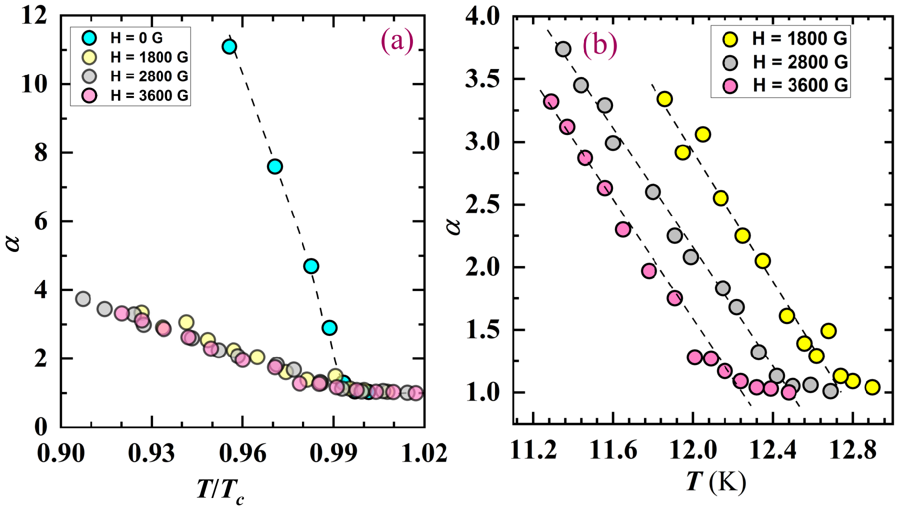

Figure 4.3: **Left**: $\alpha(T)$ values for MO10 are shown with the temperature dependence normalized to T_C at a magnetic field intensities of 1800 G, 2800 G and 3600 G. The zero field values are taken from the chapter3, for the comparison. **Right**: The α exponent as a function of temperature is shown, exhibiting a notable decrease in the slope at each field intensity.

expected and recognized in the scientific community, reveals a critical gap in our understanding: the behavior of this system at extremely low magnetic field intensities. This unexplored region, particularly in the range as low as 3 G, presents an opportunity to uncover new physics and validate existing theoretical frameworks.

To address this knowledge gap, we conducted a comprehensive experimental investigation focusing on very low magnetic fields ranging from 3 G to 150 G. This systematic study aims to thoroughly explore the BKT physics within this regime, revealing potential gradual trends and providing deeper insights into the system's behavior under these distinct field conditions.

4.2.2 Suppression in the superconducting parameters under low magnetic fields

We begin with a comprehensive investigation of the transport measurements conducted in the vicinity of T_C for different superconducting systems. To facilitate comparative analysis, we have also included experimental data from two distinct systems: a 100 nm thick NbN film on MgO substrate (MO100) and a quasi-one-dimensional 5 nm thick NbN system on Al_2O_3 substrate (SR5). The temperature-dependent resistivity measurements were conducted, starting from the case of zero magnetic fields, followed by a gradual increase in the field intensity. Notably, the lowest field measurements were performed at 3 G. It is crucial to highlight here that all measurements were carried out under zero field-cooled conditions, ensuring the acquisition of consistent and reliable data.

As shown in figure 4.4, for sample MO10, we observed a significant downward shift in the resistivity curve, reducing the T_C in a substantial way for H as low as 3 G. This behavior continues up to $\approx$ 33 G, accompanied by an inconsistent reduction in the magnitude of the resistivity jump. However, above this threshold, the shift in T_C progressively decreases. From the extracted parameters, T_C and ΔT_C (shown in fig. 4.5), an anomalous effect is observed precisely at $H = 10$ G. This effect becomes more pronounced in films with a thickness of 5 nm, as observed across various substrate materials. Interestingly, a resonance effect in T_C has been detected in MO5 up to approximately 20 G. Thereafter, a saturation effect starts to persist up to $\approx$ 90 G, showing a further decrease in T_C as H intensity starts to increase (Fig. 4.5a). For MO100, the effect of H on T_C is significantly reduced. This is caused by the 2D-3D crossover when the thickness increases. Consistently, the trend in T_C shows a negligible shift of $\approx$ 0.15 K up to 20 G, then displaying a regular behavior as expected for a 3D superconducting system (Fig. 4.5a). On the other hand, a strong non-monotonic dependence of ΔT_C on H has been detected at 5 nm (MO5), with an initial rise up to $\approx$ 30 G, then followed by a decrease till about 70 G, finally in-

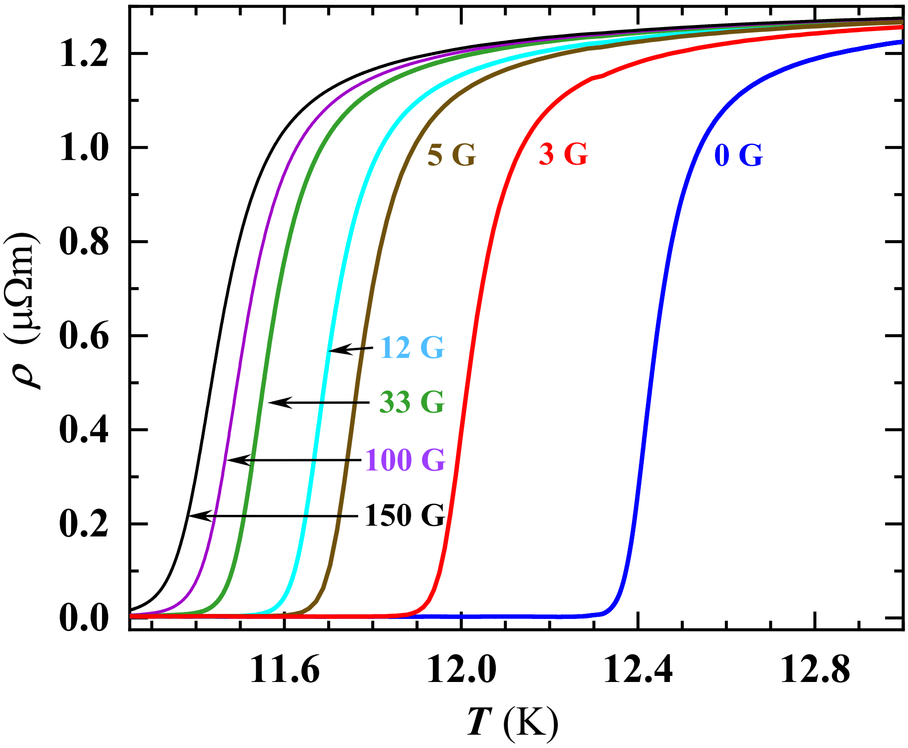

Figure 4.4: Temperature dependent resistivity around the SC transition for a 10 nm-thick NbN film (MO10) under several H field intensities applied perpendicular to the film surface.

creasing again at higher intensities (Fig. 4.5b). For thicknesses of 10 nm (MO10) and 100 nm (MO100), the variation in ΔT_C occurs up to $H \simeq 15$ G, with a very small overall variation in the thicker films (Fig. 4.5b).

These distinct differences in the superconducting behavior of NbN films with varying thicknesses at low magnetic fields are attributed to the inherent disorder present in systems where the film thickness is comparable to the superconducting coherence length ($\xi \approx 5$ nm). Consequently, a fascinating trend is observed due to the occurrence of a sizeable density of free vortices, which are introduced when the applied field intensity surpasses the critical field, H_{C1} of a superconducting system. For low-dimensional systems (such as 2-D or 1-D) characterized by inherent granularity, it is crucial to acknowledge the significance of the critical field value (H_{C1}). It represents the field intensity at which the generation of free vortices initiates within the superconducting system. Notably, for 2D or 1D systems, this value can be significantly reduced, potentially approaching zero, which allows for the introduction of free vortices, even at extremely low magnetic field strengths.

In fact, for our 10 nm-thick NbN film, the value of $H_{\mathrm{C1}} = 4\phi_0 \ln(w/\xi)/w^2 \approx 0.3\,\mathrm{G}$, where ϕ_0 is the magnetic flux quantum and $w = 50\,\mu\mathrm{m}$ is the sample width [72]. As a result, the induced vortex density $n_f = H/\phi_0$ varies from $\approx 1.45 \times 10^7\,\mathrm{cm}^{-2}$ to $\approx 7.25 \times 10^8\,\mathrm{cm}^{-2}$, for H varying from 3 G to 150 G. In this case, even the lowest applied field is ten times larger than the calculated H_{C1} for our 10 nm thick film, being thus sufficient to generate a sizeable vortex density and leading to a substantial reduction of T_{C}. These findings are also consistent with previous experimental investigations [76] and numerical analysis of the interplay between the sample width w and the coherence length ξ [113]. Moreover, a critical condition for vortex generation in superconducting strips was established as $w > 4.4, \xi(T)$, where w is the strip width and $\xi(T)$ is the temperature-dependent coherence length. This condition, extensively studied by McNaughton et al. [113], emerges from their phase diagram analysis explaining vortex generation at very low magnetic fields, particularly for systems with large width-to-coherence-length ratios (w/ξ).

Regarding the resonance in T_{C} observed in MO5 for very tiny fields, with a sizable amplification of the order of 2 K, its microscopic origin deserves further analysis, with a detailed study. We propose here that a complex interplay between disorder, coherence, and magnetic length scales can generate nonlinear effects in the vortex-antivortex interaction, leading to T_{C} amplifications. However, increasing the film thickness towards 100 nm, fluctuation effects are supposed to be reduced due to the 2D-3D dimensional crossover and no new vortices are generated as indeed observed in MO100 (Fig. 4.5b).

To gain deeper insight into the above-discussed phenomenology, we analyzed the $V-I$ characteristics under a perpendicular H field. The critical current density at zero temper-

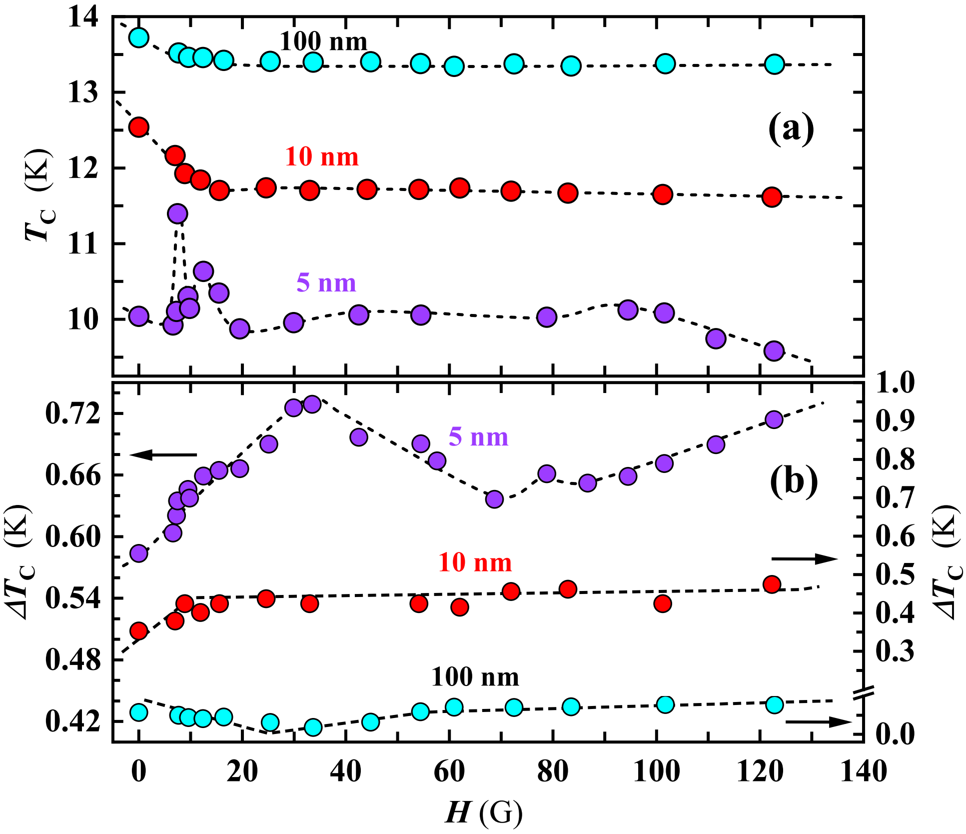

Figure 4.5: Variation of T_C (panel a) and of the SC transition width (panel b) as a function of H applied perpendicular to the film. The SC transition width has been calculated as the T difference of 90% and 10% of the normal state resistivity values just above the transition. Broken lines are guides for the eye.

ature, J_{C0}, derived from the least square fitting with the 3D and 2D GL equations [84], exhibits a similar reduction with increasing H under zero field cooled (ZFC) measurements (Fig. 4.6), suggesting that J_{C0} is not sensitive to the dimensionality of the system. However, differences emerge considering the SC critical temperature. In fact, above 10 G, T_C extracted from resistivity mimic the values derived by the 2D GL equation fit (Fig.4.6, inset), confirming the 2D nature of our NbN films.

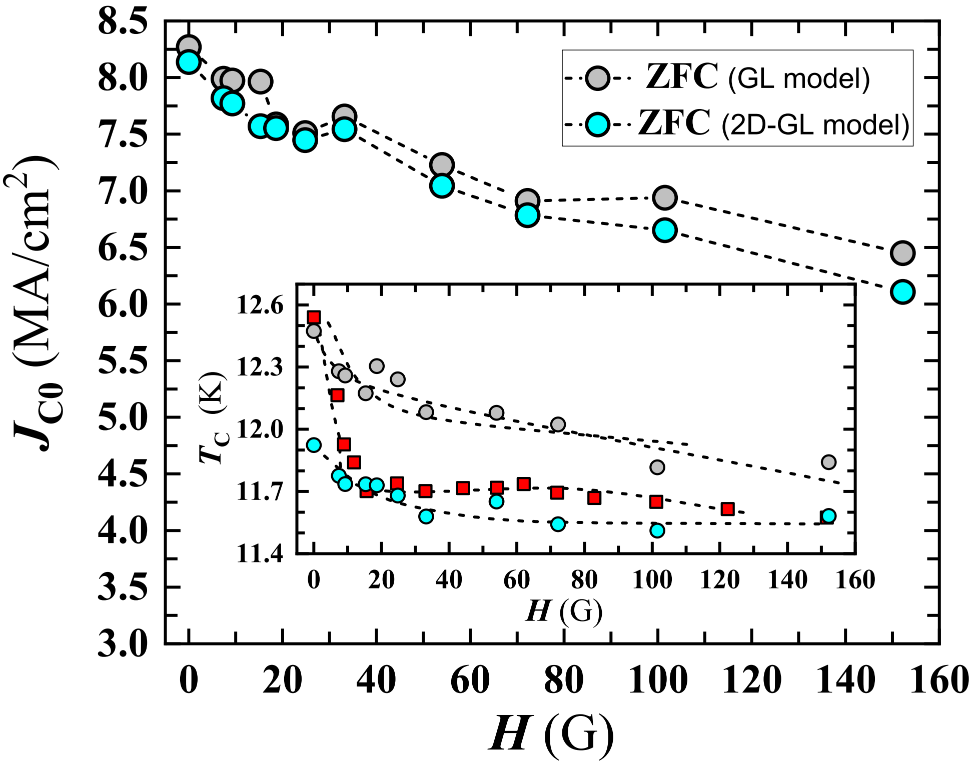

Figure 4.6: Critical current density at 0 K as a function of H for MO10, under zero field cooled conditions is shown. J_{C0} has been derived fitting $V-I$ curves by using both the 3D GL (grey-filled circles) and the 2D GL equations (cyan-filled circles). Inset: H dependence of T_C derived by the least squares fitting of $\rho(T)$ curves (red filled squares) and of $V-I$ curves by 3D (grey filled circles) and 2D (cyan filled circles) GL equations. Broken lines are guides for the eye.

The intricate response of superconducting properties in NbN films to minute magnetic fields reveals a complex interplay between dimensionality, disorder, and field intensity. Notably, the anomalous behavior at low fields and the striking resonance effect in T_C for 5 nm films underscores the essential role of disorder and dimensionality in modifying the physical parameters. Our analysis of critical current density, coupled with comparisons between 2D and 3D Ginzburg-Landau fits, provides compelling evidence for the two-dimensional nature of our thinner NbN films. Based on these findings, the subsequent section of our study is dedicated to the thorough exploration of the BKT phenomenon under the influence of low-applied magnetic fields, employing various approaches.

4.2.3 Paraconductivity

When examining systems with lower dimensionalities, we encounter increased complexities, leading to the emergence of novel effects and phenomena. Notably, the amplitude of fluctuations becomes more pronounced as the Ginzburg-Landau coherence length at zero temperature, $\xi(0)$ decreases. As a result, these fluctuations are predominantly observed in reduced dimensional systems as systematically analyzed by Silva et al. [114], where they manifest as a broadening-like feature during the transition. In contrast, fluctuations of this nature are relatively less prevalent in bulk systems.

While the term ”fluctuations” has been mentioned several times in the previous chapter, it has predominantly been used for the effects below the critical temperature dominated by the change in the order parameter. However, these fluctuation effects can survive even after the transition is achieved, arising due to the transient nature of the Cooper pairs, giving rise to a short-lived superconducting channel. These channels provide an additional pathway for electron movement, altering conductivity and giving rise to what we call paraconductivity. The study of this quantity offers an additional avenue for comprehending low-dimensional systems, achieved by investigating the dependence of $\xi(0)$ and exploring the dimensionality of the systems.

To comprehensively study paraconductivity, it is crucial to consider the contribution of distinct factors, which collectively provide an overall understanding of this phenomenon. The first factor involves a direct contribution from Cooper pairs, extensively investigated by Aslamasov and Larkin [115] and studied in different systems by varying experimental techniques such as [116, 117]. The second factor pertains to an additional effect arising from the formation of Cooper pairs through the coherent diffusion of electrons by the impurities. This effect is considered a quantum correction term, augmenting the Aslamasov-Larkin contribution, given by Maki and Thompson [118, 119]. However, it is important to note that the Maki-Thompson (MT) contribution is suppressed in systems with significant disorder, such as NbN, where it becomes negligible compared to the Aslamazov-Larkin (AL) contribution. Consequently, MT term can be neglected in this analysis, as is often done in practice.

4.2.4 Aslmasov-Larkin conductivity

The conductivity in a normal metal, without any fluctuation effect, is given by :

$$\sigma_{AL} = \frac{ne^2\tau}{m} \tag{4.3}$$

where m is the effective mass, τ is the relaxation time and n represents the electron density. By this analogy, we can estimate the conductivity due to the superconducting fluctuation:

$$\Delta\sigma_{AL}(T) \simeq \frac{(2e^2)}{m^*}\Sigma_K \frac{\langle|\psi_K|^2\rangle\tau_k}{2} \tag{4.4}$$

By calculating the integral and taking K as a continuous variable, we obtain:

$$\sigma_{AL}^{3D} = \frac{e^2}{32\hbar\xi_0 ln(T/T_C)^{1/2}} \tag{4.5}$$

$$\sigma_{AL}^{2D} = \frac{e^2}{16\hbar d ln(T/T_C)} \tag{4.6}$$

and

$$\sigma_{AL}^{1D} = \frac{\pi e^2}{16\hbar A ln(T/T_C)^{3/2}} \tag{4.7}$$

where d is the thickness and A is the wire cross-section. Near the transition $\epsilon = ln(T/T_C)$ can be taken as $\frac{T-T_C}{T_C}$ [1, 115]

It is important to note that the two-dimensional Aslamazov-Larkin equation, being independent of the material, can be directly applied to confirm the fluctuation effects. We will now use the experimental results to investigate the conductivity in the studied superconducting system.

Experimental results

In the previous section, the analysis at high magnetic fields did not yield any direct conclusion, aside from the observed diminishing effect of the BKT transition indicated by the fluctuation model and V-I characteristics. Therefore, in this section, we will delve into a detailed analysis by investigating the fluctuation conductivity. The objective is to understand the underlying mechanism occurring within the system, which leads to the breakdown of BKT physics.

To assess the occurrence of BKT under low field intensity, first, we have studied the temperature dependence of ρ(T), close to the SC transition, revealing interesting features. The fitting of the normal state resistivity at the highest field, $H = 150\,\mathrm{G}$, is given by the equation, $\rho_N(T) = A + B/T + C/T^2 + D/T^3$, over an interval $[T_1, T_2]$, with $T_C < T_1 < T_2$. This protocol of using the same normal-state resistivity at all magnetic fields reduce the number of fitting parameters, at the expense of having slightly less accurate fits at low magnetic fields. For the analysis, the temperature range considered is from $T_1 = 14$ K to $T_2 = 20$ K. The T range is taken further away from the T_C to investigate the presence of superconducting fluctuations that persist after the transition. The least squares fitted parameters are: $A = 1.65 \times 10^{-6}\,\Omega\cdot\mathrm{m}$, $B = -1.73 \times 10^{-5}\,\Omega\cdot\mathrm{m}\cdot\mathrm{K}$, $C = 3.02 \times 10^{-4}\,\Omega\cdot\mathrm{m}\cdot\mathrm{K}^2$, $D = -1.83 \times 10^{-3}\,\Omega\cdot\mathrm{m}\cdot\mathrm{K}^3$.

A necessary quantity to determine here is the temperature dependant excess conductivity due to SC fluctuations, given by:

$$\Delta\sigma = \sigma(T) - \sigma_N(T) \tag{4.8}$$

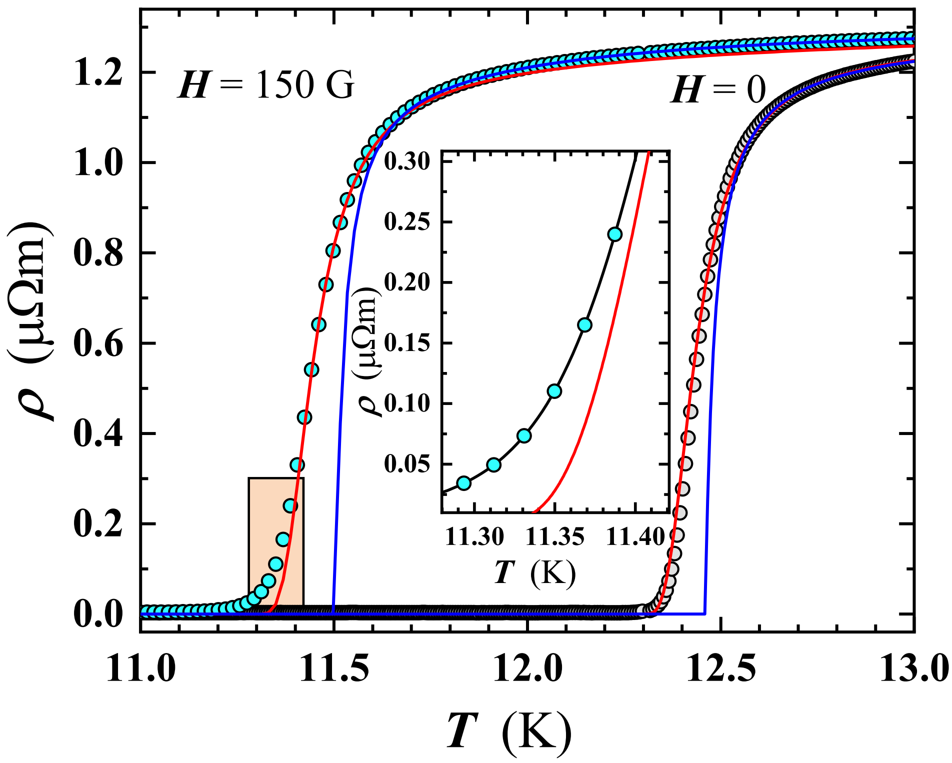

Figure 4.7: Temperature dependence of the resistivity for MO10, at $H = 0$ G and $H = 150$ G. Lines are least-square fitting by the Halperin-Nelson equation [Eq. (4.10), red] and by the Aslamazov-Larkin equation [Eq. (4.9), blue]. The smearing of the BKT phenomenon occurs at higher H fields. Inset: magnification of the orange highlighted region.

where $\sigma_N(T) = [\rho_N(T)]^{-1}$ is the normal state conductivity. The experimental paraconductivity is defined in terms of the measured resistivity as $\Delta\sigma_{\mathrm{exp}}(T) = [\rho(T)]^{-1} - [\rho_N(T)]^{-1}$. Substituting the values of the standard parameters, equation 4.6 can be expressed in a simplified form:

$$\Delta\sigma_{AL}(T) = \frac{1521}{s\sinh\left(\frac{\epsilon}{s}\right)}, \tag{4.9}$$

where, 1521 $(\Omega \cdot \mathrm{m})^{-1}$ represents the prefactor associated with the film thickness, and it can be expressed as $e^2/16\hbar d$, where d is the thickness of the MO10 film (10 nm), $\hbar$ is the reduced Planck constant, and e is the elementary charge. The s value is a high-temperature

dimensionless cutoff, possibly related to the pseudogap [120] and is used as a fitting parameter. The value of ϵ during the fitting is taken as: $\ln(T/T_{\mathrm{C}})$.
The characterization of BKT transition by the $\rho(T)$ measurements relies on the utilization of the Halperin-Nelson theory to explain its behavior. However, it is crucial to investigate the fluctuation conductivity that persists after the BKT transition to observe and comprehend the gradual effects occurring in the system. Therefore, the equation used to describe the Halperin-Nelson paraconductivity is given by:

$$\Delta\sigma_{HN}(T) = [\rho_N(T)]^{-1} a_{\mathrm{HN}} \sinh\left[\frac{b_{\mathrm{HN}}\,(T_{\mathrm{BKT}})^{1/2}}{(T - T_{BKT})^{1/2}}\right] \tag{4.10}$$

where the temperature T_{BKT}, and the dimensionless parameters a_{HN} and b_{HN} are taken as fitting parameters.
To examine the contribution of the fluctuation mechanism, we have plotted the HN paraconductivity and AL paraconductivity in the same plot (see figure 4.7) and as a function of $\epsilon = \log(T/T_{\mathrm{C}})$, where $T - T_{BKT} = T_C\,\mathrm{e}^{\epsilon} - T_{BKT}$. From the analysis carried out, we have obtained the dimensionless parameter a_{HN} constantly as 0.0048, except when $B = 0$, where $a_{\mathrm{HN}} = 0.0050$, while b_{HN} lies between 0.68 (@$H = 0\,\mathrm{G}$) and 0.73 (@$H = 150\,\mathrm{G}$); T_{C} varies between 12.460 K and 11.55 K, and T_{BKT} varies between 12.285 K and 11.35 K, with $T_{\mathrm{C}} - T_{\mathrm{BKT}} \approx 0.2\,\mathrm{K}$ in the entire range. In Tab. 4.1, we report the values of the fitting parameters for some selected H fields.

In the presence of H, the HN equation starts to deviate significantly from the experimental data, with a gradual crossover from the HN to the Ginzburg-Landau (GL) description. Moreover, under an applied $H = 150$ G, Equation (4.10) gradually fails to fit the data, both close to the critical temperature, where a magnetic-field-driven foot develops, and further away from the transition, where the data are much better described by the AL equation (Eq.4.9, Fig. 4.7). The deviation near the foot starts to appear at as small as 20

Table 4.1: Parameters derived by the least square fitting of the sheet resistance data using the Cooper-pair fluctuation model [Eq. (4.9) and Eq. (4.10)], for film MO10.

H (G)	T_C (K)	s	a_{HN}	b_{HN}	T_{BKT} (K)
0	12.46	0.075	0.0050	0.68	12.285
7	12.07	0.057	0.0048	0.68	11.88
50	11.62	0.029	0.0048	0.72	11.42
100	11.55	0.032	0.0048	0.72	11.35

G field intensity, showing a gradual divergence of the BKT physics instead of an abrupt vanishing effect as detected in the high field regime.

This behavior is also evidenced by the progressive decrease in the crossover temperature, T_{cr} (Fig. 4.8, inset), which is defined as the temperature at which the crossover between the HN and the AL fitting functions of the paraconductivity takes place. Therefore, the value of T_{cr} enabled us to identify the H field-induced crossover from BKT physics to GL physics (Fig. 4.8, inset). These findings align with the observations made regarding the behavior of T_C for MO10. In the presence of H, we detect a progressive lowering of T_{cr}, allowing us to identify the H-field-driven crossover at $H \approx 15 \div 20$ G from the BKT to the GL physics in agreement with findings of T_C behavior of sample MO10, explained in the previous section.

To study the crossover behavior in more detail, we analyze the paraconductivity. In the absence of any applied H field, the HN approach, Eq. (4.10), succeeded in fitting the fluctuation conductivity of a thin NbN film (MO10), in the region following the SC transition, where the BKT mechanism persists (Inset of Fig. 4.8). Subsequently, the highest T range values plotted in the graph, are dominated by the 2D AL regime. However, in the presence of the H field, the HN equation starts to deviate gradually with the increase

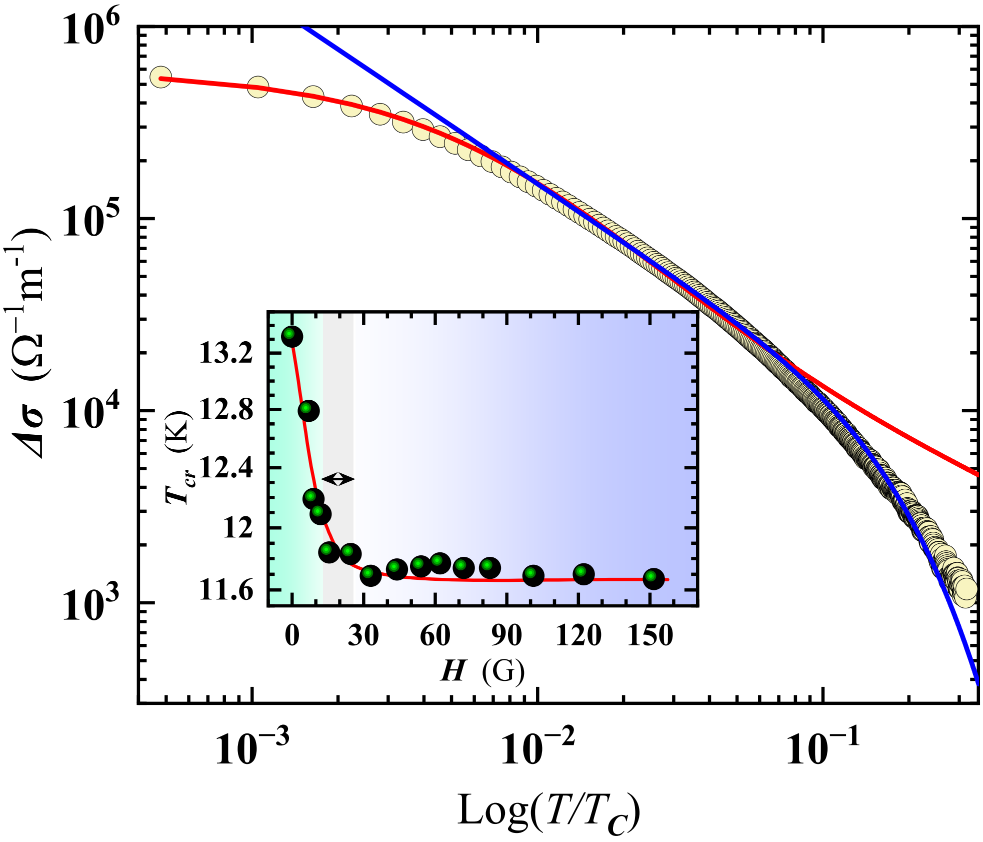

Figure 4.8: a) Paraconductivity of MO10 as a function of the reduced temperature, under an applied field of $H = 0$ G. Lines are least-squares fitting derived by the AL (blue, Eq. 4.9) and HN (red, Eq. 4.10) equations. Inset. H-field dependence of the crossover temperature, T_{cr}, defined as the crossing point of the AL and HN least square fitting curves by Eqs. (4.9) and (4.10). The transition region from the BKT (pale green) to the BCS-like (pale blue) physics has been highlighted by a grey-filled area ($\approx 15 \div 20$ G). The red line is a guide for the eye.

at each field intensity and deviating more sizably from the data (FIG. 4.8). While the H-N region with applied field intensity started to deviate, the AL description is extended, accounting for the dominance of the fluctuations as the field intensity increased allowing to identify a magnetic-field-driven crossover from the BKT to the GL physics.

This gradual suppression of the BKT physics in the resistivity measurements has provided some major evidence of a suppression effect in the phenomenon by the field-induced vortices. The number of induced vortices even at the weakest magnetic field of 3G is substantially large which results in the screening of the logarithmic interaction between VAPs. This results in affecting the dynamics of the interaction and effectively suppressing the BKT transition. However, the smearing of BKT physics does not significantly impact the SC state, which remains preserved, particularly in the weak field regime, allowing for selective control of fluctuation effects.

4.2.5 Dependence of the superfluid stiffness on the weak magnetic fields

Our previous studies conducted under high magnetic fields revealed an absence of non-linear behavior in the I-V characteristics near T_{BKT}, as well as a lack of the expected α jump. These unexpected findings prompt a deeper investigation into the system's response to weak magnetic fields. To examine this, we have determined the exponent $\alpha(T)$ from the slope of the $V - I$ characteristics, measured at several temperatures close to T_C, as exhibited in the figure 4.9 at $H = 5\,\mathrm{G}$.

Interestingly, we have observed a sensitive H dependence of $\alpha(T)$ on the applied field intensities. At H as low as 5 G, α is downward shifted, and its slope starts to decrease (Fig. 4.9). This shift continues up to 15 G, while at 50 G, a sizable lowering of the curve slope occurs, together with a discontinuous change in the α values (Fig. 4.9). At 100 G, increasing T up to 11.6 K, α saturates at a value of ≈ 2.5, to finally converge to $\alpha = 1$ at $T \approx 12\,\mathrm{K}$. As it is known, at $T = T_{\mathrm{BKT}}$, J_S is expected to jump discontinuously, from $J_S(T^-_{\mathrm{BKT}}) = 2T_{\mathrm{BKT}}/\pi$ to $J_S(T^+_{\mathrm{BKT}}) = 0$, giving $\alpha(T^-_{\mathrm{BKT}}) = 3$ and $\alpha(T^+_{\mathrm{BKT}}) = 1$, respectively. To gain additional insight into the smearing of the BKT transition with increasing H field, we have derived the SC stiffness close to the transition from the data of the α exponent, as reported in Fig.4.10. The value of the stiffness is extracted from the $V - I$ characteristics as $J^{\alpha}_S(T) = (\alpha - 1)T/\pi$ [65].

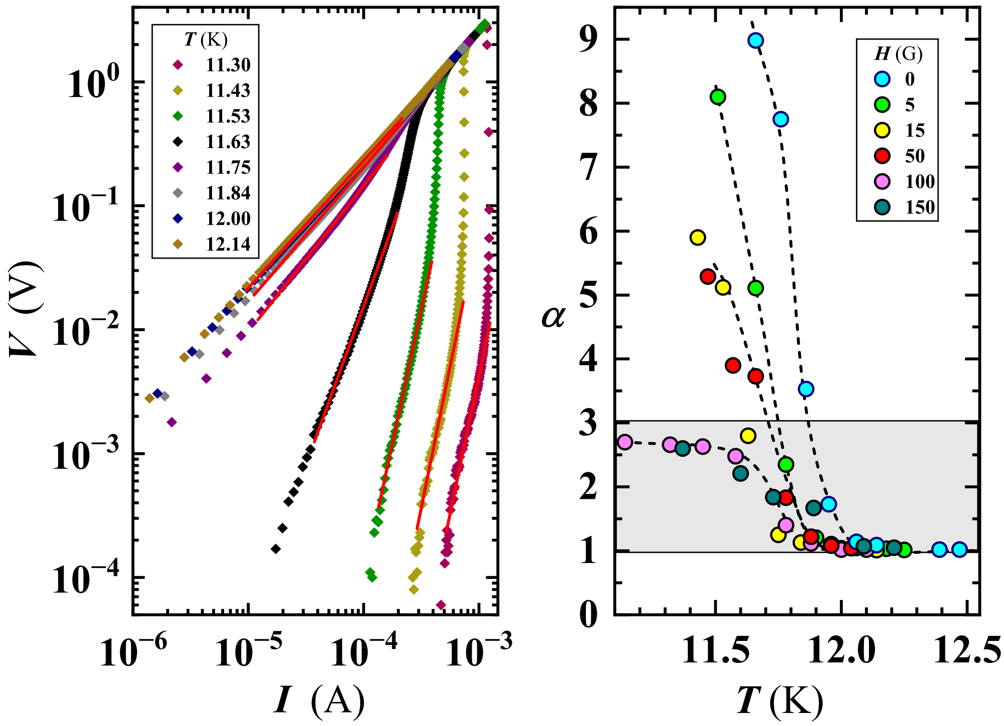

Figure 4.9: **Left:** $V - I$ curves of MO10, at several T close to T_C, under an applied field of $H = 5\,\mathrm{G}$. Red lines are least square fitting by the relation $V \propto I(T)^{\alpha(T)}$ of curves measured at (from right to left): 11.30 K, 11.43 K, 11.53 K, 11.63 K, 11.75 K, 11.84 K, 12.0 K, and 12.14 K. **Right:** Temperature dependence of the fitted α exponent for several H field intensities.

In the case of $H = 0$ G, J_S shows quite an abrupt jump at the T_BKT and its T dependence before the transition has been fitted by the functional dependence of the renormalization group equation [92]:

$$J_S(T) = 2T/\pi + 4AT/\sqrt{(T_\mathrm{BKT} - T)}/(\pi^2) \tag{4.11}$$

where the fitted parameter is $A = 10.4 \pm 0.6\ \mathrm{K}^{-1/2}$. The agreement between experiment and theory is excellent, pointing toward an accurate BKT description of the superconducting transition at zero field. With a further increase in H intensity, the sharpness of the jump starts to smear and the fit completely fails. To account for this smearing, we

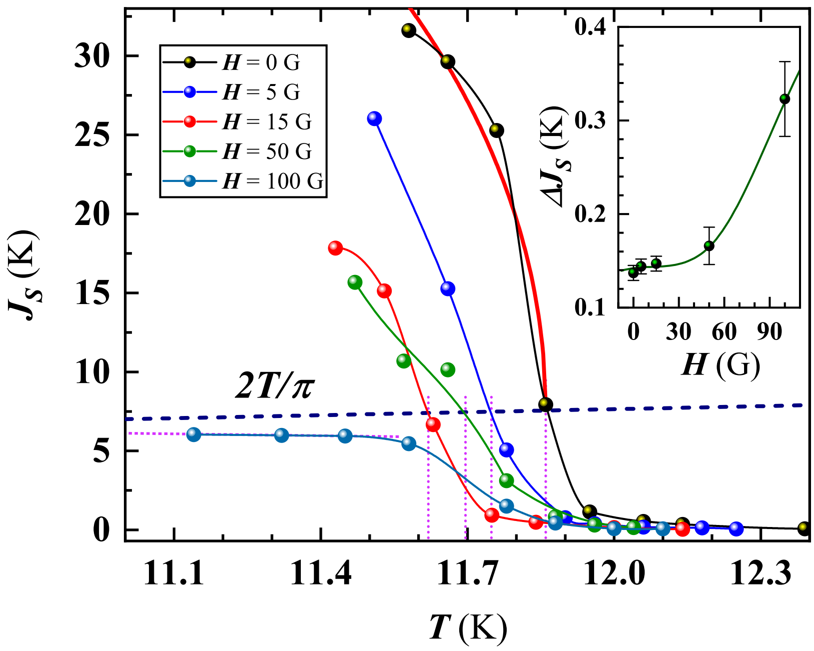

Figure 4.10: Temperature dependence of the SC stiffness of MO10, derived from α values (see text) reproduced in Fig.4.9, at several H field intensities. Experimental values at $H = 0$ G have been fitted by the Eq.(4.11) for $T \leq T_{BKT} = 11.86$ K, value obtained by the intersection of the $2T/pi$ (wine, broken) with J_S interpolating lines. The fitted parameter of Eq.(4.11) is $A = 10.4 \pm 0.6$ K$^{-1/2}$. Inset: field dependence of J_S width, estimated as the T difference of the 10and 90% of the J_S value, assumed as the interception of the $2T/pi$ line with the curve interpolating the experimental behavior. The error bars represent the uncertainty in the T difference related to the choice of the curve interpolating data. The line is a guide for the eye.

have estimated the width of J_S (ΔJ_S) of the jump starting from the intersection with the universal line $2T/\pi$. The $\Delta J_S(H)$ trend further confirms the progressive smearing of the BKT physics with increasing H (see inset of figure 4.10).

4.3 Key Findings and Final Thoughts

Our experimental investigation into the Berezinskii-Kosterlitz-Thouless transition under varying magnetic field intensities has unveiled a pronounced field sensitivity in two-dimensional superconducting systems. The study reveals a nuanced evolution of the superconducting state: at higher field strengths, the BKT physics is entirely suppressed, while lower field values yield significant and intriguing results. We observed a gradual and continuous crossover from the BKT regime to BCS-like behavior, initiating at a field intensity of 5 G and culminating in complete suppression at 100 G.

The underlying mechanism for this behavior is attributed to the introduction of a substantial density of field-induced free vortices. These vortices effectively screen the logarithmic vortex-antivortex pair (VAP) interactions characteristic of the BKT phase in two-dimensional films. The field-dependent behavior of various superconducting properties further corroborates the impact of these free vortices on the system physics.

Our findings underscore the critical importance of considering extremely low magnetic fields in the study of two-dimensional or quasi-one-dimensional superconducting systems—an aspect often overlooked in characterization studies. This investigation provides novel insights into the BKT transition under the influence of weak magnetic fields, highlighting the need for refined theoretical models that can accurately capture the intricate physics of the BKT phenomenon in this regime.

In conclusion, this study contributes significantly to our understanding of the interplay between the BKT transition and weak magnetic fields in low-dimensional superconductors, opening new avenues for both theoretical and experimental explorations in this field.

Chapter 5

Phase slips in NbN Nano-films: From Quantum to Thermal Regimes

5.1 How fluctuations manifest in a Quasi-1D Superconducting films?

In macroscopic superconducting systems, negligible fluctuations typically allow for the existence of an ideal superconducting state. However, as we transition from a bulk to a 2-D superconducting (SC) system, several new features start to emerge. These include residual resistance, non-linearity, and transition broadening, which manifest as the Berezinskii–Kosterlitz–Thouless (BKT) effect. As the superconducting channel dimensions are further reduced to $d, w \leq \xi$, the influence of fluctuations becomes increasingly dominant, effectively destroying the superconducting state. This phenomenon was first observed by William Little in 1967 [121] and predicted as phase slips [122].

The investigation of phase slip effects has attracted significant attention for several years due to their numerous technological applications. These applications include the development of quantum nanodevices, single photon detectors [123], ultrasensitive radiation detectors, and nanocalorimeters. This effect emerges fundamentally due to the reduced dimensionality and enhances the fluctuations of the order parameter which approaches zero over a very small length of dimension close to ξ.

These fluctuations create a phase difference of $\Delta\theta = 2\pi$ across the ends of the wire, causing a momentary blockage of current flow in a specific region of the SC system, making it resistive. These sudden transitions to a resistive state within the SC system are called phase slip events. The locations where these events occur are called phase slip centers [91, 104].

The mechanism of phase slip depends on a one-dimensional order parameter (see Fig. 5.1), $\Psi(x) = \Psi_0 e^{\iota nx}$. This order parameter can be visualized in the complex plane as a helix with radius Ψ_0 and pitch $2\pi/n$, where n is the number of windings. In a steady state without fluctuations, the phase number n remains constant, and its specific value is irrelevant since $e^{\iota\phi} = e^{\iota(\phi+2n\pi)}$.

For n to change, the magnitude of the order parameter $|\Psi|$ must vanish, crossing the x-axis (Fig. 5.1). This requires overcoming an energy barrier associated with suppressing the superconducting condensate within a region of length comparable to the coherence length, ξ. Each crossing of the x-axis corresponds to a phase slip event, where the winding number n changes by 1 and a 2π phase difference develops across the point where $|\Psi| = 0$.

Changes in the winding number n, and thus phase slips, can occur through two distinct mechanisms: quantum phase slips (QPS) and thermally activated phase slips (TAPS). QPS arise from quantum tunneling and are typically observed at temperatures far below the critical temperature, where thermal effects are negligible. In contrast, TAPS are driven by thermal fluctuations and become significant near the superconducting transition temperature.

Although phase slip events were initially observed in one-dimensional systems, it was later discovered that similar fluctuation effects also occur in 2D systems. These are analogous to phase slip centers (PSCs) and are known as phase slip lines (PSLs), albeit with

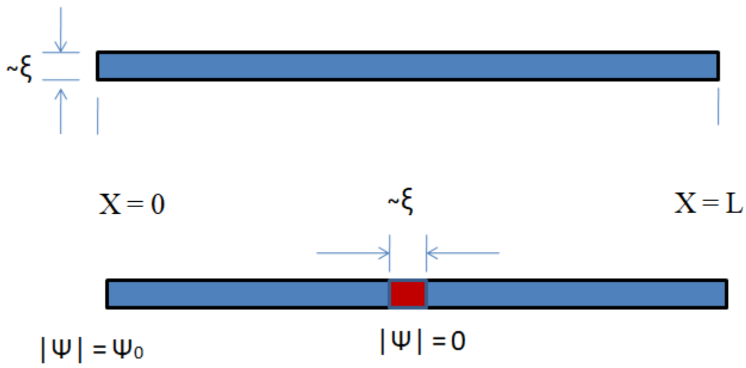

Figure 5.1: Demonstration of a phase slip event in a superconducting wire of length l. The order parameter, represented by the rotating arrow, undergoes a 2π phase slip as its magnitude goes to zero at a specific point along the wire. This process momentarily disrupts the superconducting state, leading to a voltage drop across the wire.

a different physical mechanism.

Simulation work using time-dependent Ginzburg-Landau equations shows that PSLs are river of kinematic vortices that move across the superconducting strip perpendicular to the current flow. When a vortex crosses the strip, it carries magnetic flux, which leads to a voltage pulse. These vortices tend to annihilate in the middle of the superconducting system, further contributing to the voltage generation. This process results in I-V characteristics with voltage steps or jumps, similar to those observed for PSCs due to phase slip events. An important aspect of PS events is that they arise from intrinsic fluctuations, such as thermal fluctuations of the order parameter or fluctuations in vortex density, which momentarily drive the system away from equilibrium. However, the system eventually returns to equilibrium, making these events non-equilibrium phenomena.

The Dynamics of Phase Slip Phenomena in Superconductors

Consider the fundamental concept of connecting two superconductors through a weak link of lateral dimension $\approx \xi$. The physics becomes particularly intriguing when this weak link facilitates the exchange of Cooper pairs between the two superconductors, establishing phase coherence. When a current starts to flow through these weak links, a phase difference θ arises between the two superconductors, given by the relation established for the Josephson junction: $I_S = I_C sin\theta$. The critical current, I_C, is given as [91]:

$$I_C = \frac{e\hbar {n_s}^0}{2m}\xi \tag{5.1}$$

where ${n_s}^0$ is the superfluid density. In reality, the phase difference θ between superconductors does not typically remain constant and exhibits distinct features based on their origin.

Before delving into the details of each mechanism, let's first examine the physical effects of these two distinct types of fluctuations on the superfluid density, n_S, and the critical current, I_C, of the weak link.

We can express the phase difference as $\theta + \Delta\theta(t)$, where $\Delta\theta(t)$ represents the fluctuating component. The average current value is then given by:

$$\langle I_S \rangle = I_C \langle sin(\theta + \Delta\theta) \rangle = I_C \langle cos(\Delta\theta) \rangle sin\theta \tag{5.2}$$

Expanding $\langle cos(\Delta\theta) \rangle \approx (\frac{-\langle(\Delta\theta)^2\rangle}{2})$ and $\langle(\Delta\theta)\rangle^2$ gives the average of fluctuation along its mean value, and the effective critical current of the junctions is decreased from its original value I_C to:

$$I_C^{'} = I_C exp\langle(-\Delta\theta)^2\rangle/2) \tag{5.3}$$

Comparing with equation 5.1, we obtain:

$$\frac{n_s}{{n_s}^0} = exp\left(\frac{\langle -(\Delta\theta)^2 \rangle}{2}\right) \tag{5.4}$$

which gives a suppression in the value of low-temperature superfluid density. However, for an accurate estimate, we need to calculate the $\langle(\Delta\theta)^2\rangle$.

First, we begin with a simpler case, i.e., classical phase slip lines (TAPS), for which the energy of the weak link is given by:

$$E_J = \frac{\hbar}{2e} I_C \tag{5.5}$$

where E_J is the Josephson coupling energy. By substituting the value of I_C, we can express the coupling energy in terms of the coherence length and superfluid density:

$$E_J = \frac{\hbar^2 n_S}{4m} \xi \tag{5.6}$$

In the case of fluctuations, the critical current value reduces, changing the coupling energy to:

$$E_J{}' = -E_J(1 - \langle(-\Delta\theta)^2\rangle/2) \tag{5.7}$$

For the case when $I = 0$, the phase angle $\theta = 0$, resulting in $cos\theta = 1$ and simplifying the equation to: :

$$(\Delta\theta)^2 \approx \frac{k_B T}{E_J} \tag{5.8}$$

Replacing the value of θ in the superfluid density equation 5.4:

$$n_S = n_S{}^0 \left(1 - \frac{k_B T}{2E_J}\right) \tag{5.9}$$

The derived equation indicates a linear decrease in superfluid density, n_S, at temperatures where fluctuations lead to the formation of thermally activated phase slip lines.

In the case of quantum phase slips (QPS), an additional energy scale comes into play: the charging energy arising from the exchange of Cooper pairs through the weak link. When two superconductors are connected, with capacitance C, they result in Coulomb energy of

Q^2/C associated with the charge difference between them. This charge difference arises due to the tunneling of Cooper pairs across the weak link, where $Q = 2eN$ and N is the number of Cooper pairs.

QPS becomes particularly important when this charging energy ($E_C = Q^2/C$) is comparable to or larger than the Josephson energy (E_J). This typically occurs when the size of the weak link becomes sufficiently small (of the order of $\approx \xi$). In this regime, E_C creates a significant energy barrier for each Cooper pair tunneling event, hindering the continuous flow of Cooper pairs and leading to discrete tunneling events. As a consequence, quantum fluctuations of the phase difference between the superconductors become important, giving rise to QPS. This phenomenon highlights the intricate interplay between tunneling dynamics, such as the rate of Cooper pair tunneling and how it's affected by the charging energy, and the emergence of novel quantum effects as the effective dimension of the weak link is reduced. Such effects have been observed in systems like superconducting nanowires and Josephson junctions with small capacitance.

We begin by formulating the Hamiltonian of the system:

$$H^J = -E_J Cos\theta - 2E_C \frac{\partial^2}{\partial\theta^2} \tag{5.10}$$

where E_C is e^2/2C. The ground state of the system can be derived from its Hamiltonian by employing a variational technique. The probability density corresponding to the ground state wave function is illustrated in Figure 5.2. There are two cases to study: when $2E_C/E_j >> 1$, which gives a constant value of the ground state function $|\Psi(\theta)|^2$ and $E_C/E_j << 1$, for which the value of $\langle(\Delta\theta)\rangle^2$ goes lower than 2π, which makes the application of variation approach extremely difficult.

In that case, we consider a trial function:

$$\Psi(\theta) = exp\left[\frac{-\theta^2}{4\sigma^2}\right] \tag{5.11}$$

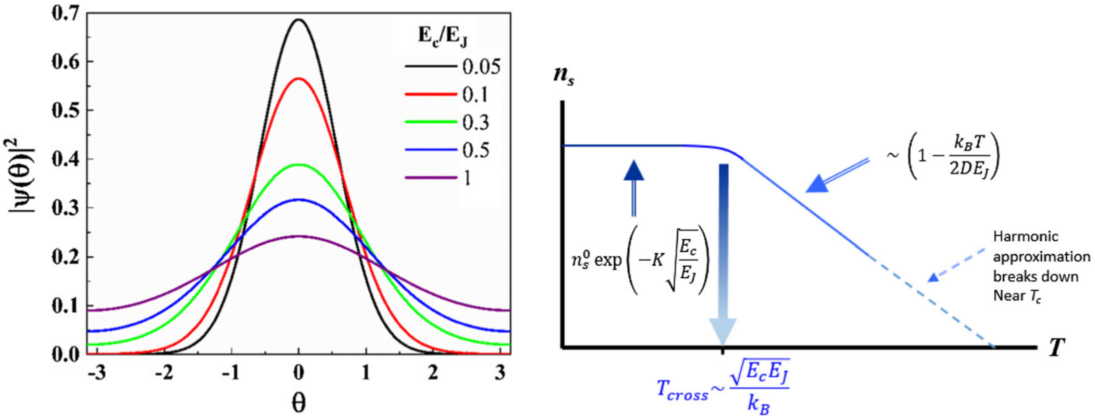

Figure 5.2: **Left**: The square wave function modulus is shown for two small ($\approx \xi$) superconducting channels in their ground state. The area under the curve represents the uncertainty in the phase θ as the ratio E_C/E_J increases. **Right**: The variation in the superfluid density is shown for a crossover from QPS to TAPS. This crossover takes place at a temperature close to the corresponding plasma frequency, $k_B T_{cross} \approx \hbar\omega_p \approx (E_C E_J)^{1/2}$. However, when the SC system is dissipative, the value of n_s decreases with the temperature variation of T^2 at lower temperatures, and the crossover region shifts to the lower temperature value[91].

solving the function and calculating its expectation energy will give a final equation:

$$\frac{n_S}{n_S^0} = exp\left(\frac{-1}{2}\sqrt{\frac{E_C}{E_j}}\right) \tag{5.12}$$

At T= 0, in the case of $\left(\frac{E_C}{E_j}\right)^{1/2} >> \frac{k_B T}{E_j}$, making n_S temperature independent. On the other hand, for higher T, $\left(\frac{E_C}{E_j}\right)^{1/2} << \frac{k_B T}{E_j}$, a linear dependence with the temperature is observed till the point where the quasi-particle excitation becomes significant, as shown in fig 5.2. In the next section, we will derive the temperature-dependent resistivity relationship for both quantum and thermal phase slips by considering the energy scales necessary to accurately describe their presence in the NbN superconducting ultra-thin films.

Thermally activated phase slip lines (TAPS)

As discussed in the previous section, increased granularity and disorder in quasi-one-dimensional superconducting systems can lead to weak localization and inhomogeneous effects, which in turn give rise to one-dimensional features such as phase slip (PS) events [104, 124, 125]. Consequently, these systems become prone to forming arrays of continuous conductive paths with effective dimensions much smaller than the physical dimensions of the system. In that case, a region equivalent to the coherence length can create a Josephson-like junction, which shows a PS barrier proportional to the area of the quasi-1D SC system. At temperatures below T_C, thermal fluctuations can provide sufficient energy for Cooper pairs to overcome these barriers, resulting in phase slips and associated voltage drops. These events contribute to the observed resistance in the superconducting state [125].

However, to accurately anticipate the behavior of resistance below the critical temperature (T_C), it is essential to study the temperature dependence of phase slip events. Initial investigations focused primarily on the formation of thermal phase slip events, which we shall begin with our analysis. Before going into the experimental details, we first try to understand the mechanism which was given by the successful theory of Langer, Ambegaokar, McCumber and Halperin (LAMH), specifically derived for thermally activated phase slips. [85, 122, 126, 127].

We begin by considering an unbiased system, where an equal number of phase slips (corresponding to a change of θ by 2π) and anti-phase slip lines (corresponding to a change of θ by -2π) are present. When a biased current is applied to this system, it disturbs the equilibrium state, leading to an imbalance between the number of phase slips and anti-phase slips. Consequently, a voltage is generated across the sample, as described by the LAMH theory, V = ($\hbar\theta$) / (2e), where θ represents the rate of change in the phase difference across the sample, $\hbar$ and e are the physical constants.

In the case when the bias current is non-zero and the thermal activation of phase slip occurs, the order parameter of the system becomes zero, increasing the free energy of the system. In this scenario, the activation energy barrier, denoted as $\Delta F(T)$, can be overcome with a rate proportional to $(\omega(T)/2\pi)e^{\frac{\Delta F}{k_B T}}$, where $\omega(T)$ represents the attempt frequency associated with thermal fluctuations, k_B is the Boltzmann constant, and T is the temperature.

$$\theta = \Omega(T)e^{-\Delta F_+(I)/k_B T} - e^{-\Delta F_-(I)/k_B T} \tag{5.13}$$

where ΔF_+ and ΔF_- are the barrier energy for Phase slip and anti-phase slip respectively. In the case of a 1D system, the time-dependant Ginzburg-landau approach is used to estimate the attempt frequency given by:

$$\Omega = \frac{L}{\xi(T)} \frac{1}{\tau_{GL}} \left(\frac{\Delta F}{k_B T} \right)^{1/2} \tag{5.14}$$

where τ_{GL}, is the relaxation time and is inversely proportional to attempt frequency. The value of relaxation time is $\pi\hbar/8k_B(T_C - T)$, where T_C is the mean-field critical temperature. In the equation 5.14, the value $\Delta F/k_B$T gives the correction factor for the phase slip lines which may overlap, and originate at different places in a superconducting system. Therefore the free energy barrier is given by, ΔF which is defined as the Condensation energy density x volume of the phase slips.

$$\Delta F = \frac{8x\sqrt(2)}{3} \frac{{H_C}^2(T)}{8\pi} A\xi(T) \tag{5.15}$$

For the case, when a biased current is applied, voltage can be written as:

$$V = \frac{\hbar\Omega(T)}{e} e^{-\Delta F/k_B T} Sinh(I/I_0) \tag{5.16}$$

and their derivative is given as:

$$\frac{dV}{dI} = \frac{\hbar\Omega(T)}{e} e^{-\Delta F/k_B T} Cosh(I/I_0) \tag{5.17}$$

In the case when the applied current is small, $I << I_0$, ohms law is written as:

$$R_{LAMH} = \frac{\hbar\Omega(T)}{eI_0}e^{-\Delta F/k_B T} = R_q(\hbar\Omega(T)/k_B T)e^{-\Delta F/k_B T} \tag{5.18}$$

where R_q is the quantum resistance given by $h/2e^2 = 6.5k\Omega$.

To be precise, the phase slip energy was calculated by Langmer and Ambegaokar [81] and in the late 1970 McCumber and Halperin derived the attempt frequency which together became LAMH theory. The idea was originally developed for very long wires, thinner than ξ, whose fabrication became possible after the innovations in the field of nanotechnology. In the early experiments, to verify the occurrence of thermal phase slips, fitting of the Resistance with the LAMH equation was used, which was first time reported in 1970 in the tin whiskers [128]. Thereafter, several groups performed experiments and reported the successful fit of the Resistance measurements [125, 129–131].

5.1.1 Quantum phase slips

The theoretical discovery of the phase-slips arising due to the quantum origin [130] was first studied in the year 1987, which was later confirmed experimentally in the same year[132]. It was observed that there is an enhanced broadening in the superconducting transition, which can no longer be described by considering the LAMH theory.
Giordano [82] was the first to describe the dynamics of the order parameter in the quantum regime, suggesting a mechanism similar to TAPS, except that appropriate energy scale $k_B T$ is replaced by $\hbar/\tau_{GL}$, resulting in the equation:

$$R_{QPS} = B\frac{\pi\hbar^2\Omega_{QPS}}{2e^2\frac{\hbar}{\tau_{GL}}}exp\left(-a\frac{\Delta F\tau_{GL}}{\hbar}\right) \tag{5.19}$$

where B and a are numerical factors of ≈ 1 and Ω_{QPS} is defined as:

$$\Omega_{QPS} = \frac{L}{\xi}\left(\frac{\Delta F}{\frac{\hbar}{\tau_{GL}}}\right)\frac{1}{\tau_{GL}} \tag{5.20}$$

The model predicted that even at T = 0 K, the nanowire having quantum phase slips will produce a finite resistance. The interesting approach would be to compare the resistance measurements by applying the LAMH and Giordano's equations in order to determine the crossover temperature where thermal and quantum phase slip rates become equal. To investigate this, we will present key experimental results obtained in this study on NbN ultra-thin films with a thickness d$\approx \xi$.

Experimental evidence of phase slip phenomena from resistivity measurements

To carry out a comprehensive study, we measured the temperature-dependent resistivity for ultra-thin NbN films having a thickness of 5 nm, which is kept constant for the films displaying phase slip effects. The novelty lies in the manipulation of the Hall bar width, with values ranging from 10 μm to 50 μm. It is necessary to note that these dimensions are several orders of magnitude larger than ξ. According to theoretical interpretations, superconducting systems with a ratio of ξ to the width, w, equal to 1 are often considered ideal for exhibiting phase slip behavior. However, several studies [104, 125, 133, 134] have demonstrated the possibility of observing phase slips even when $\frac{w}{\xi} = 25$, which raises the question about the significance of this ideal ratio for observing the phase slip phenomenon. In light of this, we have taken a step forward by investigating the impact of varying the width of the system where the ratio is $w/\xi = 1000$ while keeping the thickness constant.

We began by analyzing the temperature-dependent resistivity, as shown in Figure 5.3. The measurements presented here pertain to selected films exhibiting phase fluctuation effects. We observed a distinctive behavior characterized by a tailing effect, accompanied

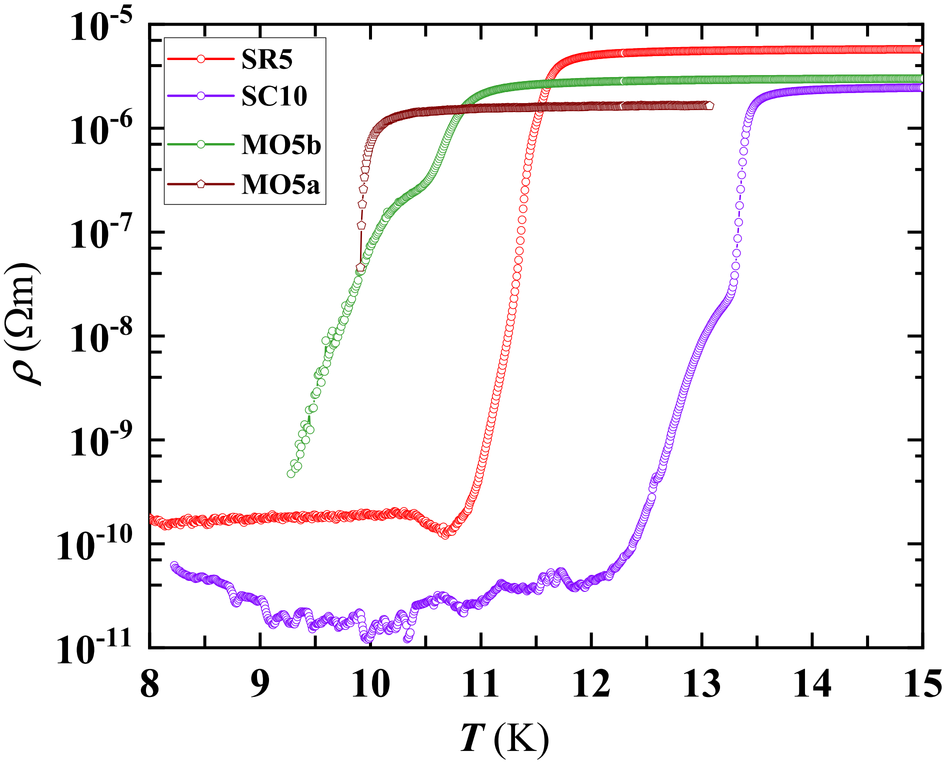

Figure 5.3: Temperature dependence of resistivity near the superconducting transition for 5 nm thick NbN films. The figure illustrates the characteristic behavior as the temperature approaches the critical point, showcasing a distinctive tailing feature in the transition region.

by a pronounced double transition. The lower part of the curve typically represents the temperature range where phase slips occur, followed by a sharp transition.

To identify the presence of thermal phase slips, we applied the Langer-Ambegaokar-McCumber-Halperin (LAMH) equation derived for the TAPS. A least-squares fitting procedure was employed to check the convergence of Equation (5.18), with T_C and β as the fitting parameters.

For our 5 nm thick film on MgO substrate (MO5b), having a width of 10 μm, we have found excellent agreement with the LAMH theory, giving values of T_C and β comparable to those found in ref. [125]. Interestingly, the T_C value obtained through the LAMH aligns precisely with the values derived from the analysis of the resistivity curve (see Table 5.1). This congruence serves as a strong confirmation that the observed fluctuation effects are due to phase slips and can be attributed to a thermal origin.

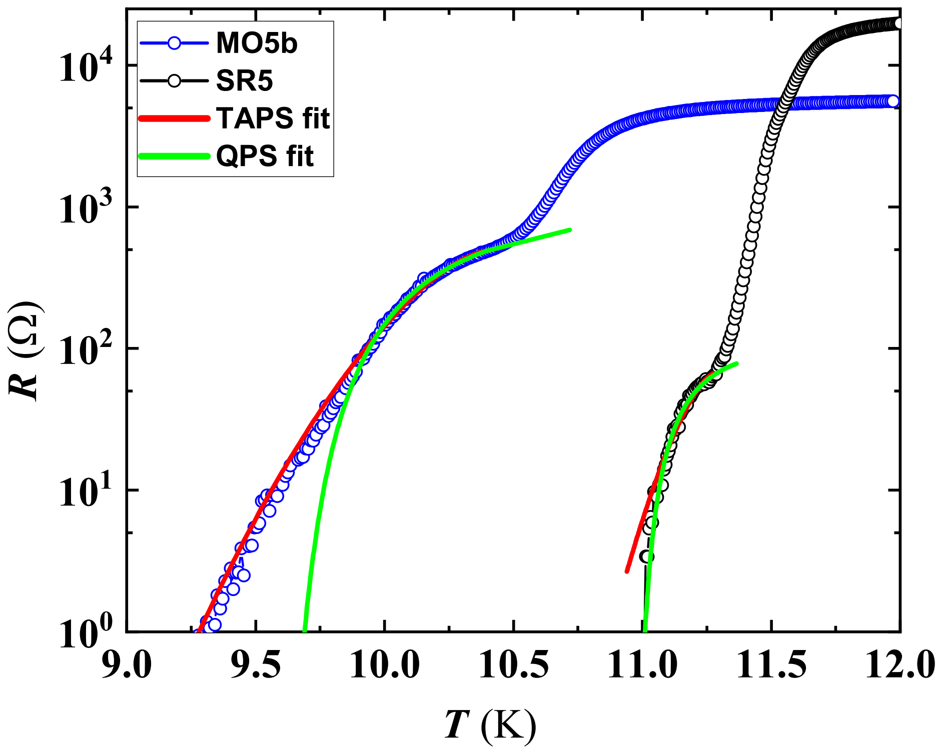

Figure 5.4: Temperature dependence of resistance for two 5 nm thick NbN films. Both curves showed tailing-like features below about 10.25 and 11.5 K for MO5b and SR5, respectively. Branches of the $\rho(T)$ curves exhibiting the transition at the lower T range were fitted by using LAMH theory, Equation (5.18) (red lines), and by Equation (5.19) (green lines).

On the other hand, for our NbN films on sapphire substrate (SR5), having a width of 10 μm, the fitting of the LAMH equation failed in the first steeper branch of the $\rho(T)$ curve (see Figure 5.4). This suggests the possibility of a different fluctuation effect present in the T range where deviation is observed. To confirm our hypothesis, we explored the possible contribution of Quantum Phase Slips emerging from the quantum tunneling of the order parameter through the same free-energy barrier as in TAPS, which is supposed to dominate at lower T. The result of the fitting by Equation (5.19) aligns well with the theoretical predictions for SR5 (see Figure 5.4). On the contrary, for MO5b, progressive deviation from the QPS Equation (5.19) is evident at lower T.

It is important to note that for ultra-thin SC films, during transport measurements, certain

Table 5.1: NbN films superconducting properties, reproduced for the samples exhibiting Phase slip phenomenon (refer chapter 3).

Sample	ρ (Ωcm) (K)	T_c (K)	ΔT_c (K)	J_{c0} (MA/cm^2)
MO5b **	5.8×10^{-5}	11.02	0.79	2.24 ± 0.013
SR5 **	1.1×10^{-4}	11.76	0.68	0.63 ± 0.013
SO5	9.3×10^{-7}	9.40	0.46	0.89 ± 0.024

distinctive features such as tailing effects and double transition phenomena can provide valuable insights into the emergence of phase fluctuations within the system, as discussed above. These observations offer a clue about the nature of the fluctuation phenomenon at play. However, to truly comprehend the underlying mechanisms involved, a more direct representation can be obtained through the analysis of the current-voltage characteristics. Therefore, the subsequent section of our study is dedicated to a comprehensive analysis of the I-V curves at several temperatures, which will shed light on the true nature of the phase slip mechanism.

Signature of the phase slip effects in I-V characteristics

Following our analysis of resistivity measurements, we proceeded to investigate the current-voltage (I-V) characteristics to obtain more direct evidence of phase slip phenomena. The measurements for I-V characteristics were performed using a pulse mode technique, starting from the lowest temperature of 4 K up to T_C. Figure 5.5 illustrates the typical behavior characterized by the observation of multiple resistive branches during both the up-sweep and down-sweep measurements.

To ascertain whether the observed resistive branches are attributable to defects or indicative of phase slip line effects, we considered specific conditions established in the work of Sivakova et al. [135]. The first condition is that an abrupt jump in the voltage is observed from zero to a finite value occurring at a critical current (I_C). Secondly, all resistive branches should converge at the same point on the x-axis (given by the intersection of their slopes with the current axis), referred to as the excess current, I_{ex}, which serves as a crucial signature of the phase slip effect. Furthermore, the differential resistance should be proportional to the number of phase slip events.

Figure 5.5 shows a family of I-V curves measured at different T for SR5 from the lowest temperature of 4.8 K up to T_C, where multiple slanted steps known as resistive branches were detected. Each voltage jump observed on the I-V curve corresponds to the generation of an additional phase slip line within the film. As we move along consecutive resistive branches, there is an observable increase in the slope, which is directly influenced by the penetration depth of the electrical field.

The dynamic resistance of these branches rises at increasing V (e.g., along the I-V sweep-up direction, (see Fig.5.6, left), and the current axis intercept (extending tail slope) occurs for a common current value of $I_{ex} \simeq 0.38$ mA, shown in Fig. 5.6 (right). Interestingly, when a sufficiently high current is applied to the system, it effectively reduces the distance between the phase slip lines, ultimately approaching the ohmic regime. In this regime, the slope of the I-V curve becomes equal to the resistance exhibited by the sample in its normal state.

These findings provide strong evidence supporting the notion that the detected resistive states are indeed caused by phase slip effects. The observed behavior in the I-V characteristics, including the multiple resistive branches, the convergence at I_{ex}, and the transition

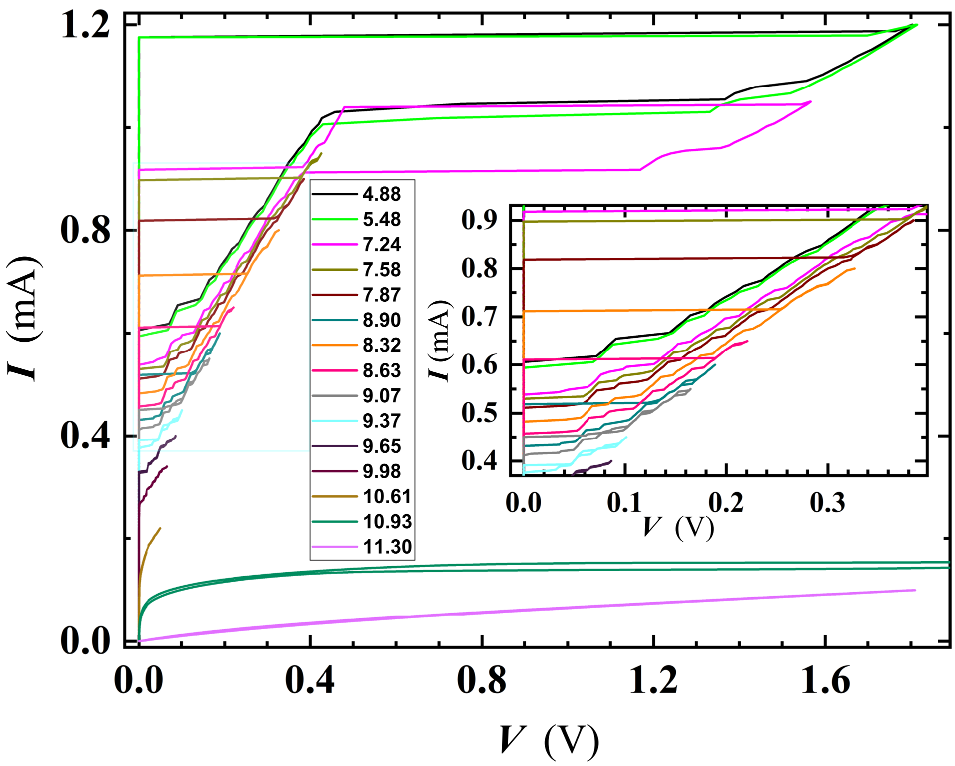

Figure 5.5: I-V characteristics for the SR5 film, carried out at several T. Both up and down-current sweeps evidence the presence of slanted steps due to the occurrence of intermediate resistive regimes before the complete transition to the normal state. Inset: magnification of the central part of the plot.

to the ohmic regime at high currents, all align with the expected signatures of phase slip phenomena in superconducting thin films.

Further analysis of the I-V curves evidenced interesting temperature dependence of the number of the resistive states appearing in the sweep-up ($N^{\uparrow}$) and sweep-down ($N^{\downarrow}$) branches of the I-V curves (Figure 5.6). The $N^{\uparrow}$ and $N^{\downarrow}$ kept an almost constant value up to $T \approx T_c/2$, and then they started to differ. In detail, at $T \gtrsim T_c/2$, $N^{\downarrow}$ jumps to higher values, and then it decreases till about 9 K. On the contrary, $N^{\uparrow}$ continues to gradually increase till 9 K. Onward from 9 K, both curves are perfectly overlapped and continuously rise with T. The behavior exhibited by $N^{\uparrow}$ and $N^{\downarrow}$ allows one to derive additional observa-

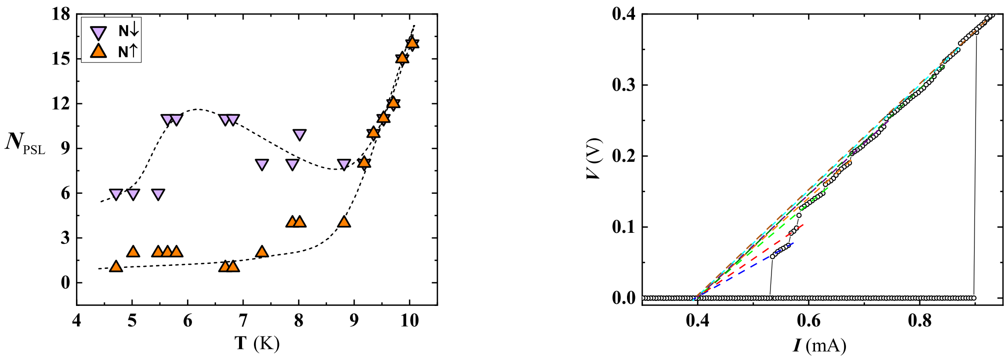

Figure 5.6: **Left** Number of resistive states for SR5, calculated from the I-V curves, during the current sweep-up ($N^{\uparrow}$) and sweep-down ($N^{\downarrow}$). Near to $T \simeq 9$ K, $N^{\uparrow}$ and $N^{\downarrow}$ suddenly converge, assuming the same value at $T \geq 9$ K. Broken lines are guides for the eye. **Right** V-I curve at a few selected temperatures for SR5, showing the convergence of all resistive tails towards a well-defined value of the excess current of $I_{ex} = 0.38$ mA.

tions about fluctuation effects involved in our investigated film. Specifically, the unequal distribution of PS in $N^{\uparrow}$ and $N^{\downarrow}$ suggests that different mechanisms are contributing in three distinct T ranges. Below $T_c/2$, the emergence of phase-slip events is driven by quantum tunneling. In the intermediate T range ($T_c/2 < T < 9$ K), the behavior of $N^{\uparrow}$ and $N^{\downarrow}$ can be explained by the competition of QPS and TAPS, the former tending to decrease approaching 9 K. Finally, above 9 K, only TAPS contributes to the observation of PS events. It is interesting to note that in the region where QPS is present, $N^{\uparrow}$ and $N^{\downarrow}$ diverge. This effect can be explained by a presumably different tunneling route followed by the system, during the sweep up and sweep down of the sourced current in the quantum regime. In the intermediate T range, the system self organizes in order to converge towards a condition dominated by TAPS, then leading to a decrease in $N^{\downarrow}$ with an increase $N^{\uparrow}$. Finally, approaching T_c, thermal fluctuations dominate over QPS, and the entire system is driven by the electrons. Since the electrons tend to track the same path while going sweep-up and sweep-down [136], the number of PS becomes equal, followed by a total increase in the number of PSL, due to enhanced fluctuation effects near T_c.

This detailed analysis reveals clear signatures of both quantum and thermal phase slips in our NbN films, as evidenced by excellent agreement with LAMH and QPS models. Following the theoretical framework established by Joshi et al. [133], we can quantitatively determine the width of nano-conducting paths (NCPs). The analytical model yields the following expression for calculating the NCP width:

$$d_{NCP} = \sqrt{\left(\frac{12\rho_{RT}C\xi_0}{1.76\sqrt{2}\pi R_q}\right)} \tag{5.21}$$

where $\xi_0 \simeq 4$ nm, $C = 8$ (value typically used for quantum systems) [49] and ρ_{RT} is the resistivity value at room temperature (RT). NCP values calculated by using Equation (5.21) were 3.2 nm for SR5 and 7.5 nm for MO5b, which are comparable with those found for NbN nanostructures in ref. [133]. In fact, for SR5, the condition $d_{NCP} < \xi$ (i.e., $\xi \approx 4$ nm) can be considered as the origin of quantum tunneling, resulting in the formation of QPS detected in our film. On the contrary, for MO5b, $d_{NCP} > \xi$, TAPS lines will result, as indeed experimentally observed.

A particularly intriguing paradox emerges from these findings: the significant contribution of quantum effects, originating from presumed 3-7 nm wide NCPs to the electrical properties of Hall bar (w $\approx 10\,\mu$m). Contemporary theoretical frameworks suggest that quantum phase slip phenomena should be confined to structures where w and $d \approx \xi$. However, our experimental results demonstrate robust phase slip effects in structures where w/ξ = 1000, challenging conventional dimensional constraints in superconducting systems. This disparity, consistently observed across all our 5 nm thick films with 10 µm wide Hall bar, strongly suggests the existence of self-organized quantum channels within the broader film structure, likely facilitated by local variations in the order parameter or microscopic inhomogeneities at grain boundaries. The systematic nature of these observations across multiple samples eliminates the possibility of anomalous behavior and points to an intrinsic mechanism governing the formation of these quantum channels. This unexpected phenomenon opens new perspectives for investigating quantum effects in larger superconducting structures and suggests that the traditional dimensional constraints for phase slip effects warrant comprehensive reevaluation.

Further investigation of this phenomenon under applied magnetic fields is crucial for elucidating the underlying physics. Systematic examination of field-dependent behavior could reveal potential suppression mechanisms of phase slips, providing fundamental insights into the complex interplay between magnetic field penetration and phase slip dynamics in these superconducting systems. To elucidate the influence of magnetic fields

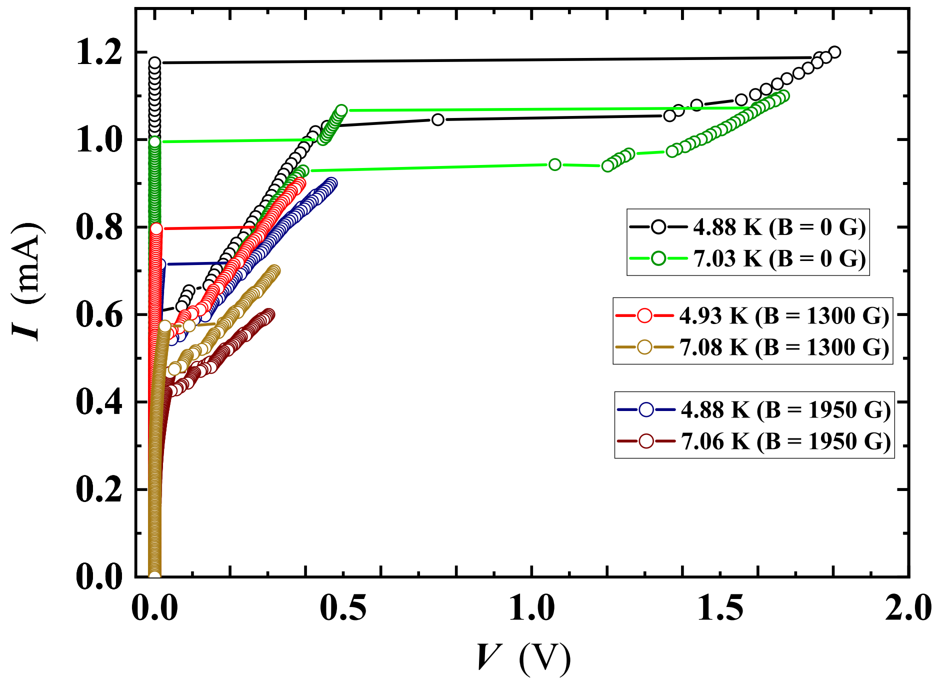

Figure 5.7: I-V characteristics of phase slip lines are shown for a 5 nm thick film deposited on an Al_2O_3 substrate, with measurements conducted at different field intensities. To facilitate a thorough comparison, two temperatures were specifically chosen to account for variations in the number of phase slip lines.

on the phase slip behavior in ultra-thin NbN films, we conducted a series of resistivity and I-V measurements. These measurements were performed under varying perpendicular magnetic field intensities ranging from 1300 G to 3600 G. The I-V characteristics, presented in Figure 5.7 and 5.8, reveal a striking dependence on the applied magnetic field. In the absence of any external magnetic field, a pronounced hysteresis behavior and a higher number of phase slip lines were observed at both 4.88 K and 7.03 K, as expected. However, the application of a 1300 G magnetic field significantly suppressed the hysteresis and reduced the number of phase slip lines. This trend persisted upon increasing the magnetic field intensity to 1900 G, with minimal hysteresis evident even at the lower temperature of 4.88 K.

These initial experimental findings demonstrate that an external magnetic field can effec-

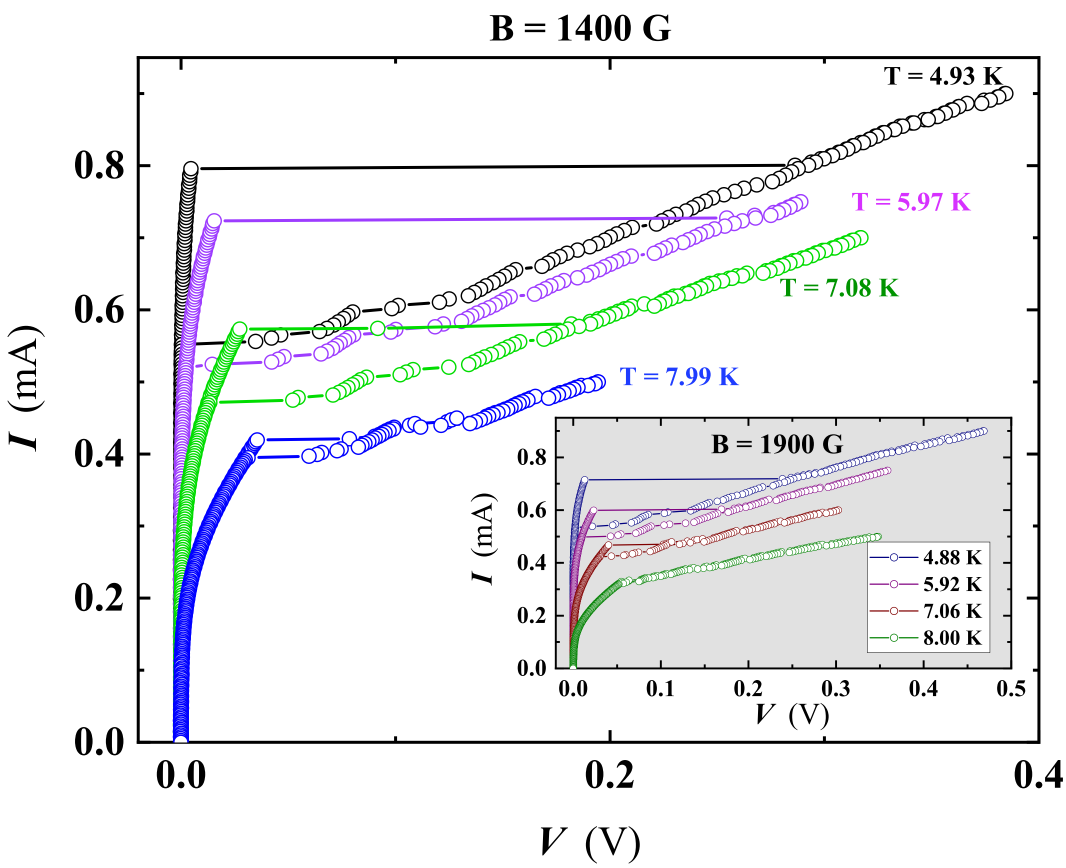

Figure 5.8: I-V characteristics obtained at two high field intensities of 1400 G and 1900 G, spanning across a range of temperature values are shown. The data clearly illustrates a notable reduction in the number of observed phase slip lines, due to the increase in the length of each resistive branch.

tively modulate phase slip dynamics. This modulation is evident in the observed reduction in the number of phase slips, which is a direct consequence of the elongation of individual phase slip lines. Furthermore, as the magnetic field intensity increases, the length of each phase slip line progressively extends until a saturation point is reached, likely corresponding to the critical field of the film. At this juncture, all phase slip lines vanish entirely [124, 135], resulting in a smooth transition devoid of any discernible phase slip effects. This ability to fine-tune phase slip behavior through magnetic field manipulation opens up promising avenues for further research and potential applications in superconducting device engineering. One particularly exciting area is quantum information technology, where the ongoing drive towards miniaturization may inevitably lead to encounters with such phase slip effects. Understanding and controlling these phenomena could therefore prove crucial in the development of next-generation quantum devices.

5.1.2 Simultaneous Observation of Phase Slip Effect and BKT Transition in a Superconducting System

The final result of this chapter presents an intriguing observation of two distinct fluctuation mechanisms in a 5 nm thick NbN ultra-film fabricated on a MgO substrate (MO5). In our study, we observed the presence of thermal phase slip effects (see Figure 5.9), arising due to the 2π phase jumps in the superconducting order parameter, as discussed earlier. Additionally, we detected a Berezinskii-Kosterlitz-Thouless transition, occurring due to the unbinding of vortex-antivortex pairs (refer to Chapter 3) in a temperature range where phase slips become negligible, while the system remains in the superconducting state.

Further analysis of the transport data reveals the interplay between these two fluctuation mechanisms. The presence of BKT was confirmed by the Cooper pair-fluctuation model above T_C, and the scaling behavior of the Halperin-Nelson equation near T_{BKT} (as explained in the BKT section) is confirmed 5.9. Interestingly, in our I-V characteristics,

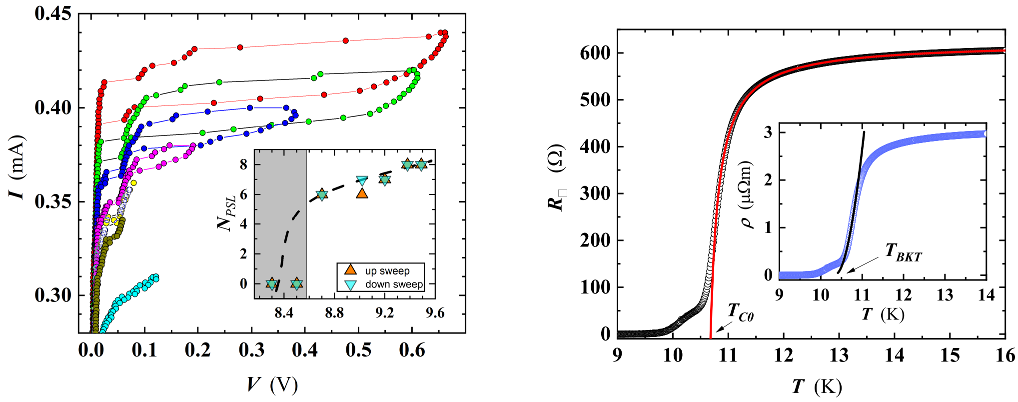

Figure 5.9: I-V characteristics of MO5b, showing the occurrence of steps in the curves close to T_c, progressively disappearing approaching T_c. The T values for the shown curves are 8.70 K (red), 9.02 (green), 9.20 K (blue), 9.38 K (magenta), 9.49 K (yellow), 9.60 K (olive), 9.98 K (cyan). Inset: number of TAPS extracted from I-V curves. The gray rectangle defines the T range where no PSL was detected.

the TAPS become undetectable at 9.9 K, far before reaching T_C (11.02 K, see Table 3.2). This suppression of phase slips gives rise to a BKT transition, an effect typically associated with 2D systems. For $T \approx T_{BKT}$, the unbinding of vortex-antivortex pairs results in the universal jump in α, as detected in the I-V characteristics of MO10. The parameters derived for this film (see Table 3.2) are in good agreement with the theory. The observation of these two distinct phenomena arises due to the complex interplay of granularity and inhomogeneity in the NbN system. Granularity leads to the formation of weakly coupled grains, which can exhibit TAPS, while the overall film retains its 2D nature for the BKT transition.

5.2 Key Findings and Final Thoughts

The comprehensive investigation of ultra-thin NbN films has revealed a rich interplay between dimensionality, disorder, and emergent fluctuation effects. The observation of thermally activated phase slips and quantum phase slips as the film thickness approaches the coherence length ($d \approx \xi$) demonstrates that the dimensional confinement of the superconducting channel gives rise to distinct manifestations of fluctuation phenomena. Remarkably, the coexistence of BKT and TAPS mechanisms, traditionally associated with 2D and quasi-1D systems respectively, indicates that these films occupy a unique position at the boundary of a previously unexplored dimensional crossover between 2D and 1D superconductivity. This novel experimental approach, characterized by the simultaneous observation of multiple fluctuation phenomena, illuminates the profound influence of dimensionality on the fundamental properties of ultra-thin superconducting films and establishes a new framework for understanding the quantum mechanics governing these systems.

Chapter 6

Conclusion and Future perspective

This final chapter serves as a comprehensive conclusion, summarizing the experimental findings and emphasizing the significant influence of systematic thickness reduction on the superconducting properties of NbN films. Throughout our investigation, we meticulously explored the interplay between film thickness, inherent disorder, and low dimensionality which are critical factors in generating phase fluctuation effects.

Our research journey began with an in-depth analysis of NbN films, starting with the thickest film of 100 nm, considered a bulk-like system. Initially, we focused on understanding the general characteristics of these films and evaluating the impact of different substrates on their superconducting properties. Through this methodical approach, we identified key trends and behaviors that emerged as the film thickness was systematically reduced.

In particular, NbN films deposited on MgO substrates stood out for their exceptional superconducting properties. These films displayed the highest critical temperature and critical current values, with sharp and well-defined transitions. The superior performance of these films can be attributed to the minimal lattice mismatch between the NbN film and the MgO substrate, which enhances film quality and supports robust superconductivity.

Conversely, the NbN films on silicon substrate performed poorly, with most of them lacking a distinct sharp transition. Our analysis revealed significant deviations and anomalies in the superconducting behavior reaching the film thickness of 25 nm. Reducing the thickness further to 15 nm, a complete alteration in the superconducting properties was observed, indicating a dimensional crossover.

The transition from a three-dimensional system to a 2D regime gave rise to a topological phase transition known as BKT transition, resulting from the breaking of vortex-antivortex pairs and representing a paradigm distinct from the BCS effect. In our analysis of this phenomenon, we employed the Cooper pair fluctuation model. Our investigation revealed that the resistivity above T_C exhibits a linear dependence on T that is consistent only with 2D fluctuation-conductivity behavior while being incompatible with predictions for 1D and 3D systems. This observation confirms the 2D nature of our NbN films. Furthermore, our findings regarding the polarizability values of vortex-antivortex pairs at the BKT transition align well with the universal relation proposed by Nelson and Kosterlitz carried out for different NbN films. In one case, the measured polarizability was approximately twice the expected value, providing further evidence for the dimensional crossover from 3D to 2D at a film thickness of 10 nm, as no BKT transition was detected at 15 nm. Additional support for this dimensional crossover is provided by the analysis of the α exponent extracted from the analysis of the I-V curves, which exhibits a sharp transition from 1 to 3 in proximity to T_{BKT}, in agreement with theoretical expectations. These findings not only provide insights into the BKT transition but also establish the effectiveness of our experimental approach, validating the dimensional crossover and the associated physical phenomena observed in our NbN films.

In pursuit of a comprehensive understanding of BKT physics, we conducted a novel investigation by introducing magnetic fields, a previously unexplored parameter in the BKT studies. we set out to explore the behavior of ultra-thin NbN films, with a thickness not exceeding 15 nm, under the influence of perpendicular field intensity. These fields ranged from 3600 G to 1300 G. Intriguingly, our investigation revealed a remarkable observation:

at these magnetic field intensities, the BKT effect vanished completely, without exhibiting any discernible trend. This discovery intrigued us and provided a unique opportunity to explore the behavior of thin NbN films under the low-field regime.

To comprehensively study this, we carefully measured the resistivity, $\rho(T)$, of these thin NbN films near T_C, while systematically varying the intensity of the perpendicular magnetic field, H, from 0 to 150 Gauss. In our analysis, we relied on two well-established theoretical models: the Aslamazov-Larkin (AL) Cooper pair fluctuation model and the Halperin-Nelson (HN) theory. These models have proven effective in describing the gradual reduction in $\rho(T)$ as T_C is approached from higher temperatures. Additionally, we focused on analyzing the transition from HN behavior to 2D AL conductivity. This analysis of NbN ultra-thin films has revealed intriguing characteristics of the BKT transition, particularly its sensitivity to weak perpendicular magnetic fields. Experimental findings demonstrate that the hints of the gradual smearing of this effect are evident from the breakdown of the Halperin-Nelson description of the fluctuation conductivity near the BKT transition at the magnetic field of 100 G, coupled with improved agreement between the Aslamazov-Larkin model and experimental data. Beyond $H = 100$ G, any indications of the BKT phenomenon become entirely obscured.

By carefully analyzing the I-V characteristics, we made a significant observation. At magnetic field intensities up to 5 G, we observed a distinct and well-defined jump in the superconducting phase stiffness precisely at the BKT temperature. However, as the field intensity increased beyond this threshold, we detected a gradual smearing of the BKT transition. This was evident from a crossover in the non-linear I-V characteristics, transitioning towards a more conventional-like behavior as the intensity increased. We have attributed this behavior to the influence of field-induced vortices, which screens and weakens the interaction between vortex-antivortex pairs. This mechanism promotes a tunable crossover from BKT to BCS superconductivity.

This study underscores the significant role played by weak magnetic fields in 2D superconducting systems, an aspect that is typically negligible in 3D systems. These findings have implications for the design of integrated superconducting circuits, emphasizing the need to consider the impact of weak magnetic fields. Furthermore, our results suggest the possibility of similar effects in analogous systems such as 2D rotating superfluids, realized with fermionic atoms confined in 2D pancakes. This emerging field of investigation may provide further insights into the BKT transition in 2D rotating superfluids. Overall, our study contributes to a deeper understanding of the interplay between weak magnetic fields and 2D superconducting and superfluid systems, paving the way for future advancements in these areas of research. This discovery of field-sensitive BKT physics has important implications for the development of superconducting devices operating in real-world environments, where even minimal stray magnetic fields could significantly impact their performance. The ability to precisely characterize and predict these effects provides crucial design considerations for future superconducting quantum devices.

In addition to our investigation of BKT physics, we detected and characterized the phase-slip events, both quantum and thermal, which are typically observed in quasi-1D superconductors. Achieving such findings required precise fine-tuning of our experimental setup and careful selection of the material system. Remarkably, we detected both quantum and thermal phase slips in our samples, each occurring in distinct temperature regimes. While traditional theoretical frameworks suggest these quantum effects should only manifest in structures with dimensions comparable to the coherence length, our observations reveal robust phase slip phenomena in significantly wider structures ($w/\xi \approx 1000$). This unexpected observation challenges our current understanding of dimensional constraints in superconducting systems and, while potentially attributable to self-organized nanoscale channels, suggests the need for a comprehensive reevaluation of size limitations in phase slip effects. The systematic nature of these observations across multiple samples points to an intrinsic mechanism that requires further theoretical and experimental investigation.

We further delved into the specific characteristics of these phase-slip events, particularly focusing on the number of phase slips occurring during both up-sweeps and down-sweeps of the sourced current. Our analysis revealed that the distribution of phase slips in the quantum regime was uneven, eventually converging to the same value in the temperature regime dominated by thermal fluctuations. Moreover, our experimental work uncovered the coexistence of BKT and phase-slip phenomena within the same NbN nanofilm—a previously unreported observation. This discovery is particularly significant as BKT and phase-slip events belong to systems of different dimensionality. Thus, we successfully demonstrated a dimensional crossover from 2D to quasi-1D within a single system.

These experimental findings serve as a catalyst for further exploration and in-depth studies of superconducting NbN nanofilms. The tunable nature of these films presents an exciting platform for generating and controlling novel quantum phenomena, which holds great potential for advancements in quantum technologies. Our work signifies a crucial step towards harnessing these quantum phenomena for practical applications.

Future perspective: Exploring NbN superconducting films in detail has provided a robust platform to leverage their superior characteristics among other Nb-based superconductors and to optimize their properties for various applications. My future research will focus on utilizing NbN films to develop high-impedance resonators, which are essential components in quantum circuits [86].

Recent studies have demonstrated that NbN films exhibit exceptionally high kinetic inductance, approaching the value of quantum resistance (R_Q) [79, 80]. This characteristic presents the advantage of compact high-L_K film resonators, enabling a decrease in the dimensions of both the readout and control systems. A key aspect of utilizing these materials within quantum frameworks is achieving conditions of low internal losses to maintain extended coherence times, which are essential for effective quantum computing.

To fully understand and harness these capabilities of NbN superconductors, the use of microwave resonators is indispensable. These microwave probing techniques not only aid in characterizing materials for quantum technologies but also offer a powerful tool for investigating fundamental physical phenomena in disordered superconductors, such as vortex dynamics and quantum phase transitions.

Through this approach, we aim to bridge the gap between fundamental understanding and practical applications, paving the way for the integration of these materials into next-generation quantum devices. The demonstrated ability to manipulate and control quantum effects through multiple parameters—thickness, magnetic field, and geometry—offers exciting possibilities for future device engineering, while our insights into the rich physics of low-dimensional superconductivity provide a robust foundation for advancing quantum technologies.

Bibliography

[1] M. Tinkham, *Introduction to superconductivity* (Courier Corporation, 2004).

[2] V. L. Ginzburg, V. L. Ginzburg, and L. Landau, *On the theory of superconductivity* (Springer, 2009).

[3] J. Bardeen, L. N. Cooper, and J. R. Schrieffer, Theory of superconductivity, Physical Review **108**, 1175 (1957).

[4] P. A. Lee, N. Nagaosa, and X.-G. Wen, Doping a Mott insulator: Physics of high-temperature superconductivity, Reviews of Modern Physics **78**, 17 (2006).

[5] R. F. Frindt, Superconductivity in Ultrathin NbSe2 Layers, Physical Review Letters **28**, 299 (1972).

[6] B. Orr, H. Jaeger, and A. Goldman, Local superconductivity in ultrathin Sn films, Phys. Rev. B **32**, 7586 (1985).

[7] H. Jaeger, D. Haviland, A. Goldman, and B. Orr, Threshold for superconductivity in ultrathin amorphous gallium films, Phys. Rev. B **34**, 4920 (1986).

[8] J. Lee, F. Schmitt, R. Moore, S. Johnston, Y.-T. Cui, W. Li, M. Yi, Z. Liu, M. Hashimoto, Y. Zhang, *et al.*, Interfacial mode coupling as the origin of the enhancement of Tc in FeSe films on SrTiO3, Nature **515**, 245 (2014).

[9] H. Ding, Y.-F. Lv, K. Zhao, W.-L. Wang, L. Wang, C.-L. Song, X. Chen, X.-C. Ma, and Q.-K. Xue, High-temperature superconductivity in single unit cell FeSe films on anatase TiO2 (001), Phys. Rev. Lett. **117**, 067001 (2016).

[10] Y. Yu, L. Ma, P. Cai, R. Zhong, C. Ye, J. Shen, G. D. Gu, X. H. Chen, and Y. Zhang, High-temperature superconductivity in monolayer BSCCO, Nature **575**, 156 (2019).

[11] J.-P. Xu, M.-X. Wang, Z. L. Liu, J.-F. Ge, X. Yang, C. Liu, Z. A. Xu, D. Guan, C. L. Gao, D. Qian, *et al.*, Experimental detection of a Majorana mode in the core of a magnetic vortex inside a topological insulator-superconductor Bi2Te3/NbSe2 heterostructure, Phys. Rev. Lett. **114**, 017001 (2015).

[12] H.-H. Sun, K.-W. Zhang, L.-H. Hu, C. Li, G.-Y. Wang, H.-Y. Ma, Z.-A. Xu, C.-L. Gao, D.-D. Guan, Y.-Y. Li, *et al.*, Majorana zero mode detected with spin selective Andreev reflection in the vortex of a topological superconductor, Phys. Rev. Lett. **116**, 257003 (2016).

[13] Z. Ge, C. Yan, H. Zhang, D. Agterberg, M. Weinert, and L. Li, Evidence for d-wave superconductivity in single layer FeSe/SrTiO3 probed by quasiparticle scattering off step edges, Nano Letters **19**, 2497 (2019).

[14] H. Wang, X. Huang, J. Lin, J. Cui, Y. Chen, C. Zhu, F. Liu, Q. Zeng, J. Zhou, P. Yu, *et al.*, High-quality monolayer superconductor NbSe2 grown by chemical vapour deposition, Nature Communications **8**, 394 (2017).

[15] Y. Cao, A. Mishchenko, G. Yu, E. Khestanova, A. Rooney, E. Prestat, A. Kretinin, P. Blake, M. B. Shalom, C. Woods, *et al.*, Quality heterostructures from two-dimensional crystals unstable in air by their assembly in inert atmosphere, Nano Letters **15**, 4914 (2015).

[16] M. X. Wang, C. Liu, J. P. Xu, F. Yang, L. Miao, M. Y. Yao, C. L. Gao, C. Shen, X. Ma, X. Chen, Z. A. Xu, Y. Liu, S. C. Zhang, D. Qian, J. F. Jia, and Q. K. Xue, The Coexistence of Superconductivity and Topological Order in the Bi2Se3 Thin Films, Science **336**, 52 (2012).

[17] X. Xi, Z. Wang, W. Zhao, J.-H. Park, K. T. Law, H. Berger, L. Forró, J. Shan, and K. F. Mak, Ising pairing in superconducting NbSe2 atomic layers, Nature Physics **12**, 139 (2016).

[18] S. C. De la Barrera, M. R. Sinko, D. P. Gopalan, N. Sivadas, K. L. Seyler, K. Watanabe, T. Taniguchi, A. W. Tsen, X. Xu, D. Xiao, *et al.*, Tuning Ising superconductivity with layer and spin-orbit coupling in two-dimensional transition-metal dichalcogenides, Nature Communications **9**, 1427 (2018).

[19] D. Costanzo, S. Jo, H. Berger, and A. F. Morpurgo, Gate-induced superconductivity in atomically thin MoS2 crystals, Nature Nanotechnology **11**, 339 (2016).

[20] E. Khestanova, J. Birkbeck, M. Zhu, Y. Cao, G. Yu, D. Ghazaryan, J. Yin, H. Berger, L. Forro, T. Taniguchi, *et al.*, Unusual suppression of the superconducting energy gap and critical temperature in atomically thin NbSe2, Nano Letters **18**, 2623 (2018).

[21] V. Fatemi, S. Wu, Y. Cao, L. Bretheau, Q. D. Gibson, K. Watanabe, T. Taniguchi, R. J. Cava, and P. Jarillo-Herrero, Electrically tunable low-density superconductivity in a monolayer topological insulator, Science **362**, 926 (2018).

[22] E. Sajadi, T. Palomaki, Z. Fei, W. Zhao, P. Bement, C. Olsen, S. Luescher, X. Xu, J. A. Folk, and D. H. Cobden, Gate-induced superconductivity in a monolayer topological insulator, Science **362**, 922 (2018).

[23] J. T. Ye, Y. J. Zhang, R. Akashi, M. S. Bahramy, R. Arita, and Y. Iwasa, Superconducting Dome in a Gate-Tuned Band Insulator, Science **338**, 1193 (2012).

[24] J. M. Lu, O. Zheliuk, I. Leermakers, N. F. Q. Yuan, U. Zeitler, K. T. Law, and J. T. Ye, Evidence for two-dimensional Ising superconductivity in gated MoS2, Science **350**, 1353 (2015).

[25] Y. Saito, Y. Nakamura, M. S. Bahramy, Y. Kohama, J. Ye, Y. Kasahara, Y. Nakagawa, M. Onga, M. Tokunaga, T. Nojima, Y. Yanase, and Y. Iwasa, Superconductivity protected by spin2̆013valley locking in ion-gated MoS2, Nature Physics **12**, 144 (2016).

[26] D. Jiang, T. Hu, L. You, Q. Li, A. Li, H. Wang, G. Mu, Z. Chen, H. Zhang, G. Yu, J. Zhu, Q. Sun, C. Lin, H. Xiao, X. Xie, and M. Jiang, High-Tc superconductivity in ultrathin Bi2Sr2CaCu2O8+x down to half-unit-cell thickness by protection with graphene, Nature Communications **5**, 5708 (2014).

[27] K. S. Novoselov, D. Jiang, F. Schedin, T. J. Booth, V. V. Khotkevich, S. V. Morozov, and A. K. Geim, Two-dimensional atomic crystals, Proceedings of the National Academy of Sciences **102**, 10451 (2005).

[28] L. J. Sandilands, A. A. Reijnders, A. H. Su, V. Baydina, Z. Xu, A. Yang, G. Gu, T. Pedersen, F. Borondics, and K. S. Burch, Optical probing of the properties of exfoliated MoS2, Physical Review B **90**, 081402 (2014).

[29] Y. Yu, L. Ma, P. Cai, R. Zhong, C. Ye, J. Shen, G. D. Gu, X. H. Chen, and Y. Zhang, High-temperature superconductivity in monolayer Bi2Sr2CaCu2O8+x, Nature **575**, 156 (2019).

[30] V. Brosco, G. Serpico, V. Vinokur, N. Poccia, and U. Vool, Superconducting qubit

based on twisted cuprate van der Waals heterostructures, Phys. Rev. Lett. **132**, 017003 (2024).

[31] J.-F. Ge, Z.-L. Liu, C. Liu, C.-L. Gao, D. Qian, Q.-K. Xue, Y. Liu, and J.-F. Jia, Superconductivity above 100 K in single-layer FeSe films on doped SrTiO3, Nature Materials **14**, 285 (2015).

[32] X. Shi, Z. Q. Han, X. L. Peng, P. Richard, T. Qian, X. X. Wu, M. W. Qiu, S. C. Wang, J. P. Hu, Y. J. Sun, and H. Ding, Enhanced superconductivity in FeSe films on SrTiO3 coated with a thin layer of TiO2, Nature Communications **8**, 14988 (2017).

[33] W. H. Zhang, X. Liu, C. H. Wen, R. Peng, S. Y. Tan, B. P. Xie, T. Zhang, and D. L. Feng, Thickness Dependence of the Superconducting Gap in ultrathin FeSe Films, Nano Letters **16**, 1969 (2016).

[34] S. Tan, Y. Zhang, M. Xia, Z. Ye, F. Chen, X. Xie, R. Peng, D. Xu, Q. Fan, H. Xu, J. Jiang, T. Zhang, X. Lai, T. Xiang, J. Hu, B. Xie, and D. Feng, Interface-induced superconductivity and strain-dependent spin density waves in FeSe/SrTiO3 thin films, Nature Materials **12**, 634 (2013).

[35] Y. Cao, V. Fatemi, S. Fang, K. Watanabe, T. Taniguchi, E. Kaxiras, and P. Jarillo-Herrero, Unconventional superconductivity in magic-angle graphene superlattices, Nature **556**, 43 (2018).

[36] G. Chen, A. L. Sharpe, P. Gallagher, I. T. Rosen, E. J. Fox, L. Jiang, B. Lyu, H. Li, K. Watanabe, T. Taniguchi, J. Jung, Z. Shi, D. Goldhaber-Gordon, Y. Zhang, and F. Wang, Signatures of tunable superconductivity in a trilayer graphene moire superlattice, Nature **572**, 215 (2019).

[37] Y. Cao, D. Rodan-Legrain, O. Rubies-Bigorda, J. M. Park, K. Watanabe, T. Taniguchi, and P. Jarillo-Herrero, Tunable correlated states and spin-polarized phases in twisted bilayer graphene, Nature **583**, 215 (2020).

[38] X. Liu, Z. Hao, E. Khalaf, J. Y. Lee, Y. Ronen, H. Yoo, D. H. Najafabadi, K. Watanabe, T. Taniguchi, A. Vishwanath, and P. Kim, Tunable spin-polarized correlated states in twisted double bilayer graphene, Nature **583**, 221 (2020).

[39] C. Shen, Y. Chu, Q. Wu, N. Li, S. Wang, Y. Zhao, J. Tang, J. Liu, J. Tian, K. Watanabe, T. Taniguchi, R. Yang, Z. Y. Meng, D. Shi, O. V. Yazyev, and G. Zhang, Correlated states in twisted double bilayer graphene, Nature Physics **16**, 520 (2020).

[40] Y. Cao, V. Fatemi, A. Demir, S. Fang, S. L. Tomarken, J. Y. Luo, J. D. Sanchez-Yamagishi, K. Watanabe, T. Taniguchi, E. Kaxiras, R. C. Ashoori, and P. Jarillo-Herrero, Correlated insulator behaviour at half-filling in magic-angle graphene superlattices, Nature **556**, 80 (2018).

[41] A. R. Urade, I. Lahiri, and K. Suresh, Graphene properties, synthesis and applications: a review, Jom **75**, 614 (2023).

[42] M. M. Ugeda, A. J. Bradley, Y. Zhang, S. Onishi, Y. Chen, W. Ruan, C. Ojeda-Aristizabal, H. Ryu, M. T. Edmonds, H.-Z. Tsai, A. Riss, S.-K. Mo, D. Lee, A. Zettl, Z. Hussain, Z.-X. Shen, and M. F. Crommie, Characterization of collective ground states in single-layer NbSe2, Nature Physics **12**, 92 (2016).

[43] L. Li, W. Han, L. Pi, P. Niu, J. Han, C. Wang, B. Su, H. Li, J. Xiong, Y. Bando, and T. Zhai, 2D Superconductivity: Recent Progress and Future Perspectives, InfoMat **1**, 54 (2019).

[44] H. Jiang, L. Zheng, Z. Liu, and X. Wang, Recent Progress on Synthesis and Ap-

plications of MXenes: A Family of Two-Dimensional Transition Metal Carbides and/or Nitrides, InfoMat **2**, 1077 (2020).

[45] M. Napari, T. N. Huq, R. L. Z. Hoye, and J. L. MacManus-Driscoll, A Perspective on the Formation of Functional Oxide Thin Films: Epitaxy, Defects, and Properties, InfoMat **2**, 769 (2020).

[46] W. Skocpol and M. Tinkham, Fluctuations near superconducting phase transitions, Reports on Progress in Physics **38**, 1049 (1975).

[47] A. Larkin and A. Varlamov, *Theory of fluctuations in superconductors*, Vol. 127 (OUP Oxford, 2005).

[48] A. Bezryadin, C. N. Lau, and M. Tinkham, Quantum suppression of superconductivity in ultrathin nanowires, Nature **404**, 971 (2000).

[49] A. Bezryadin, Quantum suppression of superconductivity in nanowires, J. Phys.: Cond. Mat. **20**, 043202 (2008).

[50] W. Zhao, X. Liu, and M. Chan, Quantum Phase Slips in 6 mm Long Niobium Nanowire, Nano Lett. **16**, 1173 (2016).

[51] J. S. Lehtinen, T. Sajavaara, K. Y. Arutyunov, M. Y. Presnjakov, and A. L. Vasiliev, Evidence of quantum phase slip effect in titanium nanowires, Phys. Rev. B **85**, 094508 (2012).

[52] X. Baumans, D. C. O. Adami, V. S. Zharinov, N. Verellen, G. Papari, J. E. Scheerder, G. Zhang, V. V. Moshchalkov, A. V. Silhanek, and J. V. de Vondel, Thermal and quantum depletion of superconductivity in narrow junctions created by controlled electromigration, Nat. Commun. **7**, 10560 (2016).

[53] H. Kim, F. Gay, A. D. Maestro, B. Sacépé, and A. Rogachev, Pair-breaking quantum phase transition in superconducting nanowires, Nat. Phys. **14**, 912 (2018).

[54] C. Carbillet, S. Caprara, M. Grilli, C. Brun, T. Cren, F. Debontridder, B. Vignolle, W. Tabis, D. Demaille, L. Largeau, *et al.*, Confinement of superconducting fluctuations due to emergent electronic inhomogeneities, Phys. Rev. B **93**, 144509 (2016).

[55] N. Mason and A. Kapitulnik, Dissipation Effects on the Superconductor-Insulator Transition in 2D Superconductors, Phys. Rev. Lett. **82**, 5341 (1999).

[56] N. Breznay, M. Tendulkar, L. Zhang, S.-C. Lee, and A. Kapitulnik, Superconductor to weak-insulator transitions in disordered tantalum nitride films, Phys. Rev. B **96**, 134522 (2017).

[57] V. N. Ryzhov, E. Tareyeva, Y. D. Fomin, and E. N. Tsiok, Berezinskii-Kosterlitz-Thouless transition and two-dimensional melting, Physics-Uspekhi **60**, 857 (2017).

[58] J. M. Kosterlitz and D. J. Thouless, Ordering, metastability and phase transitions in two-dimensional systems, J. Phys. C: Sol. State Phys. **6**, 1181 (1973).

[59] J. Hsu and A. Kapitulnik, Superconducting transition, fluctuation, and vortex motion in a two-dimensional single-crystal Nb film, Phys. Rev. B **45**, 4819 (1992).

[60] S. Caprara, M. Grilli, B. Leridon, and J. Vanacken, Paraconductivity in layered cuprates, Phys. Rev. B **79**, 024506 (2009).

[61] R. Bombín, F. Mazzanti, and J. Boronat, Berezinskii-Kosterlitz-Thouless transition in two-dimensional dipolar stripes, Phys. Rev. A **100**, 063614 (2019).

[62] W. Zhang, G.-D. Lin, and L.-M. Duan, Berezinskii-Kosterlitz-Thouless transition in a trapped quasi-two-dimensional Fermi gas near a Feshbach resonance, Phys. Rev. A **78**, 043617 (2008).

[63] M. Sharma, M. Singh, R. K. Rakshit, S. P. Singh, M. Fretto, N. De Leo, A. Perali, and N. Pinto, Complex phase-fluctuation effects correlated with granularity in superconducting NbN nanofilms, Nanomaterials **12**, 4109 (2022).

[64] L. Benfatto, C. Castellani, and T. Giamarchi, Broadening of the Berezinskii-Kosterlitz-Thouless superconducting transition by inhomogeneity and finite-size effects, Phys. Rev. B **80**, 214506 (2009).

[65] G. Venditti, J. Biscaras, S. Hurand, N. Bergeal, J. Lesueur, A. Dogra, R. Budhani, M. Mondal, J. Jesudasan, P. Raychaudhuri, *et al.*, Nonlinear I- V characteristics of two-dimensional superconductors: Berezinskii-Kosterlitz-Thouless physics versus inhomogeneity, Phys. Rev. B **100**, 064506 (2019).

[66] M. Mondal, S. Kumar, M. Chand, A. Kamlapure, G. Saraswat, G. Seibold, L. Benfatto, and P. Raychaudhuri, Role of the vortex-core energy on the Berezinskii-Kosterlitz-Thouless transition in thin films of NbN, Phys. Rev. Lett. **107**, 217003 (2011).

[67] A. Weitzel, L. Pfaffinger, I. Maccari, K. Kronfeldner, T. Huber, L. Fuchs, J. Mallord, S. Linzen, E. Il'ichev, N. Paradiso, and C. Strunk, Sharpness of the Berezinskii-Kosterlitz-Thouless Transition in Disordered NbN Films, Phys. Rev. Lett. **131**, 186002 (2023).

[68] J. Yong, T. Lemberger, L. Benfatto, K. Ilin, and M. Siegel, Robustness of the Berezinskii-Kosterlitz-Thouless transition in ultrathin NbN films near the superconductor-insulator transition, Phys. Rev. B **87**, 184505 (2013).

[69] H. Bartolf, A. Engel, A. Schilling, K. Il'in, M. Siegel, H.-W. Hübers, and A. Semenov, Current-assisted thermally activated flux liberation in ultrathin nanopatterned NbN superconducting meander structures, Phys. Rev. B **81**, 024502 (2010).

[70] V. Giglia, V. Gauthier, T. Hemakumara, R. Sundaram, D. Drouin, M. Pioro-Ladriere, and S. Nicolay, Superconducting NbN for strong magnetic field applications: Impact of the thin films intrinsic disorder, IEEE Transactions on Applied Superconductivity **33**, 1 (2022).

[71] A. Kamlapure, , M. Mondal, M. Chand, A. Mishra, J. Jesudasan, V. Bagwe, L. Benfatto, V. Tripathi, and P. Raychaudhuri, Measurement of magnetic penetration depth and superconducting energy gap in very thin epitaxial NbN films, App. Phys. Lett. **96**, 072509 (2010).

[72] K. Gray, J. Brorson, and P. A. Bancel, Resistance measurements and vortex fluctuations in two-dimensional superconducting films, J. of Low Temp. Phys. **59**, 529 (1985).

[73] J. Garland and H. J. Lee, Influence of a magnetic field on the two-dimensional phase transition in thin-film superconductors, Phys. Rev. B **36**, 3638 (1987).

[74] M. Soldatenkova, A. Triznova, E. Baeva, P. Zolotov, A. Lomakin, A. Kardakova, and G. Goltsman, Normal-state transport in superconducting NbN films on r-cut sapphire, in *J. Phys.: Confer. Series*, Vol. 2086 (IOP Publishing, 2021) p. 012212.

[75] S. Chockalingam, M. Chand, J. Jesudasan, V. Tripathi, and P. Raychaudhuri, Superconducting properties and Hall effect of epitaxial NbN thin films, Phys. Rev. B **77**, 214503 (2008).

[76] H. Bartolf, A. Engel, A. Schilling, K. Il'in, M. Siegel, H.-W. Hübers, and A. Semenov, Current-assisted thermally activated flux liberation in ultrathin nanopatterned NbN superconducting meander structures, Phys. Rev. B **81**, 024502 (2010).

[77] G. Venditti, J. Biscaras, S. Hurand, N. Bergeal, J. Lesueur, A. Dogra, R. C. Budhani, M. Mondal, J. Jesudasan, P. Raychaudhuri, S. Caprara, and L. Benfatto,

Nonlinear I-V characteristics of two-dimensional superconductors: Berezinskii-Kosterlitz-Thouless physics versus inhomogeneity, Phys. Rev. B **100**, 064506 (2019).

[78] M. Sharma, S. Caprara, A. Perali, S. P. Singh, S. Singh, and N. Pinto, Berezinskii-Kosterlitz-Thouless to BCS-like superconducting transition crossover driven by weak magnetic fields in ultra-thin NbN films, arXiv:2403.11685 (2024).

[79] S. Frasca, I. N. Arabadzhiev, S. B. de Puechredon, F. Oppliger, V. Jouanny, R. Musio, M. Scigliuzzo, F. Minganti, P. Scarlino, and E. Charbon, NbN films with high kinetic inductance for high-quality compact superconducting resonators, Phys. Rev. A **20**, 044021 (2023).

[80] D. Niepce, J. Burnett, and J. Bylander, High kinetic inductance NbN nanowire superinductors, Phys. Rev. A **11**, 044014 (2019).

[81] J. S. Langer and V. Ambegaokar, Intrinsic resistive transition in narrow superconducting channels, Physical Review **164**, 498 (1967).

[82] N. Giordano, Superconductivity and dissipation in small-diameter Pb-In wires, Phys. Rev. B **43**, 160 (1991).

[83] K. I. INC, Achieving Accurate and Reliable Resistance Measurements in Low Power and Low Voltage Applications (2004).

[84] N. Pinto, S. J. Rezvani, A. Perali, L. Flammia, M. V. Milošević, M. Fretto, C. Cassiago, and N. De Leo, Dimensional crossover and incipient quantum size effects in superconducting niobium nanofilms, Sci. Rep. **8**, 4710 (2018).

[85] M. Tinkham and V. Emery, Books-Introduction to Superconductivity, Physics Today **49**, 65 (1996).

[86] B. Sacepe, M. Feigel'man, and T. M. Klapwijk, Quantum breakdown of superconductivity in low-dimensional materials, Nature Physics **16**, 734 (2020).

[87] J. V. Jos, *40 years of Berezinskii-Kosterlitz-Thouless theory* (World Scientific, 2013).

[88] V. L. Berezinskii, Destruction of Long-range Order in One-dimensional and Two-dimensional Systems having a Continuous Symmetry Group I. Classical Systems, Sov. Phys. JETP **32** (1971).

[89] E. Jacob, Topological phase transitions (BKT).

[90] M. Cyrot, Ginzburg-Landau theory for superconductors, Reports on Progress in Physics **36**, 103 (1973).

[91] P. Raychaudhuri and S. Dutta, Phase fluctuations in conventional superconductors, Journal of Physics: Condensed Matter **34**, 083001 (2021).

[92] L. Benfatto, The Berezinskii-Kosterlitz-Thouless Transition and its Application to Superconducting Systems, in *Correlations and Phase Transitions*, Modeling and Simulation, Vol. 14, edited by E. Pavarini and E. Koch (Forschungszentrum Julich, 2024).

[93] L. M. Joshi, A. Verma, A. Gupta, P. Rout, S. Husale, and R. Budhani, Superconducting properties of NbN film, bridge and meanders, AIP Adv. **8**, 055305 (2018).

[94] D. Hazra, N. Tsavdaris, S. Jebari, A. Grimm, F. Blanchet, F. Mercier, E. Blanquet, C. Chapelier, and M. Hofheinz, Superconducting properties of very high quality NbN thin films grown by high temperature chemical vapor deposition, Supercond. Sci. Technol. **29**, 105011 (2016).

[95] L. Kang, B. B. Jin, X. Y. Liu, X. Q. Jia, J. Chen, Z. M. Ji, W. W. Xu, P. H. Wu, S. B. Mi, A. Pimenov, Y. J. Wu, and B. G. Wang, Suppression of superconductivity in epitaxial NbN ultrathin films, J. Appl. Phys. **109**, 033908 (2011).

[96] K. Smirnov, A. Divochiy, Y. Vakhtomin, P. Morozov, P. Zolotov, A. Antipov, and V. Seleznev, NbN single-photon detectors with saturated dependence of quantum efficiency, Supercond. Sci. Technol. **31**, 035011 (2018).

[97] K. Senapati, N. K. Pandey, R. Nagar, and R. C. Budhani, Normal-state transport and vortex dynamics in thin films of two structural polymorphs of superconducting NbN, Phys. Rev. B **74**, 104514 (2006).

[98] M. Sidorova, A. Semenov, H.-W. Hubers, K. Ilin, M. Siegel, I. Charaev, M. Moshkova, N. Kaurova, G. N. Goltsman, X. Zhang, and A. Schilling, Electron energy relaxation in disordered superconducting NbN films, Phys. Rev. B **102**, 054501 (2020).

[99] S. P. Chockalingam, M. Chand, J. Jesudasan, V. Tripathi, and P. Raychaudhuri, Superconducting properties and Hall effect of epitaxial NbN thin films, Phys. Rev. B **77**, 214503 (2008).

[100] K. Il'in, M. Siegel, A. Semenov, A. Engel, and H.-W. Hübers, Critical current of Nb and NbN thin-film structures: The cross-section dependence, Phys. Stat. Sol. (c) **2**, 1680 (2005).

[101] L. Aslamasov and A. Larkin, The influence of fluctuation pairing of electrons on the conductivity of normal metal, Phys. Lett. A **26**, 238 (1968).

[102] K. Maki, Critical Fluctuation of the Order Parameter in a Superconductor. I, Prog. Theor. Phys. **40**, 193 (1968).

[103] R. Thompson, Microwave, Flux Flow, and Fluctuation Resistance of Dirty Type-II Superconductors, Phys. Rev. B **1**, 327 (1970).

[104] M. Bell, A. Sergeev, V. Mitin, J. Bird, A. Verevkin, and G. Gol'tsman, One-dimensional resistive states in quasi-two-dimensional superconductors: Experiment and theory, Phys. Rev. B **76**, 094521 (2007).

[105] T. Yamashita, S. Miki, K. Makise, W. Qiu, H. Terai, M. Fujiwara, M. Sasaki, and Z. Wang, Origin of intrinsic dark count in superconducting nanowire single-photon detectors, Appl. Phys. Lett. **99**, 161105 (2011).

[106] D. R. Nelson and J. Kosterlitz, Universal jump in the superfluid density of two-dimensional superfluids, Phys. Rev. Lett. **39**, 1201 (1977).

[107] Y. Saito, Y. M. Itahashi, T. Nojima, and Y. Iwasa, Dynamical vortex phase diagram of two-dimensional superconductivity in gated MoS2, Phys. Rev. Mat. **4**, 074003 (2020).

[108] Z. Hu, Z. Ma, Y.-D. Liao, H. Li, C. Ma, Y. Cui, Y. Shangguan, Z. Huang, Y. Qi, and W. Li, Evidence of the Berezinskii-Kosterlitz-Thouless phase in a frustrated magnet, Nat. Comm. **11**, 5631 (2020).

[109] H. Van der Zant, H. Rijken, and J. Mooij, The superconducting transition of 2-D Josephson-junction arrays in a small perpendicular magnetic field, Journal of low temperature physics **79**, 289 (1990).

[110] A. Y. Mironov, D. M. Silevitch, T. Proslier, S. V. Postolova, M. V. Burdastyh, A. K. Gutakovskii, T. F. Rosenbaum, V. V. Vinokur, and T. I. Baturina, Charge Berezinskii-Kosterlitz-Thouless transition in superconducting NbTiN films, Sci. Rep. **8**, 4082 (2018).

[111] X. Wei, P. Roy, Z. Yang, D. Zhang, Z. He, P. Lu, O. Licata, H. Wang, B. Mazumder, N. Patibandla, *et al.*, Ultrathin epitaxial Niobium nitride superconducting films with high upper critical field grown at low temperature, Materials Research Letters **9**, 336 (2021).

[112] R. Baskaran, A. Thanikai Arasu, E. Amaladass, and M. Janawadkar, High upper critical field in disordered niobium nitride superconductor, Journal of Applied Physics **116**, 163908 (2014).

[113] B. McNaughton, N. Pinto, A. Perali, and M. V. Milošević, Causes and consequences of ordering and dynamic phases of confined vortex rows in superconducting nanostripes, Nanomaterials **12**, 4043 (2022).

[114] E. Silva, Frequency-dependent fluctuational conductivity above in anisotropic superconductors: effects of a short wavelength cutoff, The European Physical Journal B-Condensed Matter and Complex Systems **27**, 497 (2002).

[115] L. Aslamasov and A. Larkin, The influence of fluctuation pairing of electrons on the conductivity of normal metal, Phys. Lett. A **26**, 238 (1968).

[116] E. Silva, R. Marcon, S. Sarti, R. Fastampa, M. Giura, M. Boffa, and A. Cucolo, Microwave fluctuational conductivity in YBaCuO, The European Physical Journal B-Condensed Matter and Complex Systems **37**, 277 (2004).

[117] E. Silva, S. Sarti, R. Fastampa, and M. Giura, Excess conductivity of overdoped Bi2Sr2CaCu2O8+x crystals well above Tc, Physical Review B **64**, 144508 (2001).

[118] K. Maki, The critical fluctuation of the order parameter in type-II superconductors, Progress of Theoretical Physics **39**, 897 (1968).

[119] R. S. Thompson, Microwave, flux flow, and fluctuation resistance of dirty type-II superconductors, Phys. Rev. B **1**, 327 (1970).

[120] S. Caprara, M. Grilli, B. Leridon, and J. Lesueur, Extended paraconductivity regime in underdoped cuprates, Phys. Rev. B **72**, 104509 (2005).

[121] C. D'Errico, S. S. Abbate, and G. Modugno, Quantum phase slips: from condensed matter to ultracold quantum gases, Philosophical Transactions of the Royal Society A: Mathematical, Physical and Engineering Sciences **375**, 20160425 (2017).

[122] W. A. Little, Decay of persistent currents in small superconductors, Physical Review **156**, 396 (1967).

[123] J. Mooij and Y. V. Nazarov, Superconducting nanowires as quantum phase-slip junctions, Nature Physics **2**, 169 (2006).

[124] B. Gajar, S. Yadav, D. Sawle, K. K. Maurya, A. Gupta, R. Aloysius, and S. Sahoo, Substrate mediated nitridation of niobium into superconducting Nb2N thin films for phase slip study, Sci. Rep. **9**, 1 (2019).

[125] S. L. Chu, A. T. Bollinger, and A. Bezryadin, Phase slips in superconducting films with constrictions, Phys. Rev. B **70**, 214506 (2004).

[126] D. McCumber and B. Halperin, Time scale of intrinsic resistive fluctuations in thin superconducting wires, Phys. Rev. B **1**, 1054 (1970).

[127] D. G. Joshi and A. Bhattacharya, Revisiting the Langer–Ambegaokar–McCumber–Halperin theory of resistive transitions in one-dimensional superconductors with exact solutions, Journal of Physics: Condensed Matter **23**, 342203 (2011).

[128] J. Lukens, R. Warburton, and W. Webb, Onset of quantized thermal fluctuations in one-dimensional superconductors, Phys. Rev. Lett. **25**, 1180 (1970).

[129] R. Newbower, M. Beasley, and M. Tinkham, Fluctuation effects on the superconducting transition of tin whisker crystals, Phys. Rev. B **5**, 864 (1972).

[130] A. Van Run, J. Romijn, and J. Mooij, Superconduction phase coherence in weak aluminium strips, Japanese Journal of Applied Physics **26**, 1765 (1987).

[131] A. Rogachev, T.-C. Wei, D. Pekker, A. Bollinger, P. M. Goldbart, and A. Bezryadin, Magnetic-field enhancement of superconductivity in ultranarrow wires, Phys. Rev. Lett. **97**, 137001 (2006).

[132] J. Graybeal, P. Mankiewich, R. Dynes, and M. Beasley, Apparent destruction of superconductivity in the disordered one-dimensional limit, Phys. Rev. Lett. **59**, 2697 (1987).

[133] L. M. Joshi, P. Rout, S. Husale, and A. Gupta, Dissipation processes in superconducting NbN nanostructures, AIP Adv. **10**, 115116 (2020).

[134] A. Klimov, W. Słysz, M. Guziewicz, V. Kolkovsky, A. Malinowski, I. Zaytseva, and A. Abaloszew, Electric transport in the phase-slip-free superconducting epitaxial NbTiN sub-micron structures, Physica C: Superconductivity and its Applications **560**, 7 (2019).

[135] A. Sivakov, A. Glukhov, A. Omelyanchouk, Y. Koval, P. Müller, and A. Ustinov, Josephson behavior of phase-slip lines in wide superconducting strips, Phys. Rev. Lett. **91**, 267001 (2003).

[136] A. Kumar, S. Husale, H. Pandey, M. G. Yadav, M. Yousuf, G. S. Papanai, A. Gupta, and R. Aloysius, On the switching current and the re-trapping current of tungsten nanowires fabricated by Focussed Ion Beam (FIB) technique, Eng. Res. Express **3**, 025017 (2021).